MODELLING OF FLAMES SUBJECTED TO STRONG ELECTRIC FIELDS AND PULSED PLASMAS

by

BangShiuh Chen

A Dissertation

Submitted to the Faculty of Purdue University

In Partial Fulfillment of the Requirements for the degree of

Doctor of Philosophy

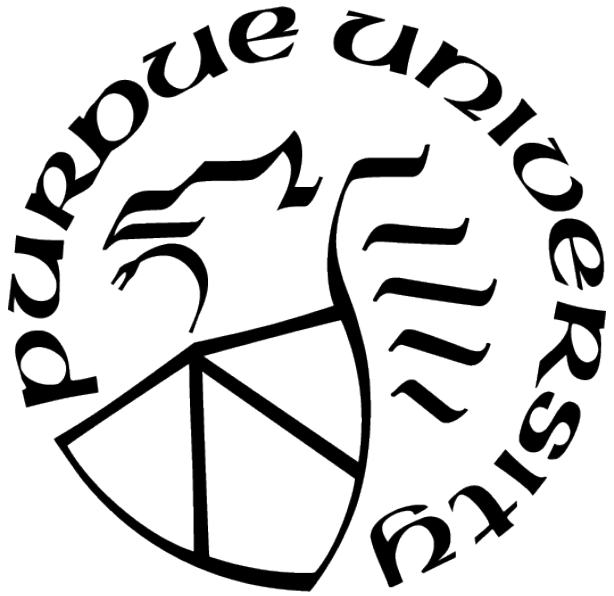

School of Aeronautics and Astronautics

West Lafayette, Indiana

August 2021

THE PURDUE UNIVERSITY GRADUATE SCHOOL
STATEMENT OF COMMITTEE APPROVAL

Dr. Sally Bane, Chair

School of Aeronautics and Astronautics

Dr. Allen Garner, Co-chair

School of Nuclear Engineering

Dr. Alina Alexeenko

School of Aeronautics and Astronautics

Dr. Sergey Macheret

School of Aeronautics and Astronautics

Approved by:

Dr. Gregory Blaisdell

To the spirit of open-source, because collaboration makes the world a better place.

ACKNOWLEDGMENTS

I want to thank all my friends, colleagues, family, and my church for supporting, encouraging, and praying for me on this journey to get my PhD. I cannot list all the helps I got, and I would not have been able to complete my study without any of you. My dad encouraged me to not give up in the early time of my PhD program, and helped me to find the research direction. My advisor Dr. Bane and Dr. Garner spent a lot of time and effort on editing my writing and communicating on the research ideas. My department head Dr. Shih helped me on the funding and is always very positive and encouraging to me. Dr. Speth, the author of the open-source code, Cantera, answered my programming questions, and helped me implementing my code. Dr. Macheret taught me plasma physics, and provided valuable suggestions on my research. My roommate, Tim, studied and exercised with me diligently. My landlord, Steve, cooked dinner for me every Tuesday. My friend, Mark, invited me to explore interesting places and events. Thank you all again!

TABLE OF CONTENTS

LIST OF TABLES

LIST OF FIGURES

LIST OF SYMBOLS

Y	mass fraction
u	flow velocity [$\mathrm{m\,s^{-1}}$]
j	diffusion flux [$\mathrm{kg\,m^{-2}\,s^{-1}}$]
W	molar mass [$\mathrm{g\,mol^{-1}}$]
X	mole fraction
z	location [m]
E	electric field [$\mathrm{V\,m^{-1}}$]
ρ	density [$\mathrm{kg\,m^{-3}}$]
$\dot{\omega}$	net production rate [$\mathrm{kmol\,m^{-3}\,s^{-1}}$]
μ_k	mobility [$\mathrm{m^2\,V^{-1}\,s^{-1}}$]
L	length of simulation domain [m]
D	diffusion coefficient [$\mathrm{m^2\,s^{-1}}$]
ϵ	electron energy [eV]
T	temperature [K]
F_0	normalized electron energy distribution function
k	index of species
λ	thermal conductivity [$\mathrm{W\,m^{-1}\,K^{-1}}$]
σ	momentum transfer cross section [$\mathrm{m^{-2}}$]
ϕ	equivalence ratio
c_p	constant pressure heat capacity [$\mathrm{J\,K^{-1}\,kg^{-1}}$]
S_L	flame speed [$\mathrm{m\,s^{-1}}$]
n	number density [$\mathrm{m^{-3}}$]
e	elementary charge [C]
N	gas number density [$\mathrm{m^{-3}}$]

ABSTRACT

Sustainability and climate change remain existential challenges due to the global dependence on the fossil fuels. Green energy technologies require additional investment and research before replacing conventional fossil fuels. Therefore, new technologies for increasing fossil fuel combustion efficiency and reducing harmful emissions are of critical importance. One such promising technology is plasma-assisted igition (PAI) and combustion (PAC). However, more research on the fundamental mechanisms of plasma-assisted combustion is needed to better understand the interaction between plasmas and flames for system optimization. This dissertation focuses on developing efficient, simplified models for plasma- and electric field-assisted combustion to investigate the effects of different plasma and electric field parameters on plasma-flame interactions.

To model electric field-assisted combustion, a one-dimensional (1D) premixed flame subjected to a microwave electric field is considered. An open-source code, Cantera, is modified to solve the conventional conservation equations together with Poisson's equation to account for the electric force between charged species. To accurately predict flame speed enhancement, non-thermal electrons are considered for both kinetics and mass transport. The results show that it is critical to use the electron energy distribution function (EEDF) for calculating electron recombination rates to improve the predictions of electron number density and flame speed. The effect of changing the electric field strength on the electron number density distribution and Joule heating efficiency is investigated, and it is found that an electric field strength of $E = 0.8$ kV/cm has the highest efficiency.

For modelling plasma-assisted combustion, a nanosecond repetitively pulsed (NRP) plasma discharge is placed in the oxidizer stream of a counter-flow diffusion flame. A computationally efficient model composed of a zero-dimensional (0D) plasma reactor model and an unsteady one-dimensional (1D) flame model is developed. The 0D plasma model incorporates detailed plasma chemistry including electron collision reactions, charge transfer reactions, dissociative reactions of oxygen, and relaxation of vibrational states. The open-source flame code, Ember, is modified to solve the unsteady 1D flame equations using the inlet gas composition from the 0D plasma to calculate extinction strain rate and ignition delay time. The calcu-

lations show that the extinction strain rate depends more strongly on the pulse repetition frequency (PRF) of the plasma than the flow rate of air through the plasma reactor. Furthermore, using a higher pulse repetition rate reduces the ignition delay, but makes flame ignition less energy efficient.

The low dimensional models developed in this work are useful for elucidating the mechanisms involved in plasma-assisted combustion and providing important flame properties for experiments and simulations involving plasma application in realistic combustion systems. The electric field and plasma-assisted combustion models developed here are much more accessible and computationally efficient than complicated multi-dimensional models. Therefore, the models can be readily implemented and modified by researchers in the wider combustion and energy science communities for investigating and developing plasma-based combustion technologies.

1. INTRODUCTION

1.1 Motivation

Sustainability of the environment, energy, and resources is critical for the future of the Earth and the next generations of humans who will inhabit it. Sustainability and climate change remain existential challenges due to the global dependence on the fossil-fuel-dependent economy. The global demand for liquid hydrocarbon fuels continues to increase annually. New methods for extracting fossil fuels have been developed, and we can now extract much more fossil fuel stored in the ground, but with higher cost and environmental impact. Even with increased investment in green energy technologies, the economies of most developed and developing countries still heavily depend on fossil fuels and will continue for the foreseeable future. For example, 80% of the energy consumed in the U.S. is from fossil fuels (37% petroleum, 32% natural gas, and 11% coal) [1]. It is difficult to change the fossil-fuel-dependent economy, and green energy will continue to be only a supplementary energy source as long as fossil fuels remain plentiful, readily available, cheaper, and more energy efficient. Therefore, developing strategies for reducing our consumption of fossil fuels and mitigating environmental damage is critically important.

In the U.S., transportation accounts for over one-third (35% in 2020) of our total energy consumption each year [1]. Personal vehicles are very popular, and an average person in the U.S. owns 0.84 cars [2] (2017 total number of all motor vehicles registrations divided by the number of population). While the cost of electrical vehicles (EVs) continues to decrease, energy density and efficiency remains a bottleneck to widespread replacement of traditional gasoline-powered cars with EVs. Gasoline has roughly 100 times the energy density by both weight or volume compared to an EV battery. Even if advancements in battery technology increase the energy density, EV batteries are still much more expensive than gasoline engines due to the expensive metals required for battery fabrication. Commercial air transportation also relies on fossil fuels, and this will likely continue for the foreseeable future since the low energy density of batteries make them impractical for long flights.

Technologies that improve the energy efficiency of existing fossil fuel-based engines do not have the same high barrier to economic transition as batteries because they still utilize

the same form of energy and infrastructure. Technologies for improving efficiency of internal combustion (IC) engines include using a high air-to-fuel (AF) ratio (fuel-lean operation) to reduce fuel consumption and exhaust gas recirculation (EGR) to reduce NO_x emissions. Fuel-lean operation is also a traditional approach for improving efficiency of gas turbine engines used for land-based power generation and aircraft propulsion. However, these technologies can cause combustion instabilities that reduce combustion efficiency and damage engine. Therefore, it is critical to continue to develop new technologies to optimize fuel-lean operation and to reduce harmful emissions to the environment. One promising approach is to enhance combustion using electric fields or plasmas, or "plasma-assisted combustion" (PAC).

1.2 Plasma and Electric Field-Assisted Combustion

1.2.1 Applications

Plasma-assisted combustion (PAC), including electric field-assisted combustion, is a promising technology for improving current internal combustion and gas turbine engines and developing new propulsion systems for extreme environments or conditions, such as hypersonic flow velocity, extremely low pressure and temperature, and ultra-lean fuel ratio. [3]. Extensive experimental work has applied PAC in IC engines, including using microwave fields [4]–[9], radio frequency (RF) electric fields [10]–[12], and nanosecond repetitive pulsed (NRP) plasma discharges [13]–[16]. Nishiyama and Ikeda (2012) [4] applied the electric field produced by magnetrons, which are used in microwave ovens, to spark-ignition (SI) IC engine ignition (spark plus microwave electric field). They showed that the IC engine with applied microwaves could achieve stable combustion with higher AF ratio and EGR rate. Mariani and Foucher *et al.* achieved similar effects by replacing a traditional spark plug with a radio frequency ignition system (RFSI). Shiraishi and co-workers [15], [16] applied nanosecond pulsed plasma for ignition in an IC engine instead of using a traditional spark plasma with time duration on the order of micro- or milliseconds. They obtained a 15% shorter ignition time using the nanosecond pulsed plasma compared to a traditional spark using a similar level of pulse energy. In addition, they showed that the ignition delay time could be further decreased by using shorter duration pulses that produce a higher electric field with the same

pulse energy. Finally, they also showed that NRP plasma discharges reduced the combustion time and increased A/F ratio at the limit of combustion stability by approximately 1.6 times compared to SI. Tanoue et al. [17] used NRP plasma to ignite methane and propane mixture in a single-cylinder gasoline engine. They showed that using NRP plasma improved the AF ratio from 20 to 23, EGR ratio from 17.5% to 22.5%, and thermal efficiency by 5%. More recently, Sjoberg et al. [18] showed that using NRP plasma to ignite gasoline (15% ethanol) can improve the efficiency of IC engine up to 17%.

Beyond the direct application to IC engines, experiments have been conducted using applied electric fields and plasmas on various types of flames, such as diffusion and jet flames [19]–[31], bluff-body stabilized flames [32]–[34], and swirl-stabilized flames [35]–[48]. In general, these experiments show that electric fields and plasmas can increase flame burning speed and improve flame stabilization, with potential applications to gas turbine engines used for both energy generation and aircraft propulsion. Another promising application of PAC is in high-speed and supersonic combustion, such as in an engine scramjet [3]. Some early studies in the late 1980s and 1990s [49]–[51] explored using a plasma torch as an igniter and flameholder in scramjet engines. For example, Sato *et al.* [50] showed that using a plasma torch extended the ignition limit and shortened the tail flame of a scramjet. Microwave fields have also been used for PAC in scramjets [52]. Esakov *et al.* [52] showed that a microwave generator with a radiating horn effectively initiated and sustained a propane-air mixture combustion torch in a cold supersonic stream. More recent studies have explored a range of PAC technologies for use with scramjet combustion, including gliding arc discharges [53]–[57], multi-point ignition using pulsed plasma with microwave fields [58], [59], quasi-DC plasma discharges [60]–[62], nanosecond pulsed plasmas [63], [64], and laser-induce plasmas [65].

To understand the physical mechanisms underlying the coupling between electric fields, plasmas, and flames and to optimize PAC technologies, we must investigate the effect of electric fields and plasmas on flame properties such as flame speed, flame temperature, and ignition delay time under well-controlled conditions. This need motivates the current study on the effects of microwave electric fields and nanosecond pulsed plasmas on a canonical

flame configuration, the counterflow diffusion flame. The following two sections review prior experimental PAC studies using microwave electric fields and nanosecond pulsed plasmas.

1.2.2 Effects of Microwave Electric Fields on Combustion

Microwave fields have been shown in several studies to improve the burning rate of flames [66]–[72]. Sullivan *et al.* [68] observed a 65% increase of the flame speed by applying a strong microwave electric field to a lean (equivalence ratio = 0.6) methane/air premixed flame. Stockman *et al.* [69] studied a methane/air premixed flame with equivalence ratios from 0.65 to 0.8 subjected to a continuous microwave electric field (maximum strength of approximately 5 kV/cm). They measured the flame properties using several diagnostics, including filtered Rayleigh scattering [73] (FRS) for the flame temperature, particle image velocimetry (PIV) for the flame speed, and planar laser induced fluorescence (PLIF) for OH concentration and the location of the flame front. They estimated the flame speed increase with the applied microwave field to be 5 to 20 % depending on equivalence ratio.

Pulsed microwaves (versus a continuously applied field) is a promising way to enhance combustion with higher efficiency. Stockman et al. [70], [74] showed that the energy cost using pulsed microwaves can be 50 times lower than continuous microwaves. Their experiments showed that an effective flame speed increase of 25% can be achieved using either 1.5 kW continuous microwave or 30 W pulsed microwave radiation. Also, the short-pulsed microwaves are less prone to electrical breakdown, which occurred with high levels of continuous microwaves and, in the worst case, can extinguish the flame. Michael et al. [75] investigated the effect of applying pulsed microwaves to an ultra-lean methane/air flame. They showed that microwaves with pulse frequency and energy of 1 kHz and 25 mJ, respectively, could sustain the flame front with equivalence ratio as low as 0.3 (the equivalence ratio limit is approximately 0.55 without microwaves).

For solid fuel combustion, the microwave radiation can be absorbed by both the gaseous and condensed phases to improve ignition and combustion. One advantage of microwave-assisted combustion is that the burning rate is adjustable by tuning the electric field strength of microwave. This is especially useful for combustion involving solid fuels, where the equiv-

alence ratio is fixed. Barkley et al. [76] investigated solid propellant flame enhancement by applying microwaves with alkali metal seeding. They showed that with a low degree of doping (3.5 wt%) using $NaNO_3$, applying the microwaves increased the burning speed by 27.5% with only 2 s of specific impulse lost.

1.2.3 Effects of Nanosecond Repetitively Pulsed (NRP) Plasmas on Ignition and Combustion

Nanosecond repetitive pulsed (NRP) discharges are a special class of plasma discharges that efficiently produce non-equilibrium plasmas with high reactivity at atmospheric pressure with low power input. Early investigations focused on the fast ionization wave (FIW) generated by the overvoltage of a single nanosecond pulse. The FIW typically travels 1 cm in just a few nanoseconds and generates a uniform large volume plasma at a very low pressure [77], [78]. The nanosecond pulse also excites molecules into high-energy states such as $N_2(A^3)$ (a nitrogen triplet state), which can accelerate fuel oxidation (hydrogen in the cited study) [79]. More recent studies have shifted from a low-pressure single nanosecond pulse to high-pressure (atmospheric) repetitive pulses [80]–[82]. Pai *et al.* (2010) [82] investigated three different regimes of NRP discharges in the pin-to-pin electrode configuration: spark, glow, and corona, which occur with different applied voltage, pulse repetition frequency (PRF), and electrode gap distance. They showed that the mechanism of regime transition of an NRP plasma differs from a traditional plasma, and that the NRP discharge method is more effective (lower preheat gas temperature and input power) at generating glow plasma [80]. In addition, the regime transition criterion indicates that the required preheat temperature for the glow regime decreases as the electrode radius of curvature decreases [82]. There are several differences between the glow and spark regimes. First, an NRP plasma in the spark regime produces significant heat over a very short (nanosecond-scale) time period, which induces a shock wave, while discharges in the glow regime do not produce a significant temperature rise [81]. Second, NRP plasmas in the glow regime rely on streamer initiation, while the initiation in the spark regime is spatially uniform [81]. Additionally, an NRP spark discharge generates a much higher (approximately 100 times) charge density than an NRP glow discharge, allowing the remaining electrons to be used to initiate the next pulse.

Plane-to-plane electrodes, most often with a dielectric barrier on one electrode (dielectric barrier discharge or DBD), are one of the most popular configurations for studying ignition by NRP discharges. At low pressures, discharges in the plane-to-plane configuration generate relatively uniform plasmas, which makes experimental measurements and numerical simulations via zero or one-dimensional models more tractable. Lou et al. [83] investigated the ignition/oxidation of premixed hydrocarbon-air flows by plane-to-plane NRP DBD discharges in the glow regime. The mixture was ignited with a non-thermal plasma, which has a much lower temperature than the auto-ignition temperature. Lou and co-workers found that the fuel can be oxidized with low-duty-cycle (1/500) NRP discharges even without ignition, and ignition can occur if the resultant flow heating is sufficiently high. They suggested that radicals such as O or OH created via low-temperature plasma chemistry are the major contributors to fuel oxidation, and the direct electron impact dissociation of fuel only has a minor effect on the fuel concentration. Different techniques have been used to investigate ignition by NRP discharges in a plane-to-plane configuration. Zuzeek et al. [84] investigated ignition of hydrogen-air mixtures using pure rotational coherent anti-Stokes Raman scattering (CARS) and the evolution of gas temperature during ignition measured by CARS agreed well with the kinetic model. They proposed three main reactions as the main oxidation process of hydrogen at low temperature for plasma-assisted ignition,

$$\mathrm{H} + \mathrm{O_2} + \mathrm{M} \rightarrow \mathrm{HO_2} + \mathrm{M} \tag{1.1}$$

$$\mathrm{O} + \mathrm{HO_2} \rightarrow \mathrm{OH} + \mathrm{O_2} \tag{1.2}$$

$$\mathrm{OH} + \mathrm{H_2} \rightarrow \mathrm{H} + \mathrm{H_2O} \tag{1.3}$$

where O and H atoms can be generated mainly by the discharge via electron impact and dissociation collisions with electronic metastable states of N_2. Yin et al. [85] (2013) investigated NRP discharge ignition of hydrogen-air mixtures using OH laser induced fluorescence (LIF) to simultaneously measure temperature and OH concentration. The resulting OH profile was

used to both identify the point of ignition and validate the kinetic model of low-temperature oxidation by NRP discharges. They proposed that the H atom is the main accumulated radical contributing to the acceleration of ignition based on the kinetic model. The ignition and oxidation of hydrocarbon fuels by NRP discharges has also been investigated [83], [86]–[88].

Another common electrode configuration for plasma assisted ignition with NRP discharges is pin-to-pin (two pointed-tip electrodes separated by a gap), which has higher ionization efficiency compared to plane-to-plane due to the higher field electron emission from the pin electrode (without dielectric barrier). However, NRP discharges in the pin-to-pin configuration generate filamentary and highly spatially-dependent plasmas that require more precise measurement techniques and two- or three-dimensional models. Lovascio et al. [89] found that the ignition time can be minimized with a certain pulse repetition frequency (PRF) when the total input energy is held constant. They explained that the PRF needs to be sufficiently high so that each pulse can take advantage of the heat and active radicals generated by the previous pulse, but not so high as to exceed the re-circulation frequency that is required to refresh the gas mixture between electrodes. They showed that the mean rate of energy deposition by the plasma is the key parameter to characterize ignition delay time. Lefkowitz and Ombrello [90] investigated the development time of a flame kernel produced by pin-to-pin NRP discharges. They showed that a lower PRF has a shorter flame kernel development time due to an increased volume of unburned mixture exposed to the discharge as long as the pulses are fully coupled (100% ignition probability for each pulse). They also investigated other parameters such as the electrode gap, equivalence ratio, pulse number, and flow velocity to optimize ignition. Overall, the flow field and heat transfer play much more important roles in ignition in the pip-to-pin electrode configuration than for the plane-to-plane.

NRP plasmas can also be used to enhance continuous combustion. Nagaraja et al. [91] designed a plasma-flame facility with a flat flame burner in a low pressure chamber. The laminar quasi-1D flame is enclosed in a uniform plasma generated by NRP discharges with the high voltage plane electrode downstream of the flame and the burner desk acting as the grounded electrode. They found that the high concentrations of radicals (O, H, and OH) generated by the low-temperature plasma moves the flame upstream. Pilla et al.[32]

investigated the influence of NRP plasmas to a bluff-body stabilized turbulent premixed flame by installing the NRP discharge in the re-circulation zone. They showed that the NRP plasma could extend the blow-off limit to both higher air flow rates and to lower equivalence ratios. Xu et al. [33] used OH laser-induced fluorescence (LIF) to study OH radical evolution in a bluff-body stabilized flame similar to the flame studied by Pilla et al. [32]. They showed that OH radicals produced by the NRP plasma were convected by the re-circulation flow to mix with the combustible gas and ignite the flame. Sabatino et al. [48] recently investigated the influence of NRP glow and spark plasmas on a swirl-stabilized flame at elevated pressures. They observed that NRP plasmas can extend the blow-off limit, and concluded that NRP spark plasma is more effective than glow plasma at pressures below 2 bar. They stated that at higher pressures, a significant portion of the NRP spark plasma energy is used to generate shock waves and vortices that disturb the flame stabilization. Lacoste et al. [92] studied the responses of a laminar premixed flame subjected to an acoustic wave, AC electric field, and NRP glow plasma with the intention of using plasma to control flame instability. They found the the flame transfer functions (FTFs) of acoustic wave and NRP plasma depended on the shape of the flame but not on the AC electric field.

1.2.4 Chemistry of Plasma-Assisted Ignition (PAI) and Combustion (PAC)

One of the most important elements for modelling plasma-assisted ignition (PAI) and combustion (PAC) is using a realistic plasma chemistry. Kossyi [93] proposed a detailed reaction mechanism for air plasma including 46 species and 445 reactions, which has been used as the baseline chemistry model for non-equilibrium plasma discharges in air in many later studies. Several researchers have employed zero-dimensional (0D) kinetics calculations to develop and validate reduced chemical mechanisms for PAI/PAC. Popov (2007) [94] developed a zero-dimensional model of a FIW for a combustible mixture of H_2, O_2, and N_2. The electric field strength was determined by Ohm's law with measured discharge current. The heating of vibrationally excited states of N_2 and H_2 was included in the energy equation. The simulation results agree well with the experiment data [95] of maximum densities of $H_2(a^3\sum_g^+)$ H_2O after the first pulse. Kosarev et al. [96] performed a zero-dimensional simu-

lation of PAI in CH_4-air-Ar mixtures. Although the proposed zero-dimensional model lacks important features, such as solving Poisson's equation for the electric field, the predicted ignition delay times agreed well with the experiments. Aleksandrov et al. [97] performed a similar zero-dimensional simulation adding nitrogen to the mixture, and found that the excitation of nitrogen to meta-stable states, which consumes a large fraction of the discharge energy, created a channel for oxygen dissociation. Bak and Cappelli [98] proposed a reduced reaction mechanism for air plasmas using the method of [99], and performed a quasi-0D simulation of NRP discharges in the glow and spark regimes (49 and 73 reactions for the glow and spark regime, respectively). The quasi-1D plasma model assumed the discharge diameter to be 400 µm, which is similar to the typical size of a filamentary discharge observed in the experiments for NRPs, so the diffusion of temperature and species concentration can be calculated. The model also used a voltage profile with a circuit equation to simulate the electric field, so the electron properties can be obtained by solving Boltzmann equation. The simulations coupled species, energy, and circuit equations, while incorporating diffusion and convection effects in the species and energy equations. The reduced reaction mechanism predicted very similar species profiles compared to the detailed mechanism with a large discrepancy only for ozone. Bak and Cappelli [100] extended the reduced air plasma reaction mechanism to methane-air mixtures and studied NOx formation in NRP discharge-assisted combustion by connecting the 0D plasma discharge model to a zero-dimensional reactor. The 0D plasma model assumes the discharge diameter to be 400 µm, which is similar to the typical size of a filamentary discharge observed in the experiments for NRPs, so the diffusion of temperature and species concentration can be calculated. The model also used a voltage profile with a circuit equation to simulate the electric field, so the electron properties can be obtained by solving Boltzmann equation. They applied NRPs to a methane-air mixture and investigated the kinetics of nitric oxide formation in the premixed combustion connected to the plasma discharge. More recently, Starikovskiy and Aleksandrov [101] wrote a detailed review of PAC reaction mechanisms that described different excited species and their roles for PAC/PAI.

1.3 One-Dimensional Flame Simulations

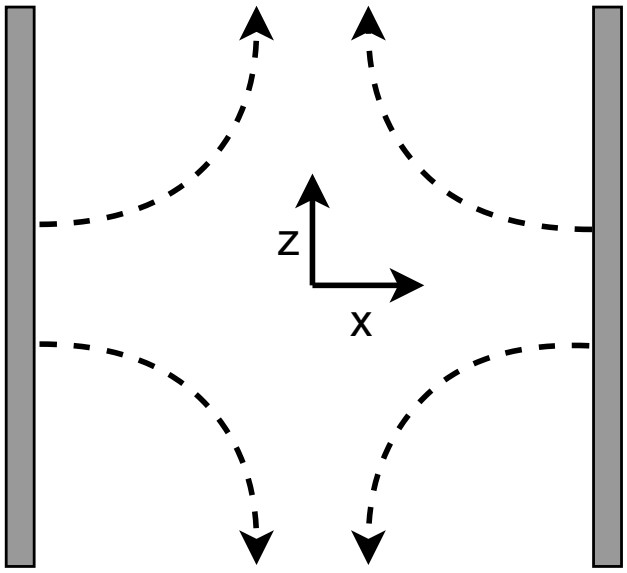

Figure 1.1. The schematic of an asymmetric stagnation flow.

Several flame properties, such as flame speed, flammability limits, and NO_x formation, can be obtained via 1D simulations. Of course, the 1D flame simulations are highly simplified and are not representative of most realistic combustion systems, which include multi-dimensional turbulent combustion. However, 1D flame simulations can still provide useful insight on flame characteristics and can be used to construct flamelet libraries for more complex combustion processes. Several software packages are available online for simulating 1D flames, such as Chemkin, Cantera, and Ember; the latter two are free and open source. One common configuration for 1D flame analysis is a counterflow flame stabilized in a axisymmetric stagnation flow field, as shown in Figure 1.1. The x-axis is the stagnation streamline and the z-axis is the stagnation plane. The velocity components are u and w in the x and z directions, respectively. The corresponding (non-reacting) potential flow field is given by [102], [103]

$$\begin{aligned} u_\infty &= -ax; \\ w_\infty &= \frac{az}{\beta}, \end{aligned} \tag{1.4}$$

where a is the strain rate. The factor β determines the flame geometry where $\beta = 1$ for a planar flame and $\beta = 2$ for a disc flame. Using the potential flow velocity field, the boundary layer approximation, and neglecting the second coefficient of viscosity, we can obtain the z-momentum equation along the stagnation streamline as

$$\rho\frac{\partial W}{\partial t} + \rho W^2 + \rho u\frac{\partial W}{\partial x} = \rho_\infty\frac{da}{dt} + \rho_\infty a^2 + \frac{\partial}{\partial x}\left[\mu\frac{\partial W}{\partial x}\right], \tag{1.5}$$

where $W = w/z$. The continuity equation becomes

$$\frac{\partial \rho}{\partial t} + \frac{\partial}{\partial x}(\rho u) + \beta\rho W = 0. \tag{1.6}$$

Reacting flow simulations require including the conservation equations for chemical species and energy. The conservation of species equation is given by

$$\rho\frac{\partial Y_k}{\partial t} + \rho u\frac{\partial Y_k}{\partial x} = -\frac{\partial \mathbf{j_k}}{\partial x} + \dot{\omega}_k W_k \tag{1.7}$$

and the conservation of energy equation is given by

$$\rho\frac{\partial T}{\partial t} + \rho v\frac{\partial T}{\partial x} + \frac{1}{c_p}\left(\sum_{k=1}^{K}\hat{h}_k\dot{\omega}_k + \sum_{k=1}^{K}\mathrm{j}_k c_{p,k}\frac{\partial T}{\partial x}\right) = \frac{1}{c_p}\frac{\partial}{\partial x}\left[\lambda\frac{\partial T}{\partial x}\right], \tag{1.8}$$

where $\mathbf{j_k}$ is the diffusion flux. Note that Equation 1.5 is not used for a non-strained 1D flame (freely propagating 1D flat flame) simulation in Chapter 2.

1.4 Objectives and Contributions

Motivated by the promise of PAC demonstrated by experiments for a range of practical combustion systems, this thesis focuses on using numerical modeling to investigate the fundamental effects of electric fields and plasmas on 1D flames. The first objective of the present study is to develop models with improved chemistry, species transport, and energy partitioning for electric field- and plasma-assisted flames. Specifically, this work focuses on the affect of (1) microwave electric fields and (2) non-equilibrium plasma produced using nanosecond repetitively pulsed (NRP) discharges on 1D flames. Regarding microwave

electric field-assisted flames, several studies have simulated a one-dimensional flame with an applied electric field, but the electric field strength was not high enough to have strong non-equilibrium effects [104]–[106]. Thus, prior models do not permit accurate prediction of flame speed enhancement due to strong applied microwave electric fields. Regarding NRP plasma-assisted flames, while significant work has been done on modeling NRP discharges, very few studies have performed simulations with full coupling of NRP plasma and combustion. Specifically, there is a lack of comprehensive simulations of even 1D planar flames subjected to NRP discharges. Such simulations would provide a simple and efficient tool for investigating the mechanisms of plasma-flame coupling under various conditions. Therefore, the first objective of the present study is to extend traditional 1D flame solvers into suitable numerical tools for investigating PAI and PAC. The second objective is to investigate the role of different plasma-flame coupling mechanisms (e.g. chemistry and gas heating) in affecting macroscopic combustion properties, such as ignition delay time, flame speed, and flame stability/dynamics, and explore how the coupling is affected by the plasma characteristics. In meeting these objectives, the current work makes the following contributions:

1. **Modelling of Microwave-assisted Combustion.**

   Manuscript title: Simulation of flame speed enhancement of a hydrocarbon flame with a microwave field

   To model the application of a microwave electric field to a 1D flame, we made significant modifications to the 1D flat flame code in Cantera [107]. Specifically, we

   (a) Added the ability to calculate the distribution of charged species, including coupling Poisson's equation to the conservation equations and implementing the accurate transport model *Stockmeyer*-(n,6,4).

   (b) Incorporated the properties associated with non-equilibrium plasma calculated by BOLOS [108] using the gas temperature and composition at each location in the 1D flame simulation. We make Cantera use the properties of non-equilibrium plasma for 1D flame simulation and iterate the simulation until converge. Notably, the correct calculation of the electron-ion recombination rates significantly

improved the model prediction of the flame speed compared to the experimental data.

(c) Implemented Joule-heating (Ohmic heating) in the microwave-assisted 1D flame simulation because primary purpose of microwaves is to heat the pre-existing free electrons created by chemi-ionization in the flame. We compared the flame speed enhancement percentage to the experiment [68], and confirmed that the primary mechanism for increasing the flame speed by a microwave electric field is the increase of flame temperature by Joule heating.

2. **Modelling of NRP plasma-assisted Combustion.**

Manuscript title: Numerical Analysis of a Nanosecond Repetitively Pulsed Plasma-Assisted Counterflow Diffusion Flame

To model the application of NRP plasma to a 1D flame, we develop a computationally efficient model which allows fast calculation of the flame properties and extinction strain rate (ESR). Specifically ,we

(a) Built a 0D plasma reactor model based on a perfect-stir reactor.

(b) Constructed a detailed methane/air plasma kinetic mechanism by combining the San Diego Mechanism [109] with plasma reactions.

(c) Modified the open-source 1D unsteady flame solver, Ember, to take the gas properties produced by NRP plasma as the flame inlet condition.

(d) Included "fast" heating due to quenching of electronically excited nitrogen and "slow" heating due vibrational-translational relaxation in the model to predict the evolution of the gas and flame temperature during pulsing and the plasma afterglow.

3. **Investigating Effects of discharge parameters**

(a) For microwave assisted combustion, we studied the effect of changing electric field strength on the electron distribution and the efficiency of Joule heating in the 1D flame.

(b) For NRP plasma-assisted combustion, we investigated the effect of NRP plasma (placed in the oxidizer stream) on the extinction behavior and ignition delay of a 1D counterflow diffusion flame and the effect of the plasma repetition frequency. We found that increasing the plasma PRF is more effective than increasing the gas residence time (or decreasing flow velocity) in the NRP plasma for extending the extinction strain rate. In addition, low PRF plasma is more efficient (requires fewer pulses) to ignite the flame but has longer ignition delay time compared to high PRF plasma.

1.5 Structure of the Dissertation

There are two main chapter in this thesis. Chapter two, *Simulation of Microwave Assisted Combustion*, models the effects of a microwave electric field on premixed flame, and discusses the effects of changing electric field strength. Chapter three, *Simulation of NRP Plasma-assisted Combustion*, models the effects of nanosecond repetitive pulsed (NRP) plasma on a counter-flow diffusion flame, and discusses the effects of changing PRF and flow rate on extinction strain rate and ignition delay time.

2. SIMULATION OF MICROWAVE ELECTRIC FIELD ASSISTED COMBUSTION

This chapter has been previously published in *Combustion and Flame*. The manuscript title: *Simulation of flame speed enhancement of a hydrocarbon flame with a microwave field*. Authors: Bang-Shiuh Chen, Allen L. Garner, and Sally P.M. Bane.

2.1 Abstract

This study models the effect of microwave electric field on a premixed flame to achieve an accurate prediction of flame speed enhancement by considering non-thermal electron for both kinetics and mass transport. The results compare well against experimental data, and show that using electron energy distribution function (EEDF) to calculate recombination rates of electron is the key to improve the prediction of the electron number density and the flame speed. The resulting technique also agrees well with the flame speed theory to explain the mechanism of flame speed increase by ohmic heating, which is by increasing the flame temperature. The model can also predict the efficiency of flame speed enhancement for a microwave electric field. Finally, the model can be improved by incorporating recombination cross sections of major ions, if they are available.

2.2 Introduction

The use of externally applied electric fields to modify combustion has been a topic of interest for more than a century, with the earliest experimental investigation on modifying flame geometry published at the turn of the nineteenth century [110]. Over the following decades, numerous experimental studies applied electric fields to modify flames, including expanding blow-off and extinction limits, enhancing flame speed and stability, and reducing soot formation [67], [111]–[115]. Marcum, et al. [116] detailed the principal results from experimental studies through 2005. A more recent study showed that applying a strong but sub-breakdown external DC electric field increased the flame speed by less than 8% for a premixed methane/air flame [117]. In another experimental study, a strong microwave

electric field increased the flame speed by more than 65% for a lean (equivalence ratio =0.6) methane/air premixed flame [68]. However, a robust model to predict the degree of flame speed increase under applied electric fields is lacking.

Three primary mechanisms have been proposed to explain the effect of an applied electric field on a flame. The first mechanism involves producing "ionic wind," where ions in a flame are accelerated by an external electric field and then transfer momentum to neutral particles via collisions [118], [119]. This mechanism is restricted to DC or lower frequency electric field so that the ions have enough time to drift in the direction of electric field. The second mechanism is gas heating, where electrons gain energy as it moves in an electric field and then transfer energy to neutral particles by elastic and inelastic collisions [120]. A third mechanism involves altering the flame kinetics by producing radical or excited chemical species, which requires to optimize several conditions such as gas composition, electric power, and temperature for the production rates [121]. The method of using microwave to enhance a flame belongs to the last two mechanisms.

The most recent numerical model of microwave flame speed enhancement by Ju, et al. [120] modeled a one-dimensional methane-air flame with a strong external applied AC microwave electric field (up to 2.0 kV/cm). They modified the energy equation by adding ohmic heating, which was the only mechanism of flame speed enhancement considered in their simulation. The authors showed that ohmic heating produced by an applied microwave electric field can increase the flame speed up to 30%, which agreed qualitatively with similar experiments [66] [122]. However, the model predicted much lower flame speed enhancement than observed experimental result [68]. Therefore, Ju and co-workers suggested further model refinement to achieve quantitative agreement with experiments.

Free electrons play an important role in the coupling between applied external electric fields and a flame. In a hydrocarbon flame, free electrons exist due to chemical ionization within the flame itself [123], [124]. Goodings, et al. [125] conducted a seminal experimental study of ions in atmospheric pressure methane-oxygen premixed flames at both lean (ϕ = 0.216) and rich (ϕ = 2.15) conditions. Gas sampling and mass spectroscopy was used to identify approximately forty species across the flame, providing by far the most detailed measurement of ion profiles in flames available in the literature. The other popular method

for measuring total ion density in a flame uses a Langmuir probe. MacLachy, et al. [122] provides a summary of studies using this method through 1978.

In addition to experimental measurements, several researchers have attempted to predict ion concentrations in flames using numerical simulations. Pederson and Brown [104] modeled a one-dimensional flame with an applied external voltage to study the effect of electric fields on the ionic structure of methane flames. Poisson's equation was solved with the standard conservation equations for a one-dimensional laminar flame and an assumed temperature profile obtained from experimental measurements. The conservation equations for charged particles were modified by adding an electric drift term to the mass flux to account for the ambi-polar diffusion effect. Pederson and Brown observed that the ratio of peak ion concentration to total ion concentration predicted by their simulation was reasonably close to experimental results [125] without an applied external voltage. The same study used simulations to predict the saturation current by increasing the applied voltage and comparing the predictions to experimental measurements. While this study considered a constant applied voltage, the range of voltages considered was not specified.

Few, if any, numerical studies on electron/ion density in laminar flames were published between Pederson and Brown's seminal work in 1993 [104] and a subsequent study by Prager et al. in 2007 [126]. Prager and co-workers modeled a lean methane/oxygen one-dimensional flame with no external electric field, with three primary differences from the earlier work of Pederson and Brown. First, they coupled the conservation equation for energy to the mass and momentum equations instead of assuming an experimental temperature profile. Second, they assumed quasi-neutrality (zero total charge flux) in the flame and used detailed transport based on Chapman-Enskog theory [127]. Third, they added negative charged species and their associated reactions to the kinetic mechanism used in [104] to account for the attachment of electrons to oxygen molecules and the subsequent reactions. This expanded ion chemistry improved the agreement between their simulated ion profiles [126] and experimental data [125].

Several years later, Han and co-workers [128] modeled the same flames using the detailed ion reaction mechanism suggested by Prager et al [126]. They improved the model by replacing the ambi-polar diffusion term with the traditional drift-diffusion flux and solving

Poisson's equation for the electric field. Han et al. also improved the transport model used for the ions by updating the empirical data and investigating the effect of polarizability.

In most of these prior numerical studies, the primary focus was obtaining more accurate predictions of ions and electrons in a flame and therefore an external applied electric field was not included, except for Pederson and Brown [104], who applied a low external electric field to calculate saturation current. More recently, Speelman, et al. [106] modeled a one-dimensional methane/air flame with an external applied DC voltage of -250 to 250 V. This model calculated the electric field using Poisson's equation and included a drift term in the conservation of species equation. A highly simplified ion reaction mechanism was used that included an electron and two positive ions (HCO^+ and H_3O^+) with three reactions: the chemi-ionization reaction producing HCO^+, a proton transfer reaction, and the recombination reaction of H_3O^+. Their simulations showed that the chemi-ionization rate, recombination rate, and the diffusivity of the electron and H_3O^+ are critical for determining electrical properties such as conductivity and saturation current, and that these parameters can be adjusted to fit experimental data [129]. Due to the relatively low electric field strength used in the model, the electrons were assumed to be thermal and thus solving Boltzmann's equation was not required. Also, this model did not include detailed transport as in Ref. [126]. While the models in Refs. [104] and [106] both included an external electric field, they only considered the relationship between the current and voltage in the flame and not the effect of the applied field on the flame speed. Also, they only considered relatively low electric fields and thermal equilibrium between the gas and electrons.

The present study proposes a new model to predict the structure and speed of premixed one-dimensional flames subject to microwave electric fields (up to 50 Td) but below electrical breakdown (around 140 Td). This new model couples Poisson's equation, drift diffusion equation, and modified energy equation to account the transport of ions/electron and temperature gain. In addition, the ohmic heating term is added to the energy equation as the main mechanism of flame speed enhancement. We use GRI3.0 and USC kinetic mechanisms for neutral species and an updated ion chemistry model based on the model of [126] to predict electron density with higher accuracy. Finally, this model uses the Boltzmann equation to obtain the electron diffusion coefficient, electron mobility, ohmic heating, and the reaction

rates of major reactions involving electrons (dissociative recombination). Although we retain the same mechanism as the simulation of Ju et al. [120], we include the effect of non-thermal electron to improve the prediction of electron number density. The governing equations are solved by coupling the open-source code Cantera with the Boltzamnn equation solver BOLOS. The input files for Cantera and BOLOS are available as supplementary material.

2.3 Theory

This section first outlines the governing equations and modifications introduced before presenting the chemical reaction model and explaining the solution process. Table 2.1 shows the modifications that this study makes to the the conventional one-dimensional flame model. We assume a quasi-steady state and neglect the frequency effect of microwave due to the large time scale difference between the flow ($10^{-3}s$) and microwave radiation ($10^{-9}s$) according to [120].

Table 2.1. The modification to the conventional one-dimensional flame governing equation

Equation	modification
species equation	add drift term
energy equation	add ohmic heating source term
Poisson's equation	new equation to calculate electric field
Boltzmann equation	new equation to evaluate electron energy distribution function
chemical source term	include production rate of positive ions and electron evaluated from electron energy distribution function (EEDF) and cross sections

2.3.1 Species equations

The conservation of species equations for a one-dimensional, laminar premixed flame can be written in mass fraction form as[103]

$$\rho u \frac{\partial Y_k}{\partial z} = -\frac{\partial \mathrm{j}_k}{\partial z} + \dot{\omega}_k W_k \,, \tag{2.1}$$

where ρu is constant due to continuity. This study solves for the inlet velocity (flame speed) as an eigenvalue of these equations. Applying a sufficiently strong electric field to a flame necessitates solving the conservation equations for ions and relevant plasma species in addition to neutral atoms and molecules. Thus, we supplement a standard chemistry mechanism for combustion of neutral species with reactions for the ion chemistry. The rates for reactions involving plasma species are calculated by solving the Boltzmann equation. Section 2.3.5 discusses the chemistry calculations in greater detail.

Two factors primarily contribute to the species mass flux j_k [104], [105], [128], [130]: diffusion and drift. We use mixture-averaged diffusion for computational efficiency, and add the drift term due to the internal electric field created by charged species in the flame. Therefore, in this study the total mass flux is written as

$$\begin{aligned} \mathrm{j}_k &= \mathrm{j}_k{}^* - Y_k \sum_{\mathrm{i}} \mathrm{j}_\mathrm{i}{}^*, \\ \mathrm{j}_k{}^* &= -\rho \frac{W_k}{\overline{W}} D_k \frac{\partial X_k}{\partial z} + s_k \mu_k E Y_k, \end{aligned} \tag{2.2}$$

where s_k is the sign of charge, which equals 1,-1, and 0 for positively charged, negatively charged, and neutral, respectively. $\overline{W}$ is mean molecular weight. The superscript $*$ denotes the diffusive flux before correction for ensuring zero total flux. The boundary conditions for Equation (2.1) for neutral species are

$$\begin{aligned} &\dot{m}_0 Y_{k,\mathrm{in}} - \mathrm{j}_k - \dot{m}_0 Y_k = 0 \text{ for } z = 0, \\ &\frac{\partial Y_k}{\partial z} = 0 \text{ for } z = L\,. \end{aligned} \tag{2.3}$$

Note that the boundary condition for neutral species on the left boundary ($z = 0$) ensures that the combined flux due to diffusion and convection equals the flux of inlet gas composition. The simulation fails to converge for the standard boundary condition of Equation 2.3 applying to charged species; therefore, we apply a Neumann boundary condition for electrons and ions, given by

$$\frac{\partial Y_k}{\partial z} = 0 \text{ for } z = 0, L\,. \tag{2.4}$$

The internal electric field E is obtained from Poisson's equation [104]. The system of governing equations is "stiff" and failed to converge using standard form of Poisson's equation (second-order discretization). Therefore, we use the differential form of Gauss's law (first-order discretization) for its simplicity and more efficient computationally compared to Poisson's equation, given by

$$\begin{aligned} &\frac{\partial E}{\partial z} = \frac{\mathrm{e}}{\epsilon_0}(n_+ - n_-), \\ &E(z=0) = 0. \end{aligned} \tag{2.5}$$

where the subscript $+$ and $-$ means positive and negative charged species respectively. Simplified models for ambi-polar diffusion such as charge neutrality require that the Debye length be much smaller than the simulation domain and are therefore only applicable in the heat releasing region of the flame where the density of charged particles is relatively high. Poisson's equation or Equation (2.5) is more general and its applicability is not limited to certain regions of the flame.

2.3.2 Energy equation

A term accounting for ohmic heating due to an external applied electric field is added to the conventional energy equation. It is assumed that all energy absorbed from the external electric field instantly transfers to the gas due to high collision frequency of electron and gas molecules in a flame. The internal electric field induces negligible heating. Note that we do not consider heating of water molecules via absorption of microwaves since the absorption coefficient of the water vapor due is several orders of magnitude lower than that of the electron (as shown in the supplementary material). This allows us to write the energy balance and appropriate boundary conditions as

$$\rho u c_p \frac{\partial T}{\partial z} = \frac{\partial}{\partial z}(\lambda \frac{\partial T}{\partial z}) - \sum_k \mathrm{j}_k c_{p,k} \frac{\partial T}{\partial z} + \sum_k h_k W_k \dot{\omega}_k + \mathrm{e}\mu_\mathrm{e} E_{ex}^2 n_\mathrm{e}, \tag{2.6}$$

$$T(z=0) = T_u, \tag{2.7}$$

$$\frac{\partial T}{\partial z}(z=L) = 0, \tag{2.8}$$

where E_{ex} is the strength of the external electric field, T_u is the temperature of unburned fuel and air mixture, and n_e is electron number density. Note that electrons primarily contribute to the ohmic heating due to their significantly higher mobility compared to ions. Bisetti and co-workers [131] showed that the power of ohmic heating depends on the electron number density and electric field strength, and is typically only few percent of the chemical heat release for low density (1.0×10^{16} [m^{-3}]) with sub-breakdown reduced electric field strength (less than 100 Td). However, Ju et al. [120] showed that ohmic heating can still have a significant effect on flame speed for low electron density (1.0×10^{16} [m^{-3}]) of electron.

2.3.3 Transport model

The classical model to account for inter-molecular potential, the Lennard-Jones potential, was proposed by Jones [132] in 1924. Han, et al. [128] used more accurate models, $Stockmayer - [n, 6, 3]$ and $Stockmayer - [n, 6, 4]$ potential [127] to model the transport of neutral species and ions, respectively, in a flame with updated constants obtained from fitting experimental data. Han, et al. also considered the interaction between charged particles using the Coulomb collision model [133]. However, due to the relatively low concentration of ions in the flames considered in the present study, we neglect the collisions between two charged particles to improve computational efficiency.

Table 2.2 summarizes the potentials and methods used to model the binary transport coefficients in the current simulations. Note that only the major species in a hydrocarbon flame O_2, CO_2, CH_4/C_3H_8, H_2, H_2O, and CO are used to calculate the binary diffusion coefficients with the $Stockmayer - [n, 6, 4]$ model and the cross sections.

Table 2.2. Binary collision model used in the present study. The models in parentheses are included in Han's simulation [128].

Solution	Neutral	Ion	Electron
Solute			
Neutral	LJ	Neglect ($[n, 6, 4]$)	Neglect(Cross-sections)
Ion	$[n, 6, 4]$	Neglect (Coulomb)	Neglect (Coulomb)
Electron	Cross-sections	Neglect (Coulomb)	Neglect (Coulomb)

2.3.4 Boltzmann equation

The application of a strong external electric field in this study necessitates solving Boltzmann's equation to determine the electron energy distribution function (EEDF) of non-equilibrium electrons. The Boltzmann equation of electron using spherical coordinates in velocity space is

$$\frac{\partial f}{\partial t} + v\cos\theta\frac{\partial f}{\partial z} - \frac{\mathrm{e}}{m}E\left(\cos\theta\frac{\partial}{\partial v} + \frac{\sin^2\theta}{v}\frac{\partial f}{\partial\cos\theta}\right) = C[f] \tag{2.9}$$

where f is the electron distribution, v is the magnitude of velocity, θ is the angle between the velocity and the field direction and C represents the rate of change in f due to collision. f can be expanded with the following two-term approximation for a high frequency field,

$$f(v, \cos(\theta), z, t) = f_0(v, z, t) + f_1(v, z, t)\cos(\theta)\exp(\mathrm{i}\omega t), \tag{2.10}$$

where ω is angular frequency of the electric field. Using Equation 2.10 and the temporal growth model [134], Equation 2.9 becomes,

$$-\frac{\gamma}{3}\frac{\partial}{\partial\epsilon}\left[\left(\frac{E_0}{N}\right)^2\frac{\tilde{\sigma}_m\epsilon}{2(\tilde{\sigma_m}^2 + q^2)}\frac{\partial F_0}{\partial\epsilon}\right] = \tilde{C}_0 + \tilde{R}, \tag{2.11}$$

where $\tilde{\sigma}_m$ refers to the corrected total momentum transfer cross section, $\gamma = (2\mathrm{e}/m)^{1/2}$ (e is the elementary charge and m is the electron mass.), $q = \omega/N\gamma\epsilon^{1/2}$, $\tilde{C}_0$ is the collision term, and $\tilde{R}$ is the growth-renormalization term. Hagelaar et al. [134] states that Equation 2.11 is also valid for a space-dependent EEDF, and can be used to evaluate electron properties

for a microwave electric field because the electron energy lost over one field cycle is small ($\omega/N \gg (2m/M)\sigma_m\gamma\epsilon^{1/2}$, where M is the mass of gas molecule).

Several terms in the governing equations and rates of reactions involving electrons will depend on the EEDF, including the electron mobility (μ_e) and diffusion coefficient (D_e), average electron energy ($<\epsilon>$) or electron temperature, and electron-energy-dependent reaction rate (k)(reaction 4 in Table 5). These terms are calculated from the EEDF using the following equations:

$$<\epsilon>=\int_0^{+\infty}\epsilon^{3/2}F_0 d\epsilon. \tag{2.12}$$

$$\mu_e=-\frac{\gamma}{3N}\int_0^{+\infty}\frac{\epsilon}{\tilde{\sigma}_m}\frac{\partial F_0}{\partial\epsilon}d\epsilon. \tag{2.13}$$

$$D_e=\frac{\gamma}{3N}\int_0^{+\infty}\frac{\epsilon}{\tilde{\sigma}_m}F_0 d\epsilon. \tag{2.14}$$

$$\mathrm{k}=\gamma\int_0^{+\infty}\epsilon\sigma_k F_0 d\epsilon. \tag{2.15}$$

Bisetti and Morsli [131] showed that one can solve the Boltzmann equation independently at each point for the properties of electrons because the mean free path of electrons is much smaller than the length scale of the reaction zone in a flame. Section 2.3.6 provides more detail concerning the coupling of the solution of the Boltzmann equation and the flame solver.

2.3.5 Chemistry

Two neutral-species mechanisms, the GRI-Mech 3.0 mechanism [135] and the reaction mechanism for C3 combustion of [136], are used for methane and propane, respectively. We use the mechanism proposed by Prager et al. [126] with some modifications for the ion chemistry. This ion mechanism [126] includes 67 reactions and 11 charged species and is the most detailed one available in the literature for a hydrocarbon flame. The reactions are listed

in Table A.1 in Appendix A. Several modification are made to the mechanism to improve the prediction of number densities of electrons and other major ions. First, the reaction rate coefficient of recombination between the most abundant positive ion, H_3O^+, and electron is calculated by Equation 2.15 rather than using a standard Arrhenius formula. According to Neau, et al. [137], the temperature dependence of the reaction rate coefficient changes from $T^{-0.83}(T < 1000K)$ to $T^{-1.10}(T > 1000K)$; therefore, it is more appropriate to use the electron energy distribution function and the cross section data [137] of H_3O^+ to calculate the rate coefficient. In contrast, Han et al. [128], [138] and other studies use Arrhenius-type reaction coefficients. Figure 2.1 shows the rate coefficients versus electron temperature calculated from the EEDF and cross section data and the Arrhenius formula used by Han et al. The crossing point between the two rate coefficients is near the flame temperature (1500 to 2000 K), but the difference grows larger when the temperature is farther away from the crossing point. For example, the external electric field in the current study can increase the electron temperature up to 8000 K, which results in a significant difference in the reaction rate coefficient. Also shown in Figure 2.1 is the constant recombination reaction rate coefficient used by Ju *et al.* [120] in their simulations. This reaction rate is much higher than the rates calculated using both the current method (EEDF and cross section) and the Arrhenius formula with data from [139] at higher electron temperature. Note that there are other important positive ions in a flame such as $C_2H_3O^+$ and CH_5O^+ in Prager's simulation[126]. The recombination rates should also be calculated using cross section data of the ions, but H_3O^+ is the only species with its cross section found in the literature. Second, Han et al. [138] shows that using Prager's model significantly overestimates the densities of $C_2H_3O^+$ and CO_3^-. To address this issue, Han et al. [138] proposed including Reactions 63 and 64 and defined Reaction 43 as irreversible; we make the same modifications in the current study. Third, the ion-ion recombination rate coefficients are updated. The estimated rate coefficients for ion-ion recombination of positive ions $C_2H_3O^+$ and CH_5O^+ and negative ions in Prager et al. [126] do not have references. There are three different reaction rate coefficients for two-particles, ion-ion recombination, as shown in Table 2.3 [93], [140].

Therefore, the reaction rates of Reactions 45 to 52 are updated with the estimated coefficients. Fourth, ion-ion recombination reactions of the major ion species (O_2^-, OH^-, HCO^+,

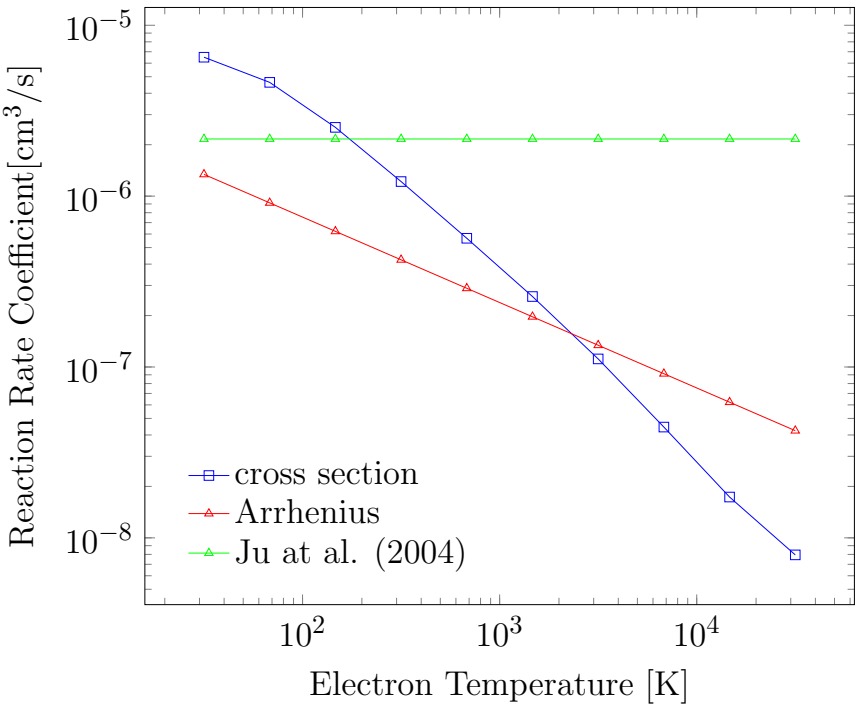

Figure 2.1. Comparison of reaction rate coefficients obtained using the EEDF and cross section data [137], Arrhenius formula (data from [139]), and the constant reaction rate coefficient of [120]. The EEDF is assumed to be a Maxwell-Boltzmann distribution function of electron temperature.

Table 2.3. Reaction rate coefficients of two-particle ion-ion recombination. A, B, and C are chemical products of recombination reactions.

reaction	A	B	E
$A^- + B^+ \Rightarrow A + B$	2.09×10^{18}	-0.5	0.0
$A^- + BC^+ \Rightarrow A + B + C$	6.02×10^{16}	-0.5	0.0
$AB^- + C^+ \Rightarrow A + B + C$	6.02×10^{16}	-0.5	0.0

and H_3O^+) are included to prevent unusually high densities of charged species from appearing at the boundaries. The complete ion reaction mechanism is given in Table A.1 in Appendix A.

It is worth to mention that we do not use the chemistry proposed by Bisetti et al. (2018) [141], which use a modified AramcoMech 1.4 [142], [143] with an updated ion chemistry to predict ions in a flame more precisely, because it required more computational time for its large number of reactions. They improved the chemistry by comparing CH concentrations and I-V curves with experimental data (although there is still some difference to the experiment.). We will incorporate it to our simulation in the future. Also, we do not consider excited oxygen such as $O_2(a^1\Delta_g)$, which have faster reaction rates by Starik et al. [144], because the reduced field (20 to 50 Td) in the current simulation is lower than plasma discharge and could not generate enough $O_2(a^1\Delta_g)$ (threshold energy at 0.977 eV) to have a significant impact. The amount of $O_2(a^1\Delta_g)$ to have a significant effect on flame speed is approximately 5% in oxygen [145], [146]. The reaction rate coefficient of $O_2(a^1\Delta_g)$ for 20-50 Td reduced electric field strength is on the order of 10^{-17} $m^3\,s^{-1}$ at the peak of reaction zone [131]. The electron number density of current simulation is around 2×10^{16} m^{-3} and the number density of oxygen is around 10^{24} m^{-3}. Considering a 1 mm reaction zone and 20 cm/s flow speed (residence time around 5×10^{-3}s), we have approximately 0.4% of $O_2(a^1\Delta_g)$, which is too low to produce significant a non-negligible increase in the flame speed. As for nitrogen, most electronic excited states require more than 6 eV, so their concentrations are even lower than $O_2(a^1\Delta_g)$. Also, we do not consider the vibrational excited states because of the high rate of vibrational-translational relaxation.

2.3.6 Simulation method

The one-dimensional premixed flame code in Cantera software [107] was modified for the current model and is used to solve Equations (2.1),(2.5), and (2.6) , while the open-source Boltzmann equation solver BOLOS [108] is modified to facilitate the use of high frequency field as shown in Section 2.3.4. The solution strategy is to gradually build up the elements of the model over three stages to ensure convergence is achieved at each step.

Stage one. The conventional form (without the electric drift and and ohmic heating terms) of Equations 2.1 and 2.6 are solved using Cantera. The chemistry includes neutral and charged species but no plasma reactions, i.e. the source term in Equation 2.1 does not include production or depletion of plasma species. The diffusion of charged species is turned off, and ions are convected with the neutral flow. This first solution stage provides reasonable profiles of the charged species to use as the initial guess for stage two.

Stage two. In this stage, Poisson's equation 2.5 is solved for the internal electric field and coupled with the species equation by including the electric drift term in Equation 2.1. Equations 2.1 and 2.6 are then solved again, including the electric drift term with charged species diffusion activated. This solution stage yields an accurate profile of electrons in the flame without an external electric field. Since there is no applied external electric field in this stage, the electrons are thermal. Bisetti et al. [131] has shown that $0.4\,\mathrm{m}^2/\mathrm{Vs}$ is a good estimate for the electron mobility μ_e and the electron diffusion coefficient D_e is calculated using the Einstein relation.

Stage three. In the third and final solution stage, the external electric field is applied to the flame. Boltzmann's equation is solved using BOLOS [108], with gas temperature and mole fractions of major species passed from Cantera to obtain the EEDF and to calculate electron properties/parameters via equations (2.12), (2.13), (2.14), and (2.15). We list the major species and the database for their complete cross-section data, which is available as supplementary material, in Table 2.4 for calculating the EEDF. When passing parameters such as electron mobility, electron diffusivity, and reaction rate coefficients back from BOLOS to Cantera, a five-degree polynomial curve fit is used to make parameters functions of gas temperature to ensure that new points can still assess data during grid refining. In this

solution stage, we first obtain the new electron profile in the flame using the transport properties, electron temperature, and production rates of recombination obtained from EEDF calculated from BOLOS. Next, the effect of ohmic heating (the $e\mu_e E^2 n_e$ term in Equation 2.6) is turned on. All properties mentioned above is turned on gradually by multiplying the external electric field strength by a fraction and slowly raising this fraction to unity. Finally, several iterations are performed until the program converge.

Table 2.4. Major species cross section.

Species	Database	Ref.
C_3H_8	Morgan	[147]
CO_2	Morgan	[147]
H_2	Morgan	[147]
H_2O	Morgan	[147]
O_2	Morgan	[147]
CO	Phelps	[148]
N_2	SIGLO	[149]

2.4 Simulation Result

The current model simulates the effects of an applied microwave electric field on a lean propane-air flame, because the electron number density has been verified with the experiment in Appendix B, which alleviates the issue of uncertainty of reaction rate coefficients. First, we investigate the electron profile in the flame without ohmic heating and how the profile is affected by the recombination rate for H_3O^+ (Arrhenius reaction rate vs. rate based on electron energy) and electron transport parameters. Second, the model is used to predict the flame speed increase via ohmic heating with an applied microwave electric field and compare with experimental measurements. Finally, we propose an improved model which uses an estimated effective dissociative recombination cross section for $C_2H_3O^+$. The inlet gas conditions of all simulations discussed in this section are set to the same conditions of the experiment of Sullivan et al. [68], propane/air with equivalence ratio of 0.6 at room temperature and atmospheric pressure. And we set the origin at $T = 0.75T_u + 0.25T_{ad}$,

where T_{ad} is the adiabatic temperature. All cross sections for calculating the EEDF and the effective recombination cross section of H_3O^+ are from [150] and [137], respectively.

2.4.1 Effect of Applied Microwave Electric Field on Flame Properties

This work proposes several improvements to the model for a one-dimensional flame with an external electric field. The most significant improvement over previous models is treating the electrons as non-thermal under strong applied electric fields. The solution to Boltzmann's equation is coupled to the flame model to calculate the local electron energy distribution function. The EEDF is then used to calculate electron temperature, electron mobility, electron diffusion coefficient, and rates for reactions which involve an electron as a reactant. The most recent and complete model in the literature considered the electrons to be in thermodynamic equilibrium with the heavier particles and used Arrhenius-type reaction rates for recombination reactions between electrons and positive ions [128]. Note that to calculate rate coefficients of recombination between positive ions and electrons, effective dissociative recombination cross sections are required. Only the effective dissociative recombination cross section of H_3O^+ can be found in [137]. Therefore, only the recombination rate coefficient of H_3O^+ (Reaction 4 in Table A.1) is calculated using BOLOS. For example, the cross section of $C_2H_3O^+$ is not available in literature.

To demonstrate the importance of including non-thermal electrons, flame profiles under external applied electric fields are calculated using the current model and then compared with profiles calculated using the approach of Han et al., which treated the electrons as thermal. Note that it is difficult to compare different models when ohmic heating is included because it can significantly alter the temperature profile and hence the reaction rates. Therefore, ohmic heating is excluded for the simulations in this section to facilitate comparison of the two models.

We consider a lean ($\phi = 0.6$) premixed propane/air flame with an applied microwave electric field of strength $E = 1.0$ kV/cm and frequency $f = 2.45$ GHz. The USC C3 mechanism [136] for propane combustion is combined with the ion chemistry discussed in Section 2.3.5 and given in Table A.1 in Appendix A. As discussed previously, the two most

important changes in the current model compared to the most recent model in the literature [128] are 1) calculation of the H_3O^+ recombination rate as a function of the EEDF; and 2) calculation of electron mobility/diffusivity using the EEDF. First, the relative effect of these two changes on the calculated flame profile is investigated. Figure 2.2(a) shows the profiles without external electric field. Both profiles of 1) and 2) are very close to the reference profile using Arrhenius-type expression for recombination reaction and constant assuming electron mobility [128]. This is expected because under these conditions (no applied external electric field and moderate temperature) the electrons will be thermal ($T_\mathrm{e} = T_{gas}$). The profiles may differ slightly because the Arrhenius rate coefficient from [139] is intended for use in astrochemistry and the applicable temperature range is only 10-1000 K. However, under an applied external electric field as shown in Figure 2.2(b), non-thermal electrons significantly change the electron profile. In general, the reaction rate of recombination reduces as the electron energy increases, so the electron number density is higher for profile of 1) comparing to the reference profile. Also the external electric field increases the electron temperature which increases the rate of ambi-polar diffusion ($D_a = D_+(1+T_\mathrm{e}/T_{gas})$) making the electron profile of 2) broader with a lower peak value. These results demonstrate the important of using the current model to better simulate the effects of applying a strong external electric field to the flame.

We next investigate the combining effect of 1) and 2). Figure 2.3(a) shows the electron temperature distribution through the flame for increasing strength of the applied electric field. For $E = 0.4$ kV/cm, the electron temperature is much higher than the gas temperature in the pre-heat zone but only slightly higher for the rest of the domain, but for $E > 0.4$ kV/cm the electron is non-thermal for the entire domain. Figure 2.3(b) compares electron profiles for different electric field strengths calculated using the current model, where both the H_3O^+ recombination rate and electron mobility depends on the EEDF and hence the electron temperature. For $E < 0.4$ kV/cm the energy gained of electron from the external electric field is mostly dissipated by collisions with heavy particles after position 0.5 mm and thus electrons are mostly thermal and the electron profile is close to the profile without the external electric field. Increasing E causes a broader electron profile, lower peak number density, and higher number density down-stream of the flame. Again, these calculations

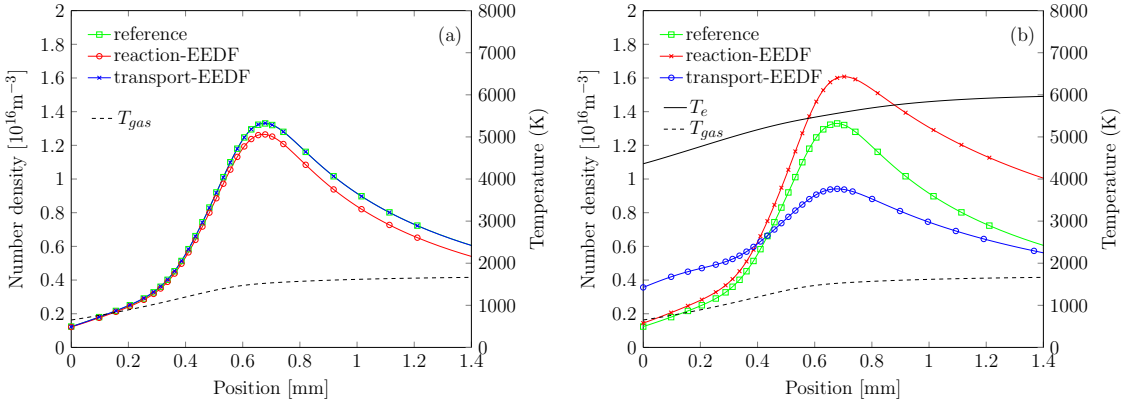

Figure 2.2. The effect of the H_3O^+ recombination rate and electron mobility on the electron density profiles across a premixed lean ($\phi = 0.6$) propane-air flame both with and without an applied microwave electric field. The reference profile is calculated using the Arrhenius-type reaction rate for H_3O^+ recombination. The mobility of electrons is assumed to be constant ($0.4\,m^2/Vs$) and the diffusion coefficient is calculated using Einstein's relation. The profile "reaction-EEDF" and "transport-EEDF" use BOLOS to calculate the recombination reaction rate coefficient and the electron mobility/diffusivity from EEDF, respectively. (a) without external electric field; (b) with an applied microwave electric field (E =1.0 kV/cm, f = 2.45 GHz).

show that the effects considered by the current model are important when simulating flames with applied electric fields, especially for strong electric fields.

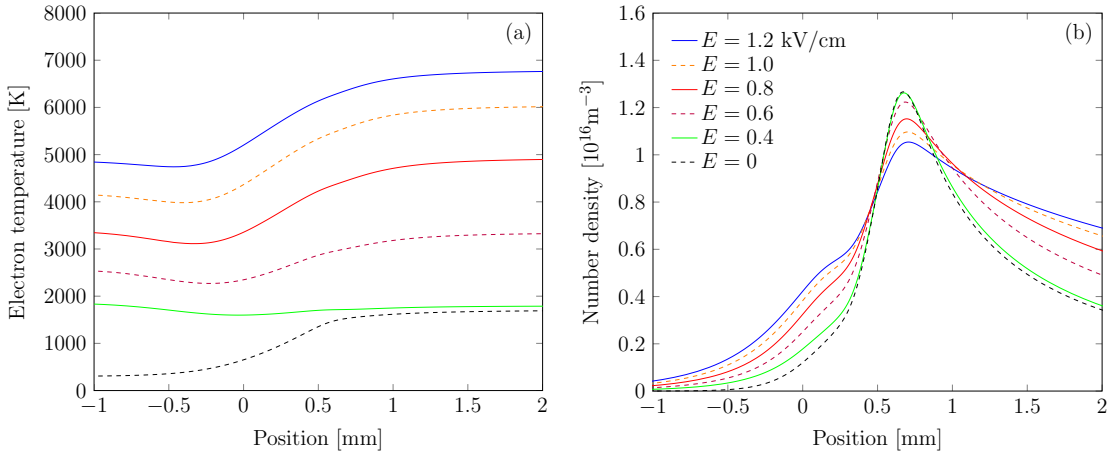

Figure 2.3. Calculated profiles of (a) electron temperatures with increasing electric field strengths. (b) Corresponding electron densities. The profiles are calculated using the current model with the recombination rate of H_3O^+ electron mobility dependent on the EEDF under an applied microwave (2.45 GHz) without ohmic heating effect. Note the curves represent external electric field strengths of 1.2, 1.0, 0.8, 0.6, 0.4, and zero, respectively, (unit in 1.0 (kV/cm)) looking from top to bottom in front of 3.5 cm position.

2.4.2 Flame Speed Enhancement with Applied Microwave Electric Field

To demonstrate the capabilities of the current model, the effect of an applied microwave electric field on the laminar flame speed is investigated. Many studies [66]–[72] have shown that microwaves can enhance the flame speed. Here, the flame speed enhancement with an applied microwave field predicted by the model is compared with the experimental results of Ref. [68] for a propane/air flame with equlivalence ratio of 0.6. In their work, a burner with a stagnation flow field was used to produce a flat flame (with only small curvature), and the flame speed was estimated from the height of the flame above the burner deck using a known flow velocity field from simulation. The burner was placed in a microwave cavity of WR430 rectangular waveguide. The microwave was generated by a high power magnetron with power level of 1300 to 4500 watt. The system produced a resonant standing wave, and

the maximum electric field strength for a given incident microwave power P was estimated as

$$P = 6.63 \times 10^{-4} ab \sqrt{1 - \frac{f_c^2}{f^2}} {E_{max}}^2, \tag{2.16}$$

where f is the operating frequency (2.45 GHz), and the waveguide dimensions are $a = 10.9\,\text{cm}$, $b = 5.46\,\text{cm}$, and $f_c = 1.372\,\text{GHz}$ depend on the waveguide and given in the reference [68]. The present study uses a field increase ratio of 5.433 due to resonance (multiplier to E_{max}) so that a power level of 4500 W corresponds to a maximum electric field strength of 2.0 kV/cm as suggested in [68]. Although the geometry and setup might affects the accuracy of flame speed, the percentage of relative flame speed increase should be more reliable. Therefore, we calculate the percent increase of the flame speed with the applied electric field using the current model and the approach of Han et al. (thermal electrons) and compared them with the experimental results from [68] in Figure 2.4. Both the experiment and the simulation use the same inlet composition of propane/air with $\phi = 0.6$. As done before in Section 2.4.1, the effects of the H_3O^+ recombination rate and the electron mobility are considered separately and together, as shown by the different curves in Figure 2.4. First, applying the approach of Ref. [128], which using the Arrhenius-type expression for the recombination rate and constant electron mobility significantly underestimates the flame speed increase. Similar predictions are obtained when including the effect of the EEDF on the electron mobility. The prediction of the flame speed enhancement improves when the EEDF is used to calculate the H_3O^+ recombination rate, but is still underestimated. In this case, the effect of non-thermal electrons on the recombination rate is most important in accurately predicting the flame speed increase.

The present model uses the cross section of H_3O^+ and the EEDF to obtain its recombination rate with non-thermal electrons. However, as discussed in Section 2.3.5, there are other important recombination reactions, such as that of $C_2H_3O^+$, where Arrhenius reaction rates are still used due to the lack of cross section data for dissociative recombination. This could have a significant impact on the flame speed prediction via lower predicted ohmic heating

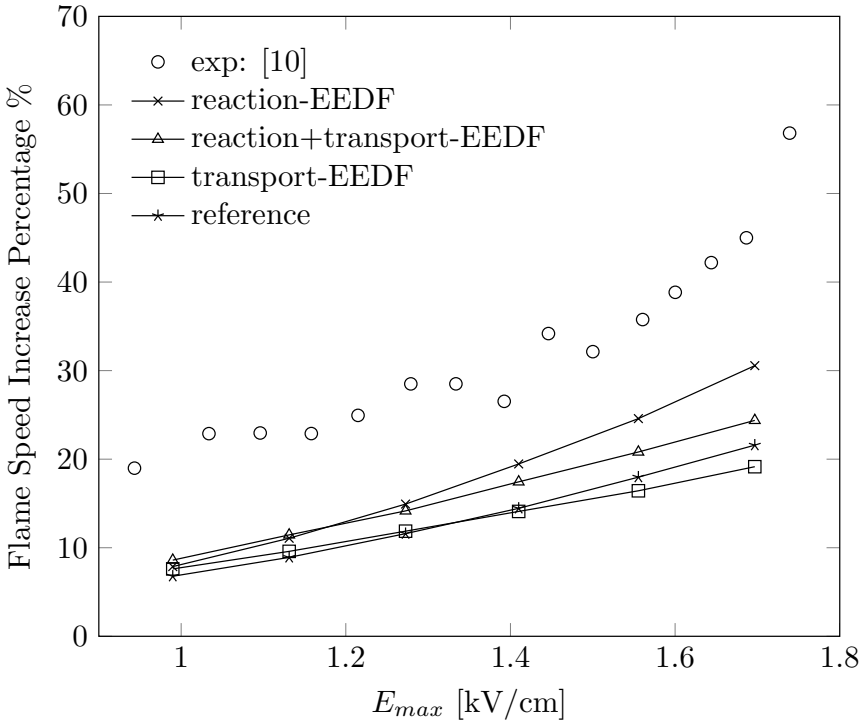

Figure 2.4. Comparison of percent increase in the flame speed of simulations to experiment [68] for a propane/air premixed flame with equivalence ratio of 0.6 as a function of the amplitude (rms) of a microwave field strength, which is calculated with equation 2.16. The curve "reaction-EEDF" means the reaction rate coefficient of dissociative recombination between H_3O^+ and electrons is calculated using the EEDF obtained from the Boltzmann equation with the cross section data of [137] while assuming constant mobility ($0.4\,m^2/Vs$) and the Einstein relation for electron transport. The curve "transport-EEDF" refers to the transport calculated using the EEDF while the reaction rate coefficient is calculated with Arrhenius formula with parameters from [139]. The reference curve is calculated without either change.

due to inaccurate calculation of the electron number density. To address this issue, a slightly modified chemistry model is proposed and discussed in the next section.

2.4.3 Model Improvement by Estimating $C_2H_3O^+$ Cross Section

As discussed previously, the rates of several ion recombination reactions cannot be determined accurately at high applied electric fields due to the lack of cross section data. As shown in the previous section, neglecting non-thermal electrons in the recombination rates of all major positive ion species dramatically underestimated the effect of the applied electric field on the flame. Also, we observed that the updated recombination reaction rate coefficients of $C_2H_3O^+$ and H_3O^+ from [139] are comparable ($4.54\times10^{-7}T^{-0.5}$ and $6.26\times10^{-7}T^{-0.5}$ $cm^3\,mol^{-1}\,s^{-1}$, respectively). To address this issue, it is reasonable to assume that the effective dissociative recombination cross section data of the other major positive ion, $C_2H_3O^+$, is similar to that of H_3O^+. Thus, the reaction rate coefficients of Reactions 8 and 10 in Table A.1 can be estimated using the cross section of H_3O^+. We refer to this approach as the "improved model," and the model using an Arrhenius reaction for $C_2H_3O^+$ recombination as the "original model." Figure 2.5 shows the predicted profiles of charged species for the same conditions as the experiment described in Section 2.4.2. First, in Figures 2.5(a) and (b), it is shown that the profiles obtained using the Arrhenius-type reaction rate coefficient for $C_2H_3O^+$ recombination ("original" model) and the cross-section data ("improved" model) are very similar without an external electric field. This ensures that the improved model is consistent with the original model in the case with no applied field. In Figures 2.5(c) and (d), the profiles are calculated with the applied electric field ($E = 1.0$ kV/cm) but neglecting ohmic heating. In this case, the number densities of ions and electrons are higher with the improved model due to the change of the rate coefficient of dissociative recombination of $C_2H_3O^+$. In Figures 2.5(e) and (f), including ohmic heating further increases the difference between the two models. The higher electron density resulting from improved estimation of $C_2H_3O^+$ recombination results in higher ohmic heating. In general, the profiles calculated using the original model are not as strongly affected by the applied electric field and ohmic heating.

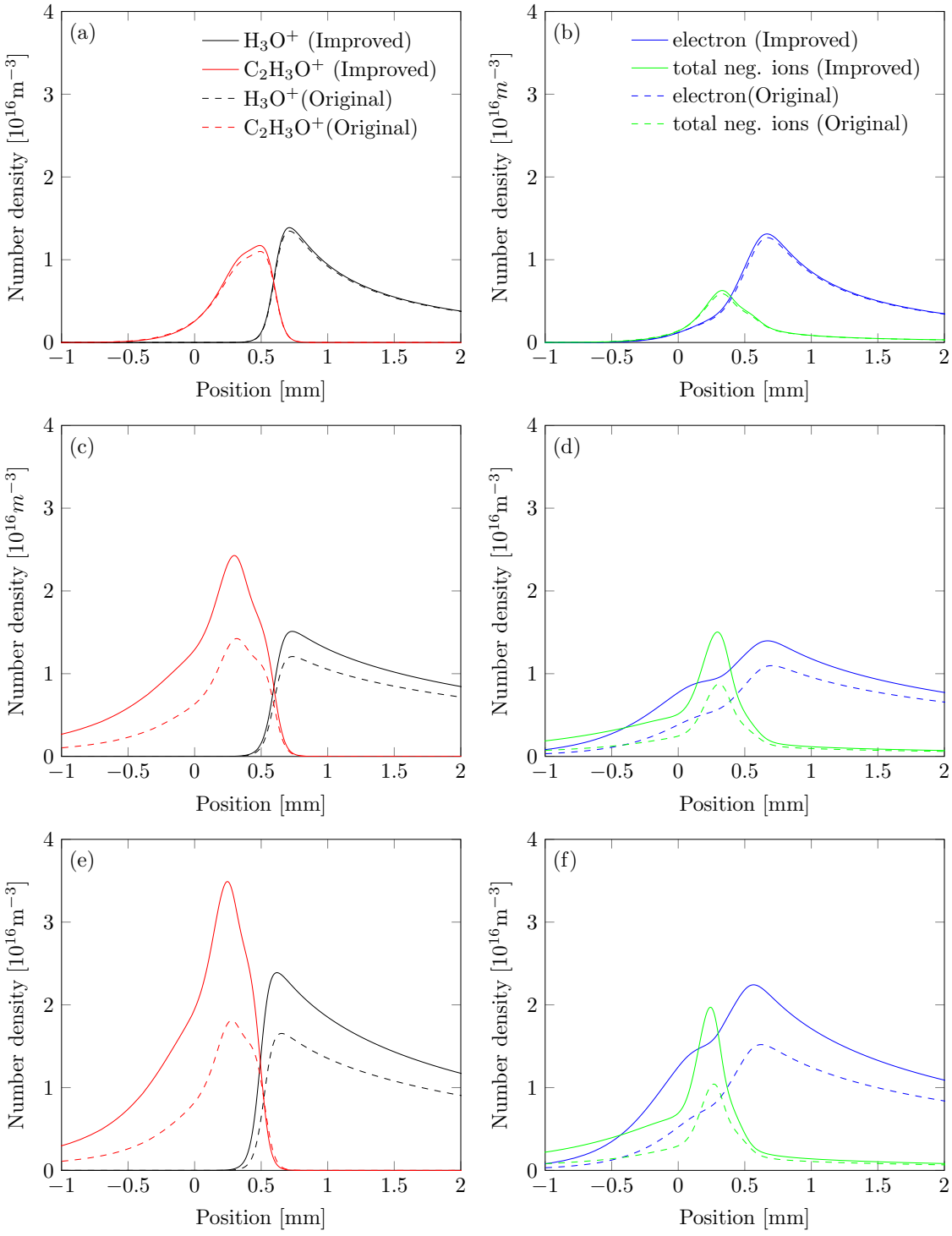

Figure 2.5. Comparison of profiles of charged species calculated using the "original" model (Arrhenius-type reaction rate for $C_2H_3O^+$ recombination) and the "improved" model (estimate of $C_2H_3O^+$ cross section data). (a), (b) No applied electric field; (c),(d) applied electric field ($E = 1.0$ kV/cm, $f = 2.45$ GHz), neglecting ohmic heating; (e),(f) applied electric field and ohmic heating included. Note the figure legends of (c) and (e) follow (a), while (d) and (f) follow (b).

Figure 2.6 (a) shows the flame speed increase calculated using the improved model, i.e. using cross section data and the EEDF to calculate recombination rates for both H_3O^+ and $C_2H_3O^+$. Compared to the results obtained using the original model shown in Figure 2.4, the predicted flame speed increase is significantly higher and agrees much more closely with the experimental data. Figure 2.6 (b) shows that the flame speed increases as ohmic heating increases. Although the percentage of flame speed increase is not exactly proportional to the ohmic heating, the results suggest that ohmic heating is the primary mechanism for flame speed enhancement and is proportional to the number density and electron mobility.

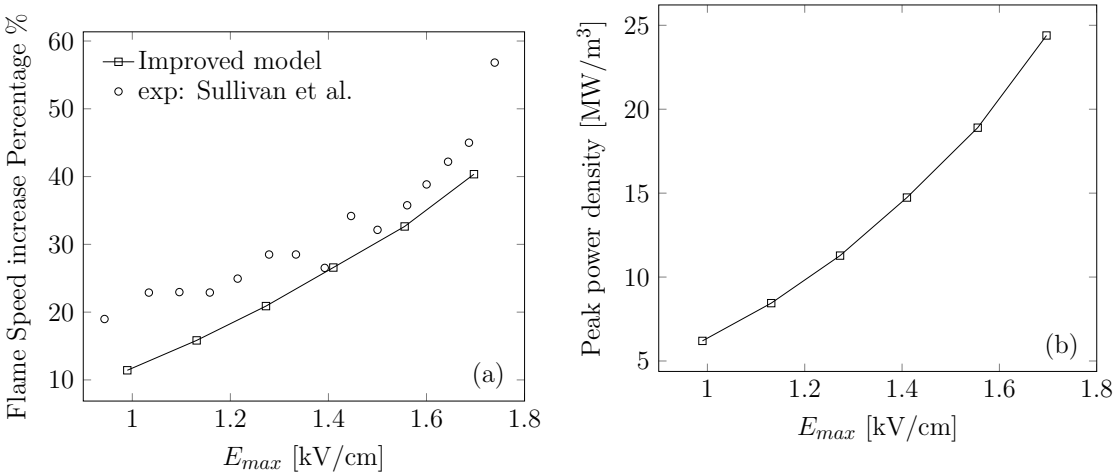

Figure 2.6. (a) Comparison of percent increase in the flame speed between experiment [68] and the improved model for a propane/air premixed flame with equivalence ratio of 0.6 as a function of the amplitude (rms) of a microwave field strength (E_{max}), which is calculated using Equation 2.16. (b) The corresponding peak power densities of ohmic heating of the simulation.

We then look into the detail of the ohmic heating, chemical heating and temperature profiles of the case with $E = 1.0$ kV/cm for both origin and improved models. Figure 2.7(a) shows that the improved model results in much higher ohmic heating compared to the original model, especially near the flame's heat release zone. Figure 2.7(b) shows that the chemical heat release for the improved model starts slightly further upstream and has a higher peak value. According to this plot, the boundary between the pre-heat and heat release zones is located approximately at the origin, and the thickness of heat release region is around 1 mm. Although the ohmic heating is approximately one order of magnitude smaller than

chemical heating, it raises the flame temperature slightly and thus promotes the feedback process of chemical heat release. Figure 2.8(a) shows the temperature profiles of the flame with and without electric field. The temperature profiles with electric field deviate from the case without electric field (reference flame). Figure 2.8(b) compares the temperature difference between both models and the reference flame (no electric field). With an applied electric field, the flame speed is higher and the flame thickness is thinner so the temperature of pre-heat zone is lower than the reference flame. The improved case has the fastest flow rate, so that the temperature is the lowest. In the flame reaction zone, the temperature difference begins to increase due to ohmic heating and the associated increase in chemical reaction rates. The improved model has the highest temperature in the reaction zone due to higher ohmic heating. Finally, the temperature continues to increase in the burned region due to the heating of residual electrons by the electric field.

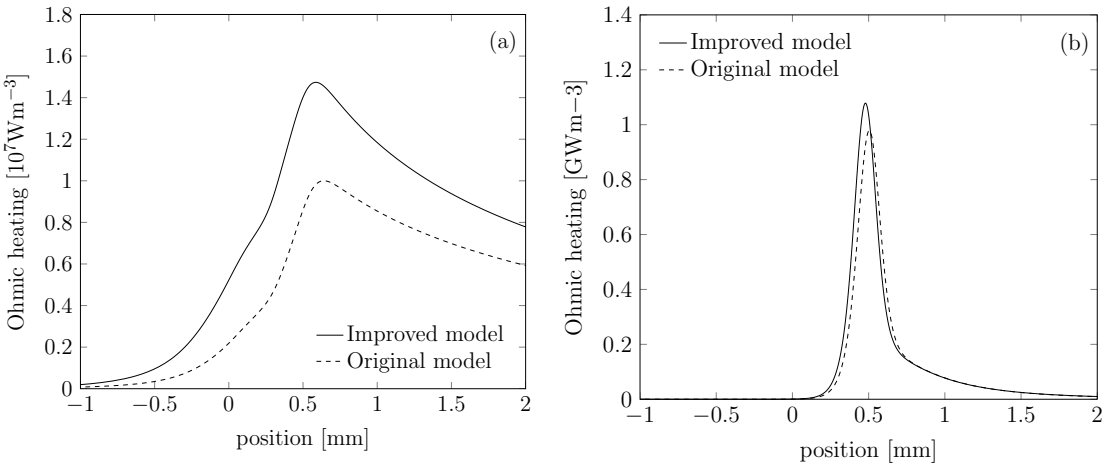

Figure 2.7. Comparison of (a) ohmic heating and (b) chemical heating determined using the original vs. improved models. The electric field strength is 1.0 kV/cm.

According to the theory of Zeldovich and Frank-Kamenetskii [151], the laminar flame speed can be estimated using a simplified model that assumes two-step combustion with separate preheat and reaction regions. In the preheat region, the heat source term is assumed to be zero. In the reaction region the thermal convection term is assumed to be much smaller than the thermal diffusion term and is therefore neglected. Matching the solution of two equations (dT_{i}/dx) at the boundary between two regions results an simplified expression for

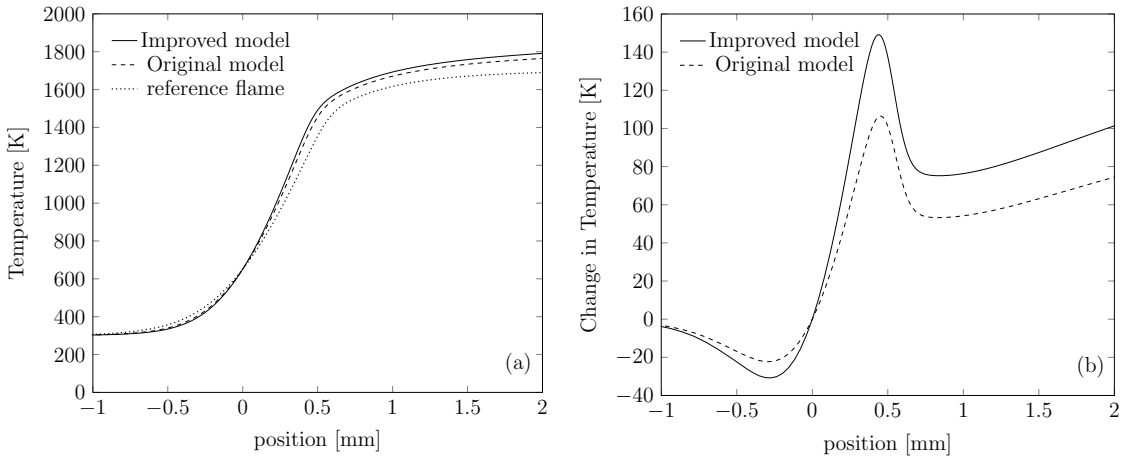

Figure 2.8. (a) Calculated temperature profiles using the original and improved model compared to the reference flame with no electric field. (b) The difference between the temperature of the reference flame and the original and improved models. The electric field strength is 1.0 kV/cm.

flame speed. However, for the case with an external electric field the heat source term in the preheat region is not zero but is equal to the ohmic heating rate. Therefore, the energy equation in the preheat region becomes

$$\lambda \frac{dT}{dx}|_{\mathrm{i}} \approx \rho S_L c_p (T_{\mathrm{i}} - T_u) - \int_{-\infty}^{z_{\mathrm{i}}} \dot{q}_{ohmic} dz, \tag{2.17}$$

where the subscript i means the interface between pre-heat and chemical reaction zone, and T_u and T_b is the unburned and burned temperature, respectively. In the reaction region with an applied electric field the heat source term is the combination of chemical heating and ohmic heating, yielding

$$\lambda \frac{dT}{dx}|_{\mathrm{i}} \approx \sqrt{2 \int_{T_{\mathrm{i}}}^{T_b} \lambda (\dot{q}_{chem.} + \dot{q}_{ohmic}) dT}, \tag{2.18}$$

where $\dot{q}_{chem.}$ is the power density of chemical heating. Matching the two equations at the boundary between the preheat and reaction regions and considering T_{i} is nearly the same value (figure 2.7), we obtain an expression for the laminar flame speed as

$$S_L \approx C(\sqrt{2\bar{\lambda} \int_{T_{\mathrm{i}}}^{T_b} (\dot{q}_{chem.} + \dot{q}_{ohmic}) dT} + \int_{-\infty}^{z_{\mathrm{i}}} \dot{q}_{ohmic} dz), \tag{2.19}$$

where C is a constant and $\bar{\lambda}$ is the mean thermal conductivity. Since ohmic heating is more than an order of magnitude smaller than chemical heating, it is reasonable to neglect ohmic heating in the term under the square root, i.e. $\dot{q}_{chem.} + \dot{q}_{ohmic} \approx \dot{q}_{chem.}$. Equation 2.19 can be used to estimate the percent increase in flame speed due to the ohmic heating. Assuming the thermal conductivity is approximately 0.1 W/mK, the first term on the right hand side of Equation 2.19 is approximately 227.4 kW and 242.7 kW for the original and improved models, respectively. The second term on the right hand side, which corresponds to the total ohmic heating in front of the heat release region (pre-heat zone), is estimated to be approximately 0.629 kW and 1.618 kW for the original and improved models, respectively. This effect directly accounts for less than 1% of the flame speed increase, so we can also neglect it. Note that ohmic heating is still affecting the temperature by heating the gas. Therefore, the original formula of Zeldovich and Frank-Kamenetskii is still suitable in this case if the

flame temperature profile is known. According to the theory, We estimates the percent increase in flame speed to be 16.80% and 24.65% for the original and improved models, respectively, which is very close to the simulation results. Therefore, the main mechanism for flame speed increase via ohmic heating is through increasing the flame temperature (which indirectly increases the chemical heat releasing rate.). Since the mobility can be evaluated accurately by solving the Boltzmann equation, the most important factor for predicting an accurate heat flux due to ohmic heating is accurately predicting of the electron density profile. The improved model better accounts for the effect of non-thermal electrons on dissociative recombination and predicts higher electron number density and flame temperature, making it well-suited for predicting the flame speed with an applied external microwave electric field.

Lastly, we investigate the efficiency of microwave-flame-speed enhancement. This is by far difficult to achieve in an experiment because the amount of ohmic heating is difficult to be measured. Figure 2.9 shows the efficiency versus the position in the simulation domain. The position starts at 1 mm, where most of the heat releasing reactions have finished. After the heat releasing region, the efficiency decreases as the position because the ohmic heating power is wasted on heating up the burned gas via the residual free electrons. Therefore, it is desirable to cut the microwave after the heat releasing region, which does not affect the flame speed, to maintain a higher efficiency. In current simulation, the microwave with RMS strength close to 0.8 kV/cm has a higher efficiency with the maximum efficiency around 0.5 to 0.6. In reality, it is difficult to control the microwave to not heat the burned gas after the heat releasing region. However, this could be a key factor to improve the efficiency of flame speed enhancement by microwave.

2.5 Conclusion

This study develops an improved model for a one-dimensional laminar flame under the influence of a strong applied electric field, combining sophisticated transport theory, up-to-date chemistry, and non-thermal electron properties. The model can predict the increase in flame speed due to an external applied microwave electric field with reasonable agreement with experimental measurements. The results of the current work reveal that the key to

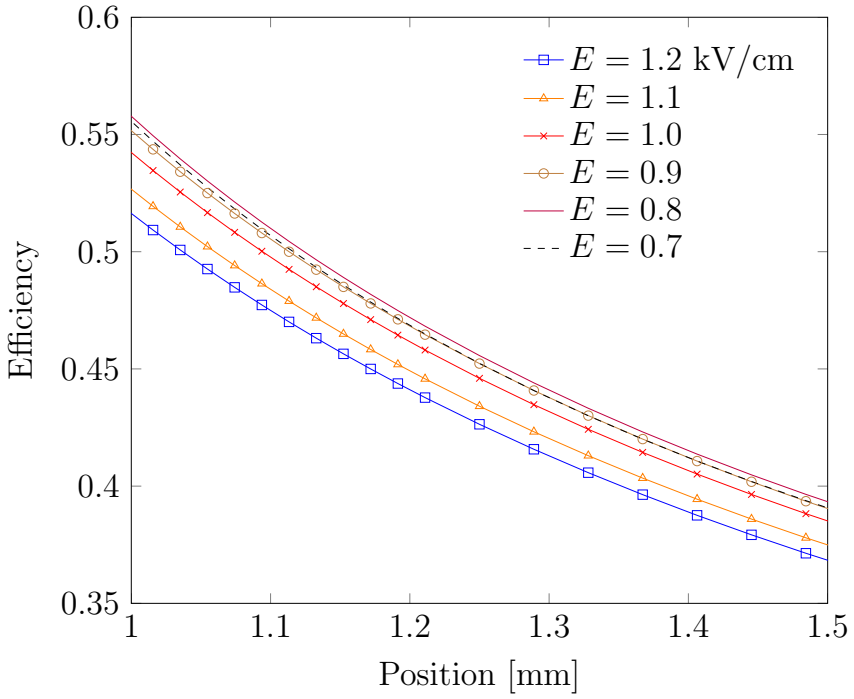

Figure 2.9. Efficiency of flame speed enhancement by applying a 2.45 GHz microwave to a propane/air flame at equivalence ratio of 0.6. The efficiency is defined as the ratio of accumulated power of ohmic heating to equivalent power of direct gas heating to a same amount of flame speed increase.

accurately predicting the effect of the applied electric field on the flame speed is using the EEDF to calculate electron-ion recombination rates, which has been overlooked in prior models. The results also show that the primary mechanism for increasing the flame speed via a microwave electric field is the increase of flame temperature by ohmic heating. It is demonstrated that ohmic heating can have a significant impact on a flame. We also investigate the efficiency of using microwave to increase flame speed, and show the potential improvement of the efficiency. Moreover, the ability of the current model to predict the degree of flame speed increase will be useful in investigating more complicated effects of applied external electric fields such as expanding blow-off limits, increasing flame stability, and reducing soot formation [111], [113], [115].

There are some limitation of current model. First, due to the lack of cross section data for $C_2H_3O^+$, the current model uses the cross section of H_3O^+. Although the model can predict the flame speed well compared to the experimental measurements with varying magnitude of electric field strength, it may be improved by adding the cross section data of $C_2H_3O^+$ and other major ionic species. Second, the model is limited to a low ionization rate, and we neglect the interaction of charged particles. For a gas with higher ionization degree (10^{-5}), coulomb collisions cannot be neglected, and we must include more cross section data of charged species to accurately calculate Boltzmann equation. Third, the model is limited to a sub-breakdown electric field strength. We still need to improve current model by adding the chemistry of the excited species such as $O_2(a^1\Delta_g)$ and using a detailed energy equation for different channels of heating. Expanding the model to higher electric field strength will permit the simulation of intense nanosecond electric pulse on a flame.

3. SIMULATION OF NANOSECOND REPETITIVE PULSED PLASMA ASSISTED COMBUSTION

This chapter has been submitted for publication and is currently under review. The manuscript title: *Numerical Analysis of a Nanosecond Repetitively Pulsed Plasma-Assisted Counterflow Diffusion Flame*. Authors: Bang-Shiuh Chen, Allen L. Garner, and Sally P.M. Bane.

3.1 Abstract

A computationally efficient model is proposed to analyze plasma-assisted combustion using nanosecond repetitive pulsed (NRP) plasmas. The NRP plasma discharge is placed in the oxidizer stream of a counter-flow diffusion flame. The effect of changing pulse repetition frequency (PRF) and flow rate of a continuous NRP plasma discharge on the extinction profiles of a counter-flow diffusion flame is investigated numerically. The results show that increasing PRF is much more efficient at extending the extinction strain rate than decreasing the flow rate. The model can also be used to simulate flame ignition using NRP plasma discharges. The results show that it is necessary to apply more pulses when using a higher PRF NRP plasma discharge even though these conditions have shorter ignition delay times.

3.2 Introduction

Over the past decade, plasma-assisted combustion (PAC) and ignition (PAI) have been widely studied for improving combustion efficiency across various applications, including land-based power generation, aviation gas turbines, and supersonic propulsion [3], [152], [153]. While thermal plasma ignition (i.e. spark ignition) has been used for over a century [154], interest in using both non-equilibrium and equilibrium plasmas for ignition and combustion control has increased dramatically in recent years. In particular, nanosecond repetitively pulsed (NRP) discharges have attracted significant attention due to their high chemical reactivity and energy efficiency due to their low duty cycles. NRP discharges mainly occur in three regimes, corona, glow, and spark. The glow and corona regimes have very modest temperature rise and the effect is primarily chemical, while the spark regime induces

rapid gas heating and thus has thermal and hydrodynamic effects in addition to chemical [80]–[82].

Several researchers have investigated plasma-assisted ignition (PAI) using NRP discharges. Using NRP discharges between pin-to-pin electrodes, Lovascio *et al.* [89] found that the ignition time of a propane-air mixture in a constant volume combustion chamber can be minimized with a certain pulse repetition frequency (PRF) for a fixed total input energy. They explained that the PRF needs to be sufficiently high so that each pulse can take advantage of the heat and active radicals generated by the previous pulse, but not so high as to exceed the re-circulation frequency (around 50–100 kHz for a 1 mm inter-electrode gap at 0.2 MPa), which is required to refresh the gas mixtures between electrodes. Lefkowitz and Ombrello [155] investigated the ignition probability of a methane/air flowing mixture using NRP discharges. They defined what they termed the "fully-coupled regime" where all discharges are applied to the same ignition kernel before it can be transported away from the electrode gap, and found that the ignition probability is higher in the fully-coupled regime than in the partially-coupled or decoupled regimes. They also found that the kernel size growth rate is larger with longer inter-pulse time within the fully-coupled regime. In a subsequent study [90], Lefkowitz and Ombrello investigated the development time of the flame kernel and showed that lower PRF promotes shorter flame kernel development time due to an increased volume of unburned mixture exposed to the discharge as long as the pulses were fully coupled.

In addition to PAI, NRP plasmas can also be used for enhancing a flame long after it has been established by the ignition kernel. Plasma can interact with flame with three mechanisms: kinetic, thermal, and hydrodynamic. Several configurations have been proposed to demonstrate the effect of NRP plasmas on a flame. In one configuration, the flame is enclosed in a large volume of plasma or the NRP plasmas are directly applied at the flame front. For example, Nagaraja *et al.* [91] designed a plasma-flame facility with a flat flame burner in a low pressure chamber. Uniform plasma was generated by NRP discharges with the high voltage plane electrode located downstream of the flame and the burner deck acting as the grounded electrode. They observed a 20% increase in flame temperature and up to 500% increase in radical OH concentration for a premixed $H_2/O_2/N_2$ flame. Nagaraja and co-workers

also performed numerical simulations of the plasma-assisted flame using a framework they developed in prior work [156] and compared with experimental results. They found that radicals (O, H, and OH) generated by the low-temperature plasma at the preheat region of the flame were the main cause of the observed displacement of the flame upstream. In another configuration for investigating plasma-assisted flames, the NRP plasmas were generated upstream of the flame. For example, Sun *et al.* [157] set up a counterflow burner in a low pressure chamber and installed a pair of electrodes upstream in the oxidizer flow. They observed that the flame with plasma generation upstream had a higher extinction strain rate than the flame without the plasma. One key difference between these two plasma-assisted flame configurations is the location of the plasma discharges: in the first configuration, the plasma is located near the flame front (or surrounding it) to generate radicals directly in the flame preheat region, while the second configuration uses the plasma to generate radicals upstream of the preheat region. While NRP discharges can generate many different radicals to enhance the flame speed, many radicals recombine rapidly at low temperature and high pressure [158]. Therefore, the second plasma-assisted flame configuration requires heating to preserve the radicals to improve the effectiveness of NRP discharges for flame enhancement.

In addition to experimental studies, much effort has focused on developing predictive models of PAI and PAC. The reduced electric field strength (E/N) is a critical parameter for simulating nanosecond pulsed plasmas because it determines the production rates of electrons and high-energy states of molecules [159]. However, accurately measuring the electric field with sufficient resolution is challenging and has only been accomplished recently, [160], [161] so other approaches for estimating the electric field are typically used. Several studies [79], [162], [163] have modeled a nanosecond pulsed plasma in zero-dimension (0D) with estimated E/N calculated from the measured discharge current assuming a uniform plasma after breakdown. These studies showed that it is appropriate to use a two-term Boltzmann equation solver to calculate the plasma properties for NRP discharges. In addition, Bak and Cappelli [98] incorporated diffusion and convection losses into their 0D plasma model, which are significant for pin-to-pin NRP discharges. Several authors have combined such 0D models of plasma kinetics with traditional combustion chemistry to simulate plasma-assisted fuel oxidation and ignition [100], [164].

While many researchers have studied PAI chemistry using 0D simulations, numerical investigations of flames coupled with NRP discharges in even one dimension are very scarce. Besides the aforementioned simulation [91], Casey *et al.* [165] performed a one-dimensional simulation of the application of a nanosecond pulse to an ignited flame kernel. Unsurprisingly, these one-dimensional (1D) models [156], [165] were very computationally expensive compared to a 0D model. Shioyoke *et al.* [166] simulated the effect of a nanosecond plasma on the burning velocity of an ammonia flame in the second configuration discussed above (plasma applied upstream of the flame). They separated the plasma and combustion into two computational domains: a 0D perfectly stirred reactor (PSR) containing the plasma discharge upstream and a 1D steady laminar flame downstream, respectively. They applied a constant reduced electric field to the PSR to generate a time-dependent species profile, and then chose a slice of the profile at a specified degree of ammonia decomposition as the inlet condition for the 1D steady flow. While the model proposed by Shioyoke and co-workers can be used to investigate the effect of non-equilibrium plasma on the burning velocity at different degrees of fuel decomposition, the model does not consider the transient effect of the time-dependent species profile. In this study, we propose to combine a customized PSR model for NRP plasma discharges and a 1D *unsteady* flame model to analyze the effects of NRP plasma on both flame ignition and propagation. We focus on the spark regime and its thermal and chemical effects. We choose to model a counterflow diffusion flame because previous experimental studies [157], [167] used the counterflow configuration to show the effect of non-equilibrium plasma and the associated radicals produced by the plasma on the flame.

3.3 Plasma-Assisted Flame Model

3.3.1 Model Overview

A schematic of the plasma-assisted counterflow burner model is shown in Figure 3.1. In this configuration, the plasma is generated only in the oxidizer stream; therefore, we can treat the plasma and flame in two separate domains: a 0D plasma reactor and a 1D counterflow flame, which are solved separately. We assume the mass flow rate of the oxidizer

at the left boundary is constant, which can easily be achieved in an experiment using a flow rate controller. We set the left boundary inlet condition (convection boundary condition) to be the output of the 0D plasma reactor, which is assumed to have the same properties (gas composition and temperature) of the plasma except for charged species (see Section 3.3.5). The inlet velocities of the plasma discharge and burner are $u_{\text{in,plasma}}$ and $u_{\text{in,burner}}$, respectively. Such a decoupled model is significantly more computationally efficient due to the vastly different timescales associated with the plasma kinetics versus the combustion chemistry [168]. In addition, it can be more efficient to apply the plasma discharge upstream of the flame so that the discharge input energy is not wasted on the burned gas. Finally, using two separate domains for the plasma and combustion calculations facilitates model parameter manipulation. For example, the 1D flame may be removed and replaced with a multi-dimensional computational fluid dynamics (CFD) simulation connected to the 0D plasma reactor.

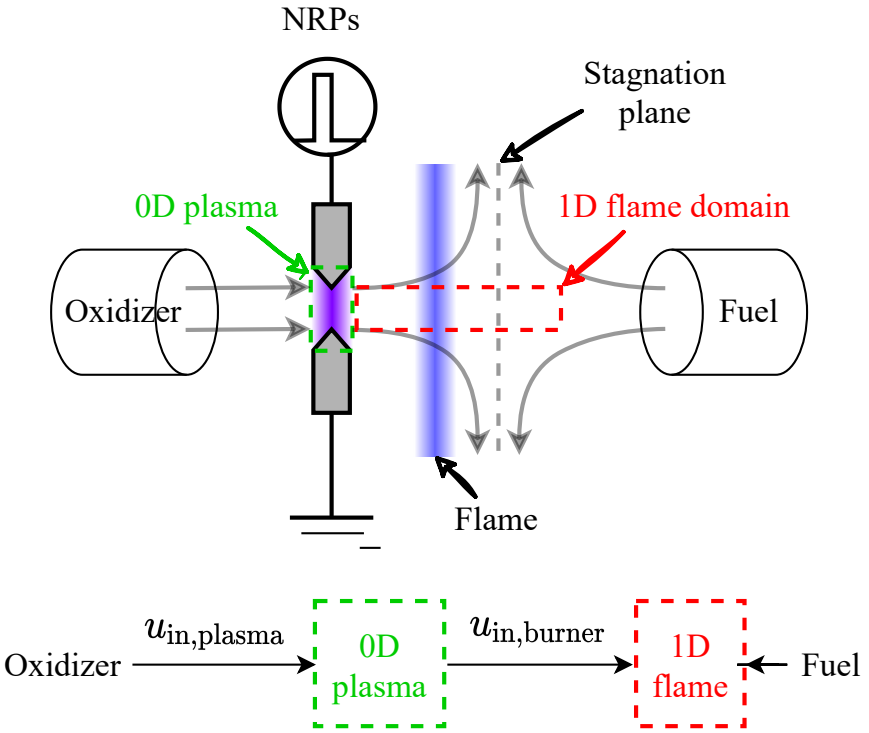

Figure 3.1. Schematic of NRPs plasma assisted counterflow diffusion flame

3.3.2 Zero-dimensional plasma reactor model

Our plasma reactor model is based on the model of Adamovich *et al.* [169], which is used to simulate the nanosecond pulsed plasma between two spherical electrodes with air initially at 300 K and 100 Torr [170]; the results matched well with the experimental data of [170]. Our plasma model uses a more general electrical relationship (see section 3.3.3) of current and electric field from [79], [94], [162], [163] instead of the cathode drop model in [169]. In addition, our 0D plasma reactor was developed based on the model of a perfectly-stirred reactor (PSR) to simulate the effect of the flow rate into the plasma reactor. Section B.2.1 provides a detailed comparison.

The governing equations include the species conservation equations, the energy equation for the gas (rotational/translational) temperature, the equation for vibrational level populations, and the equation of state. Note that the advantage of using the population fraction approach for vibrationally excited N_2 is that it does not require adding more reactions to the mechanism for each vibrational state. The conservation equation for species k is given by

$$\frac{dY_k}{dt} = \frac{1}{\tau_{res}}(Y_{k,in} - Y_k) + \frac{\dot{\omega}_k W_k}{\rho} + \left(\frac{dY_k}{dt}\right)_{diff}, \tag{3.1}$$

where Y_k is the mass fraction, $\dot{\omega}_k$ is the net production rate, and W_k is the molar mass of species k in the PSR. The subscript "in" denotes the inlet gas to the PSR. The residence time τ_{res} is equal to the total system mass divided by the mass flow rate through the control volume ($M/\dot{M}$). ρ is the gas density in PSR and $\left(\frac{dY_k}{dt}\right)_{diff}$ is the species diffusion term. In the current study, we assume that the total mass in the discharge is held constant, and we can estimate τ_{res} by dividing the discharge diameter by the inlet flow velocity, $u_{\text{in, plasma}}$. We use Cantera [107], an open-source program, to calculate the source term for the net production rate of species $\dot{\omega}_k$, which includes both plasma and combustion reactions. The species diffusion term can be derived approximately using the finite-volume method as

$$\left(\frac{dY_k}{dt}\right)_{diff} \approx \frac{1}{\rho}\left(\frac{D_{k,0} + D_k}{2}\right)\left(\frac{\rho_0 + \rho}{2}\right)\left(\frac{Y_{k,0} - Y_k}{R_d^2}\right) \tag{3.2}$$

where R_d is the radius of discharge, D_k is the diffusion coefficient of species k of the PSR. The subscript "zero" denotes the ambient gas (the co-flow of discharge). The diffusion coefficients are calculated by Cantera [107] with the mixture-average method $D_k = D_{k,mix}$. For charged species, the diffusion coefficients are calculated by ambipolar diffusion, given by

$$D_k = D_{\mathrm{O_2^+}}(1 + T_\mathrm{e}/T), \tag{3.3}$$

where $D_{\mathrm{O_2^+}}$ is the diffusion coefficient of $\mathrm{O_2^+}$, which is the most abundant positive charged species during the pulse and is calculated using the *Stockmayer-[n, 6, 4]* potential [127] to account for ambipolar diffusion. T_e is the electron temperature, which can be calculated from the electron Boltzmann equation (see section 3.3.3). T is the gas temperature. The energy equation is given by,

$$\begin{aligned}\frac{dT}{dt} = \frac{1}{\tau_{res} c_p}\sum_k Y_{k,in}(h_{k,\mathrm{in}} - h_{k,\mathrm{eq}}) + \frac{1}{\rho c_p}\sum_k h_{k,\mathrm{eq}}\dot{\omega}_k W_k + \\ \left(\frac{dT}{dt}\right)_{comp.} + \left(\frac{dT}{dt}\right)_{\mathrm{cond.}} + \left(\frac{dT}{dt}\right)_{\mathrm{diff.}} + \left(\frac{dT}{dt}\right)_{\mathrm{vib.}},\end{aligned} \tag{3.4}$$

where c_p is the molar heat capacity and $h_{k,\mathrm{in}}$ is the enthalpy (by mass) of the inlet gas. $h_{k,\mathrm{eq}}$ is the enthalpy in the PSR at equilibrium ($T_\mathrm{e} = T_{gas}$), which is calculated by Cantera (see details in Section 3.3.4). The terms $(dT/dt)_{\mathrm{comp.}}$, $(dT/dt)_{\mathrm{cond.}}$, $(dT/dt)_{\mathrm{diff.}}$, and $(dT/dt)_{\mathrm{vib.}}$ are the temperature changes due to compensation, conduction, diffusion, and vibration. The compensation term adds back the absorbed energy of non-elastic electron collisions including excitation, ionization, and dissociation reactions, which we may write as

$$\left(\frac{dT}{dt}\right)_{comp} = \frac{1}{\rho c_p}\sum_\mathrm{i} \Delta h_\mathrm{i} R_\mathrm{i}, \tag{3.5}$$

where Δh_i is the enthalpy difference between the ground and excited states of a molecule, which is also the threshold energy of the inelastic electron collision process of the plasma reaction i. The rate of progress of reaction i is expressed as

$$R_\mathrm{i} = k_\mathrm{i}[\mathrm{e}][X], \tag{3.6}$$

where k_{i} is the rate coefficient of reaction i for the inelastic collision processes [e] is the concentration of electron, and $[X]$ is the concentration of the target species of electron collision. Note that an elastic collision transfers a much smaller amount of energy compared to an inelastic collision due to the large mass difference between electrons and molecules, and their elastic collisions with electrons are neglected in this study. To illustrate the need for such a compensation term, consider the example of the excitation of ground state nitrogen molecules to the nitrogen triplet state by collision with high temperature electrons,

$$\mathrm{N_2 + e \longrightarrow N_2(A^3) + e.} \tag{3.7}$$

The energy of $\mathrm{N_2(A^3)}$ is higher than $\mathrm{N_2}$, and the energy of the electron on the right hand side (post-collision) is lower than on the left hand side (pre-collision). However, Cantera regards the electron energy as a function of gas temperature only and treats this collision process as an endothermic reaction. In reality, the excitation energy comes from the electron instead of the gas for an electron-collision process. Therefore, the excess energy of the electron is added to the left side of the reaction,

$$\mathrm{N_2 + e + \epsilon_e \longrightarrow N_2(A^3) + e,} \tag{3.8}$$

where

$$\epsilon_{\mathrm{e}} = h_{\mathrm{N_2(A_3)}} - h_{\mathrm{N_2}}. \tag{3.9}$$

Analogous to mass diffusion, the heat transfer from the plasma discharge through conduction may be derived as

$$\left(\frac{dT}{dt}\right)_{\mathrm{cond.}} \approx \frac{1}{\rho c_p}\left(\frac{\lambda_0 + \lambda}{2}\right)\left(\frac{T_0 - T}{R_d^2}\right), \tag{3.10}$$

where T_0 is the ambient gas temperature and λ is the thermal conductivity. In addition, the temperature change due to the mass diffusion is given by

$$\left(\frac{dT}{dt}\right)_{\mathrm{diff}} \approx \frac{1}{\rho c_p}\sum_k h_k^*\left(\frac{dY_k}{dt}\right)_{\mathrm{diff.}} \tag{3.11}$$

where h_k^* (enthalpy) depends on the direction of mass diffusion, i.e. the sign of the concentration gradient, as

$$\begin{aligned} h_k^* &= h_{0,k} \text{ for } \left(\frac{dY_k}{dt}\right)_{\text{diff.}} > 0 \\ h_k^* &= h_k \text{ for } \left(\frac{dY_k}{dt}\right)_{\text{diff.}} < 0. \end{aligned} \tag{3.12}$$

Note that we neglect the effect of mass diffusion of vibrational states in the energy equation because the exchange of vibrational quanta between different molecules occurs on much shorter timescales than diffusion. The mass diffusion of vibrational states does have an effect on the population fraction of the vibrational states but it does not create heat flux (translational energy flux) through the boundary. To simplify the reaction mechanism, the current model uses the equation of vibrational level populations fraction equation and the implementation described below for the vibrational states of nitrogen,

$$\frac{df_v}{dt} = \frac{\dot{\omega}_v}{[\mathrm{N_2}]} + \frac{1}{\rho}\left(\frac{\rho_0 + \rho}{2}\right)\left(\frac{D_{\mathrm{N_2},0} + D_{\mathrm{N_2}}}{2}\right)\left(\frac{f_{v,0} - f_v}{R_d^2}\right) \tag{3.13}$$

where f_v is the population fractions of nitrogen at the vibrational level v for the discharge. We use the diffusion coefficient of the ground state nitrogen for all vibrational states by assuming the cross sections of the vibrational states are the same as the ground state and, according to the Chapman-Enskog theory [171], the diffusion coefficients are the same if the temperature (translational) is the same. We assume that the diffusion coefficient $D_{\mathrm{N_2}}$ is the same as the ground state of nitrogen. We also define $[\mathrm{N_2}]$ as the total concentration of $\mathrm{N_2}$ (summation of ground and all vibrational states), which is calculated from Eq. (3.1) and used for all reactions involving $\mathrm{N_2}$. For example, the excitation reaction $\mathrm{N_2 + e \longrightarrow N_2(A^3) + e}$ uses the total concentration of nitrogen assuming the reaction rate coefficient is the same for different vibrational states. The third body efficiencies of nitrogen vibrational states are also assumed to be the same as ground state nitrogen. Note that the reaction rates involving the vibrational states of nitrogen can differ from the ground state, especially for a strongly endothermic reactions. Due to the lack of experimental measurements, the

reaction rates are usually calculated by models such as the Fridman-Macheret model [172]. The vibrational heating term is given by

$$\left(\frac{dT}{dt}\right)_{vib.} = \frac{1}{\rho c_p}\sum_v h_{\mathrm{N}_2(v)}\dot{\omega}_{\mathrm{N}_2(v)}W_{\mathrm{N}_2} \tag{3.14}$$

where h_v is the enthalpy of the nitrogen vibrational state v ($h_v = h_{\mathrm{N}_2} + \epsilon_v$). Finally, the equation of state is [169],

$$P(t) = P_0 + \rho_0 R[T(t) - T_0]\exp\left[-\left(\frac{t}{\tau_{acoust}}\right)^2\right] \tag{3.15}$$

where $\tau_{acoust} \approx R_d/a$ is the acoustic timescale. Note that Eq. 3.15 captures the fast heating effect of NRP on pressure change. The pressure only changes significantly in the first 10 μs after the pulse, and the temperature change due to pressure for constant volume, ($\rho c_p \Delta T = -\Delta P$), is not significant in the simulation. We solve the 0D equations using Scipy [173] with the backward differentiation formula (BDF) method. Gas properties, including diffusion coefficients, heat capacity, conductivity, and enthalpy, are calculated by Cantera [107].

3.3.3 Electron Properties

The 0D plasma reactor model is coupled with BOLOS [108], an open source electron Boltzmann equation solver using the two-term approximation method with the temporal growth model [134], to evaluate electron properties including electron temperature, plasma reaction rates, and electron mobility (drift velocity). Cross-section data for N_2 and O_2 are obtained from [174]. All properties are pre-calculated for reduced electric fields from 0 to 1000 Td with a 1 Td increment at T=300 K, and thus properties for a given value of E/N (electric field over gas number density) can be easily obtained by linear interpolation during a simulation. Note that the gas temperature only affects the elastic collision and has negligible effect on EEDF (electron energy distribution function as a function of E/N) when temperature is low. We do not consider the change of gas composition in solving BOLOS as this requires a multi-variable table for interpolation of electron properties. We use the same

method used in [79], [94], [162], [163] to calculate the drift velocity assuming the discharge is uniform,

$$E\mu_{\mathrm{e}} = \frac{I}{\mathrm{e}n_{\mathrm{e}}S}, \tag{3.16}$$

where I is the current, n_{e} is the electron number density, S is the cross-sectional area of the discharge, and μ_{e} is the electron mobility, which is a function of the reduced electric field. Since the drift velocity $E\mu_{\mathrm{e}}$ is a monotonic function of E/N (from the pre-calculated table), we can also express E/N as a function of the drift velocity using linear interpolation. Figure 3.2 illustrates the solution procedure for one time step in the 0D NRP plasma simulation. The drift velocity is first obtained using the electron number density from the previous time step (I and S are given from the experiment). The corresponding value of E/N is then obtained from the pre-calculated table. The maximum value of the electric field is calculated from the voltage ($E \approx V/d$) to prevent an erroneously large value of E/N, which usually occurs at the beginning of the pulse when the electron concentration is extremely low.

3.3.4 Chemistry

The plasma reactions used in the current work are listed in Table A.2. The reaction mechanism is based on the work of Adamovich *et al.* [169], which includes a detailed air/CH_4/H_2 plasma reaction mechanism for neutral molecules. Accurately predicting the electron number density is critical for accurately predicting the excited states of molecules in a plasma. Electronically excited species such as $N_2(A^3)$ especially play a dominant role in producing an oxygen atom, which can directly enhance combustion and release heat on time scales much less than a microsecond. The reaction mechanism suggested by Popov [162] predicts electron number densities that are in good agreement with experimental results for low-pressure nanosecond pulsed plasmas. We supplement this mechanism with additional reactions from [98] to complete the ion chemistry of atmospheric spark plasmas. Vibrationally excited molecular states play an important role in gas heating on longer timescales on the order of microseconds or milliseconds. Higher gas temperature promotes chain reactions and can preserve the reactivity of the plasma. For example, Takita *et al.* [158] showed that the adding radicals only significantly increases burning velocity for high temperature (> 750 K).

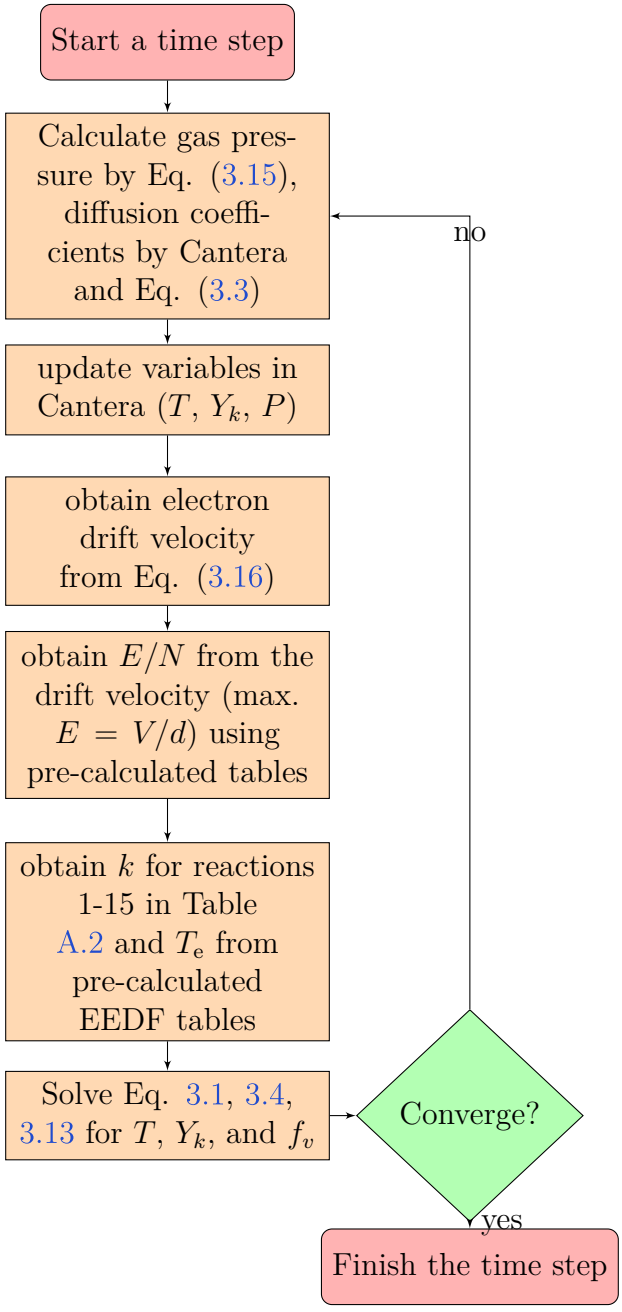

Figure 3.2. Flow-chart diagram of the zero-dimensional NRP-plasma simulation.

In this study, the cross sections for vibrational excitation of higher vibrational states are approximated by the ground state cross section (Reaction 15 in table A.2). For example, the cross section for the $v = 1$ to $v = 2$ excitation reaction of nitrogen, $N_2(v = 1) + e \longrightarrow N_2(v = 2) + e$, differs from the cross section of the ground state reaction 5% $N_2 + e \longrightarrow N_2(v = 1) + e$ by only 5% [175]. The difference in cross section is larger for higher vibrational states, but the population fraction of these higher states is also much smaller. After vibrationally excited molecules are generated from electron collision reactions, the time evolution of their populations are controlled by two primary processes: vibrational-translation (V-T) relaxation and vibrational-vibrational (V-V) transfer. According to [176], the dominant nitrogen V-T relaxation reaction is through collision with oxygen atoms, $N_2(v) + O \rightarrow N_2(v-1) + O$, and the rate coefficient can be calculated by

$$k_{v \rightarrow v-1} = v k_{1 \rightarrow 0} \exp(\delta_{VT}(v-1)), \tag{3.17}$$

where

$$\delta_{VT} = \frac{2.87}{T^{1/3}}, \tag{3.18}$$

and

$$k_{1 \rightarrow 0} = \frac{k_b T}{P\tau}, \tag{3.19}$$

where $P\tau$ is the pressure multiplied by the characteristic reaction time, T is in Kelvin. We use an empirical fit $P\tau[\text{atm s}] = \exp(32.2T^{-1/3} - 16.35)$ for $P\tau$ from [177]. Note that T is in Kelvin for Eqs. (3.17,3.18,3.19). The populations of vibrationally excited nitrogen are also affected by V-V transfer reactions, given by

$$N_2(v) + N_2(w) \longrightarrow N_2(v-1) + N_2(w-1), \tag{3.20}$$

with rate coefficients given by [176]

$$k^{v \rightarrow v-1}_{w-1 \rightarrow w} = wv k^{1 \rightarrow 0}_{0 \rightarrow 1} \exp(\delta_{VV}|w - v|)\,(3/2 - \exp(\delta_{VV}|w - v|)/2)\,, \tag{3.21}$$

where v and w are the vibrational quantum numbers of the two states participating in the reaction. The anharmonic energy between vibrational levels v and $v-1$ can be calculated by

$$\Delta E_{v,v-1} = \omega_e(1 - 2x_e v), \tag{3.22}$$

where ω_e is the harmonic energy gap between the vibrational levels and x_e is the first anharmonic term. Therefore, the energy difference of V-V transfer is

$$\Delta E = \omega_e(1 - 2x_e v) - \omega_e(1 - 2x_e w). \tag{3.23}$$

The up-pumping of vibrational levels ($w > v$) can occur without needing to overcome the energy barrier, but this is not the case for the reverse reaction. Therefore, the reverse rate is given by

$$k_r = k_f \exp(-\frac{\Delta E}{k_b T}). \tag{3.24}$$

Also, since the concentrations of the electronically excited nitrogen states such as $N_2(A^3)$ are much lower than the ground state N_2 concentration, the vibrational states of electronically excited N_2 (e.g. $N_2(A^3, v > 0)$) are neglected.

The thermodynamic properties of each species are calculated in Cantera [107] using the NASA 7-coefficient polynomial parameterization [178]. The enthalpy is expressed as,

$$\frac{H^0(T)}{RT} = -a_0 T^{-2} + a_1 \frac{\ln T}{T} + a_2 + \frac{a_3}{2}T + \frac{a_4}{2}T^2 + \frac{a_5}{4}T^3 + \frac{a_6}{5}T^4 + \frac{a_7}{T}. \tag{3.25}$$

Most of the thermodynamic data of excited species (including vibrational states of nitrogen) are from [179], [180]. When the thermodynamic data of a species is not available, we use the same approach as [179]: Use the same coefficients, a_0 to a_6, as the ground-state species, and add the threshold energy (in temperature [K]) or the energy difference between the vibrational and ground state for a_7.

3.3.5 One-Dimensional Counterflow Flame Model

We use Ember [102], an open-source transient flame solver, to simulate transient 1D counterflow flames and investigate the effect of NRPs plasma on the dynamics of such flames. Details on the governing equations employed for unsteady 1D flames can be found in the Ember documentation of [102]. We modified the source code of Ember to enable a time-dependent inlet boundary condition at the left boundary of the 1D domain. During each time step, the gas temperature and composition are updated to new values according to the 0D NRP plasma discharge (see the details in the repository https://github.com/BangShiuh/ember/tree/burner-flame-mass-flux). The reaction mechanism used for the 1D flame simulation is the San Diego Mechanism [109] supplemented by the neutral part of the air-plasma reaction mechanism used in the 0D plasma reactor model. We do not include charged species in the reaction mechanism because Ember does not solve Poisson's equation to obtain accurate transport velocities of charged species. Fortunately, the densities of charged species after a pulse are much lower and contribute very little energy to the flame when it is far away from the plasma with very low electric field. For example, the temperature increases less than 1 K for 10 ppm of electron and O_2^+ to recombine in air at 300K and 1 atm. In addition, we include only the first four vibrational states of nitrogen, which are the main states populated through electron impact during the plasma discharge [169], to account for the heating effect of relaxation of vibrational energy.

In plasma-assisted flames, both the initial concentration of radical and active species produced by the plasma and the time required for them to reach the flame are important factors to determine the degree to which these active species influence the flame chemistry. Ember [102] uses the potential flow of infinitely separated jets to derive the governing equations and defines the ESR as the maximum strain rate parameter a, which has a flame solution. The ESR (maximum a) is independent of the burner separation distance (BSD) for a typical counter-flow flame simulation (constant temperature and oxidizer/fuel composition) [102], [181]. The local axial velocity of the potential flow of infinitely separated jets without a flame is given by ([102])

$$u(x) = u_{\text{in,burner}} - \frac{a^2}{4u_{\text{in,burner}}}x^2 \tag{3.26}$$

where $u(x)$ is the axial velocity of a counterflow and $u_{\text{in,burner}}$ is the inlet velocity at the left boundary, and is equal to the flow velocity of oxidizer stream in the current study. The stagnation plane is located at $L_{u=0} = 2u_{\text{in,burner}}/a$, and the left boundary for the inlet oxidizer is at $x = 0$. We can find the characteristic time, τ_{stag} for a particle to reach the vicinity of stagnation plane the stagnation plane by

$$\int_0^{\tau_{stag}} dt = \int_0^{0.99L} \frac{dx}{u} \tag{3.27}$$

The location $x = 0.99L$ is used because, mathematically, it would take the particle an infinite amount of time to reach $x = L_{u=0}$. Solving for τ_{stag} gives

$$\tau_{stag} = \int_0^{0.99v_{\text{i}}/a} \frac{dx}{u_0 - \frac{a^2}{4u_0}x^2} \approx 5.3/a, \tag{3.28}$$

which only depends on the strain rate. Therefore, changing the inlet velocity should not have a significant effect on the time of radicals to reach the flame.

3.4 Results and Discussion

In this section, we first investigate the characteristics of the NRP plasma discharge, and the effect of PRF and flow velocity to the gas temperature and radical concentration. Then we apply these NRP plasma discharges in the oxidizer stream of a counter-flow diffusion flame and investigate the effect of NRP plasma discharges at different pulse repetitive frequencies (PRFs), flow velocities, and number of pulses on the flame ignition and extinction.

3.4.1 NRP Plasma Discharges

We chose to use the discharge parameters and initial conditions (pressure and temperature) of the experiments in [170] because our model is based on [169], which was validated to [170] as mentioned in Section 3.3.2. We first simulate the effect of a burst of multiple plasma pulses on a counter-flow diffusion flame using our 0D model of an NRP plasma discharge. A counter-flow diffusion flame in air and methane cannot be sustained in the 1D flame model at a pressure of 100 Torr. Changing the pressure in the simulation will change the reduced

electric field E/N because the gas number density N depends on the pressure. Therefore, to simulate the flame at 100 Torr, we add oxygen to the oxidizer stream to slightly increase the ratio of oxygen to nitrogen to O_2:N_2 = 1 : 2.4 (29.4% oxygen and 70.6% nitrogen) by volume so that the flame can sustain itself even without the assistance of plasma. Note that we use this gas composition at 300 K and 100 Torr in both the inlet flow to the 0D plasma reactor and the oxidizer stream of the counter-flow diffusion flame for all simulations in this study. We use the same voltage and current profile from [170] for each pulse in the burst so that the power of each pulse ($P = IV$) remains constant. We assume that the discharge radius of each pulse is the same value of 0.85 mm, which is estimated from the experiments in [170]. Note that only the first pulse requires an estimation of initial electron number density, and the rest of pulses will inherit the remaining electrons from the last pulse. We choose the initial value of electron number density so that the first pulse can successfully generate a non-equilibrium plasma without an overshoot in both the gas temperature and electron number density. We use a burst of five pulses at a 2 kHz repetition rate in the oxidizer stream with inlet flow velocity of $u_{\text{in,plasma}}$ = 1 m/s at 300 K and 100 Torr ($\tau_{res} \approx 2 \times 0.85$ mm / 1.0 m/s = 1.7 ms). Figure 3.3 shows the profiles of reduced electric field and electron number density for multiple pulses. The profiles reach a quasi-steady state very quickly after the first pulse. Pulses 2-5 use the residual electrons from the previous pulse to more easily initiate a uniform plasma. The reduced electric field (E/N) is much lower for pulses 2-5 before the peak E/N because the electron number densities are higher before the peak according to Equation 3.16.

The pulse repetition frequency (PRF) and flow velocity into the plasma reactor can both influence the plasma properties in the quasi-steady state. Figure 3.4 compares the gas temperature and mass fraction of oxygen atoms (important radical for combustion) for different PRFs and inlet flow velocities to the plasma reactor. In Figure 3.4 (a) and (c), the flow velocity is fixed at $u_{\text{in,plasma}}$ = 1 m/s (at 300 K and 100 Torr) and the PRF is varied from 500 Hz to 4 kHz. In Figure 3.4 (b) and (d) the PRF is fixed at 1 kHz and the flow velocity ($u_{\text{in,plasma}}$) into the plasma reactor is varied from 0.25 to 2 m/s. As shown in Figure 3.4 (a) and (c), increasing the PRF can significantly increase both peak gas temperature and oxygen atom mass fraction. Decreasing the flow velocity (increasing residual time) can

also increase both the peak gas temperature and peak oxygen atom mass fraction, as shown in Figure 3.4 (b) and (d), but to a more modest degree than increasing the PRF. Also, the increases in gas temperature and oxygen atom concentration quickly saturate as the flow velocity is decreased. Therefore, decreasing the flow velocity is not as effective at enhancing the plasma properties as increasing the PRF.

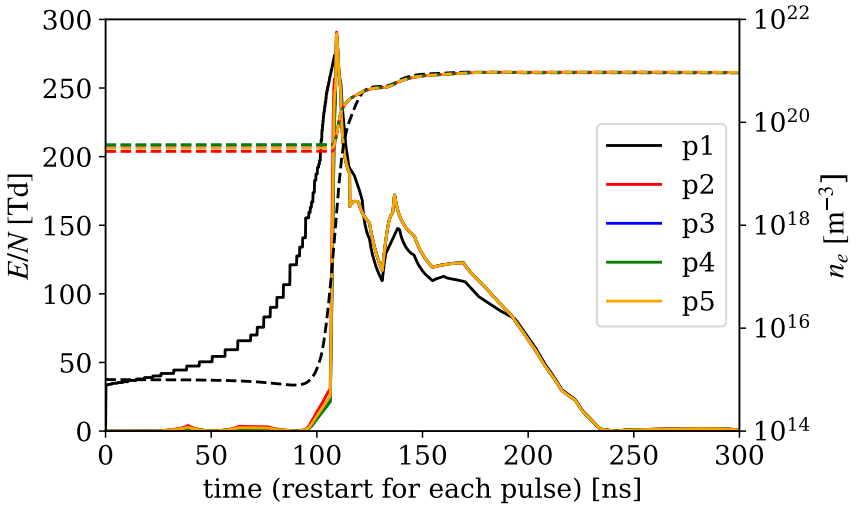

Figure 3.3. Profiles of reduced electric field and electron number density for each pulse in a burst of 5 NRP plasma discharges (PRF = 2 kHz) in the oxidizer stream (29.4% oxygen and 70.6% nitrogen, 300 K, and 100 Torr) with flow velocity, $u_{\text{in,plasma}} = 1$. The dashed lines are the electron number density.

To increase the computational efficiency by taking advantage of the separable 0D and 1D domains in our model 3.3.1, we can use a larger timescale for the 1D flame simulation than for the 0D plasma simulation (0.1 ns) due to the vastly different timescales of NRP plasma and combustion chemistry. To confirm this, we simulate the methane/oxidizer diffusion flame with applied NRP discharges (five pulses at PRF = 2 kHz) at a strain rate of $a = 400$ 1/s (see definition in [102]) using time resolutions larger than the 0D plasma simulation, i.e. > 0.1 ns. The 1D counterflow burner simulation uses the 0D simulation result as the oxidizer stream, and pure methane as the opposite stream of fuel. The flow velocity of the oxidizer stream into the flame ($u_{\text{in,burner}}$) is set to equal to the plasma flow velocity $u_{\text{in,plasma}}$ at 300 K, and 100 Torr. Note that the time steps for the 1D simulation are produced by filtering the original time steps of the 0D simulation to the desired resolution. Figure 3.5

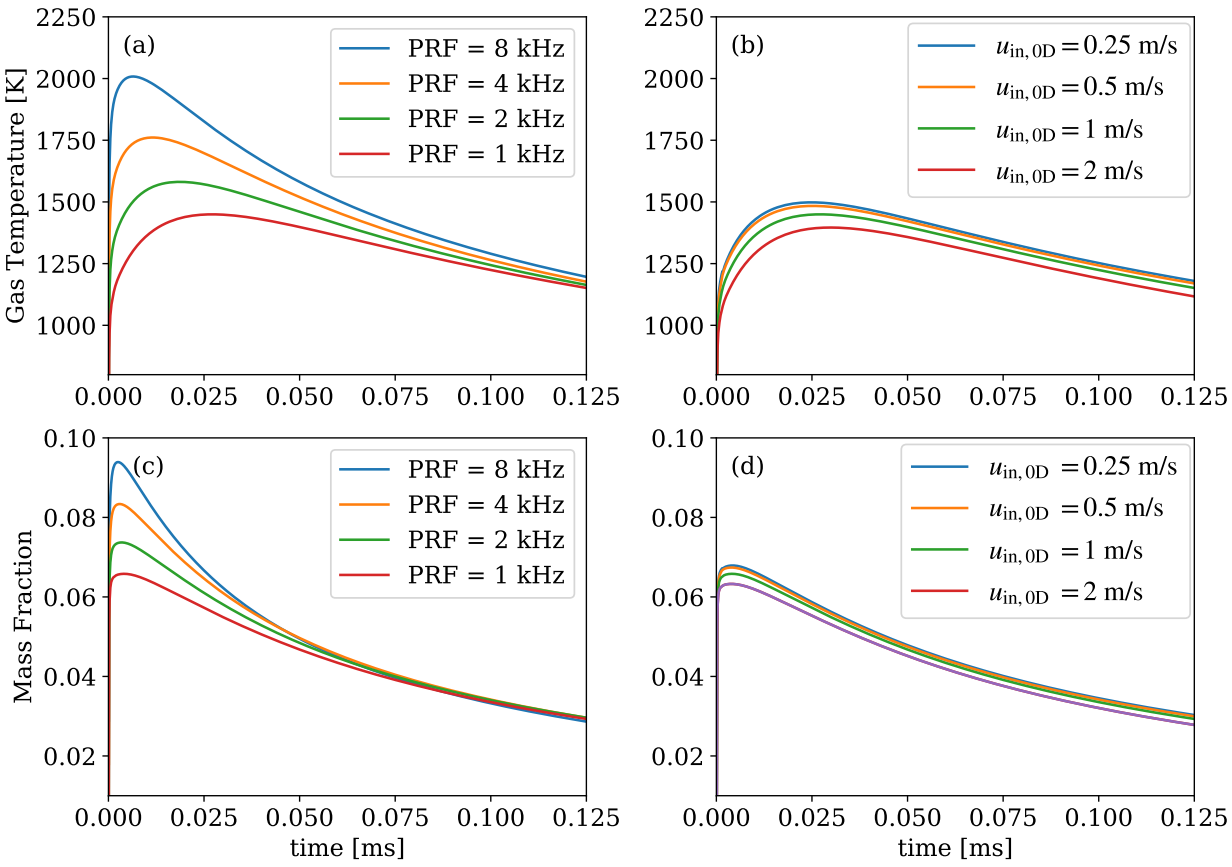

Figure 3.4. Gas temperatures and mass fractions of oxygen atoms produced by NRP discharges in the quasi-steady state for different PRFs and flow velocities into the plasma reactor (29.4% oxygen and 70.6% nitrogen, 300 K, and 100 Torr). (a) and (c) Effect of PRF on gas temperature and oxygen mass fraction with a flow velocity of $u_{\text{in,plasma}} = 1$ m/s; (b) and (d) Effect of the plasma flow rate with PRF of 1 kHz.

shows the error of the calculated flame heat release rate using larger time resolutions for the 1D flame simulation vs. the result obtained using the plasma time step (0.1 ns) for the entire simulation. The error of heat release rate is used in Ember as a criterion for whether a simulation has reached a steady state. We found that 100 ns is a sufficiently small time step for the flame simulation with error less than 5% compared to a 0.1 ns time step. This reduces the computational time to approximately 15% of the time required for the entire simulation using a time step of 0.1 ns. Therefore, the following 1D flame simulations use the filtered profiles of 100 ns instead. This also indicates that any short-lived ($<$ 100 ns) plasma species will not have a significant effect on the flame downstream.

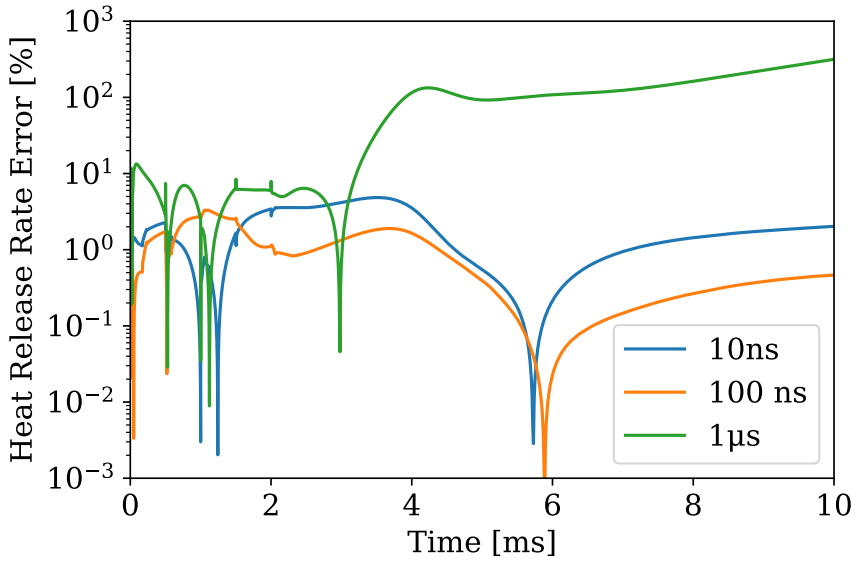

Figure 3.5. Error of the calculated flame heat release rates for different time resolutions in the 1D flame simulation, compared to the simulation with minimum 0.1 ns time step (time scale for the plasma simulation). A NRP plasma discharge (burst of 5 pulse with PRF = 2kHz and flow rate ($\rho_{\text{in,burner}} u_{\text{in,burner}}$) calculated from $u_{\text{in,burner}} = u_{\text{in,plasma}} = 1$ m/s at 300 K and 100 Torr) is applied to a self-sustained flame with strain rate $a = 400$ 1/s.

3.4.2 Effect of NRP Plasma Discharges on Flame Extinction

In this section, we investigate the effect of continuously-applied (contract to burst mode) NRP plasma discharges on the counterflow diffusion flame extinction strain rate. The con-

ventional extinction curve for a 1D counterflow flame simulation uses the spatially maximum temperature as the peak flame temperature. The maximum temperature of the NRP plasma-assisted flame changes over time because of the oscillating inlet condition produced by the NRP discharges. Therefore, we use the average maximum temperature of one period (time equals the inverse of PRF) for the curves of the NRP plasma cases; the same averaging approach is used for the fuel consumption rate). Note that we choose PRFs of 1 kHz and 2 kHz because the plasma produced at these PRFs does not increase the gas temperature above the flame temperature. The maximum local fuel consumption rate (FCR) is another important indication of the existence of a flame. We define the non-dimensional FCR as

$$\eta_{FCR} = \frac{FCR}{aC_{fuel}} \tag{3.29}$$

where C_{fuel} is the concentration of fuel (methane) at 300 K and 100 Torr. The denominator represents the flow rate of the fuel. To accommodate the flame and to prevent the flame from being too close to the boundary, larger inlet velocities, $u_{\text{in,burner}}$ are needed when the strain rate is high ($L_{u=0} = 2u_{\text{in,burner}}/a$, see Section 3.3.5). Therefore, we select a higher flow velocity, $u_{\text{in,burner}} = 4$ m/s (at 300 K and 100 Torr) to simulate the flame extinction curve for PAC cases. In experiments, it is easiest to use the same mass flow rate into both the plasma discharge and the burner inlet. Therefore, we set $\rho_{\text{in,plasma}}u_{\text{in,plasma}} = \rho_{\text{in,burner}}u_{\text{in,burner}}$. However, the flow rates can be varied between the plasma and the burner by using additional flow controllers or nozzles/diffusers.

We first investigate the effect of the PRF of the plasma discharges on flame extinction. Figure 3.6 compares the extinction curves of flames with and without NRP plasmas produced continuously in the oxidizer stream at PRFs of 1 and 2 kHz. The flame without plasma extinguishes at a strain rate of 489 1/s (no solution for maximum temperature below 1847 K). The plasma-assisted flames can sustain significantly higher strain rates compared to the flame without plasma, and the maximum temperature increases significantly. The maximum temperature and η_{FCR} decrease dramatically around $a = 1250$ 1/s and $a = 3150$ 1/s for PRF = 1 kHz and 2 kHz, respectively. In addition, the temperature beyond this drop-off remains higher than 1000 K indefinitely and η_{FCR} is not zero because the active species generated by

the plasma can still oxidize the fuel even when the temperature is too low for a self-sustained flame. Experiments by Sun *et al.* [157] showed similar trends where NRP plasma discharges extended the extinction strain rate and increased the intensity of a methane-oxygen-argon counter-flow flame. They observed an increase of the extinction strain rate from less than 300 1/s to more than 500 1/s when applying 20 kHz NRP discharges in the oxidizer stream (28% O_2 and 72%Ar mixture). They also performed simulations with different oxidizer temperatures and oxygen atom addition, using constant values instead of the periodic profiles of temperature and species concentration created by the pulsed discharges in our simulation). They showed that the extinction strain rate increases significantly as the oxidizer temperature increases, with an extinction strain rate higher than 1000 1/s at 900 K. Note that the electric field used in [157] is much lower compared to our study (Sun: max. $V \approx 6500$ V with $d = 10$ mm and current study: $max.V \approx 9000$ V with $d = 2$ mm.). Thus the plasma temperature in [157] (528 K) is much lower than the plasma temperature in our study (average temperature of 641 K and 868 K for 1 kHz and 2 kHz cases, respectively), and so we expect to observe a greater increase of the extinction limit in our simulation.

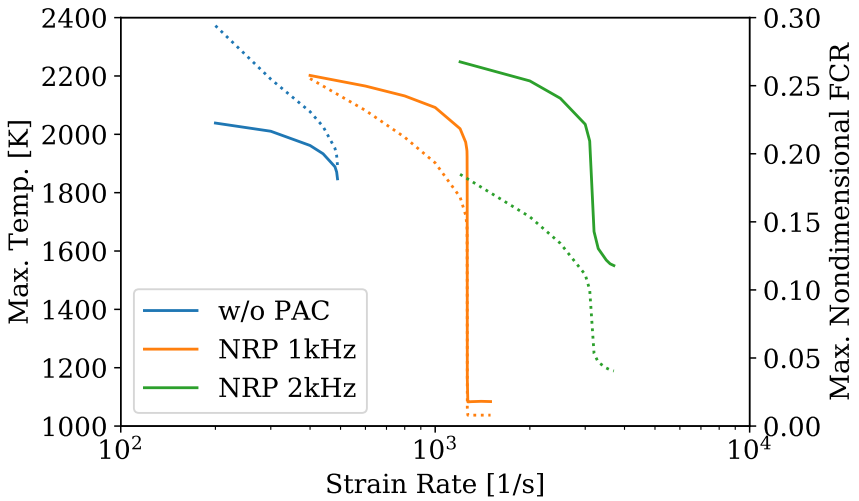

Figure 3.6. Extinction curves for counter-flow diffusion flames with and without NRP plasma discharges (PRF = 1 and 2 kHz) in the oxidizer stream (opposite fuel stream of pure methane). The solid curves are the temperature and the dotted curves are the maximum nondimensional FCR (η_{FCR}). The flow velocity is $u_{\text{in,plasma}} = 4$ m/s at 300 K and 100 Torr, and $\rho_{\text{in,burner}} u_{\text{in,burner}} = \rho_{\text{in,plasma}} u_{\text{in,plasma}}$.

As discussed in Section 3.4.1, the flow velocity into the plasma reactor $\rho_{\text{in,plasma}} u_{\text{in,plasma}}$ is also an important factor for plasma-assisted flames as it affects the plasma properties (see Figure 3.4). Therefore, we now investigate the effect of flow velocity into the plasma on flame extinction using a fixed PRF. For the results in Figure 3.6, the inlet flow rate for the flame was equal to the inlet flow rate for the plasma reactor, i.e. $\rho_{\text{in,plasma}} u_{\text{in,plasma}} = \rho_{\text{in,burner}} u_{\text{in,burner}}$ and the plasma flow rate was fairly large (4 m/s). However, it is difficult to simulate the extinction curve for low inlet flow rates into the flame and high strain rate because the stagnation plane can be pushed too close to the boundary (see Equation 3.26). Therefore, we investigate the effect of the flow velocity into the plasma reactor $u_{\text{in,plasma}}$ independent of the flow velocity into the burner oxidizer stream $u_{\text{in,burner}}$. Note that the value of $u_{\text{in,burner}}$ has only minor effects on the flame because the time for radicals to reach the flame only depends on the strain rate a (see Section 3.3.5). Figure 3.7 shows the extinction curves for a fixed PRF of 1 kHz with plasma reactor inlet flow velocities $u_{\text{in,plasma}}$ varying from 0.25 to 4 m/s. It is shown that decreasing the flow velocity into the plasma reactor (increasing the residence time) does moderately increase the extinction strain rate. However, when compared to Figure 3.6, it is clear that increasing the flow residence time is not nearly as efficient as increasing the plasma PRF because the temperature and oxygen atom concentration saturate very quickly as the residence time increases (see Figure 3.4).

3.4.3 Flame Ignition Using NRP Plasma Discharges

Finally, we use the model to investigate ignition of a counter-flow diffusion flame using a burst of NRP plasma discharges in the oxidizer stream. Placing the NRP plasma discharge in the oxidizer stream makes it much easier to control and model the plasma because the inlet gas composition stays constant (whereas it varies near the flame) which allows us to use the EEDF table discussed in Section 3.3.3 for interpolating plasma parameters such as reaction rates. In addition, placing the discharge in the oxidizer stream prevents damage to the electrodes by the high flame temperature. To study the efficiency of flame ignition using NRP plasmas, we simulate the 1D counter-flow with inlet flow velocity of $u_{\text{in,burner}} = u_{\text{in,plasma}} = 1$ m/s at 300 K, a strain rate of $a = 400$ 1/s, and generate plasma discharges in the oxidizer

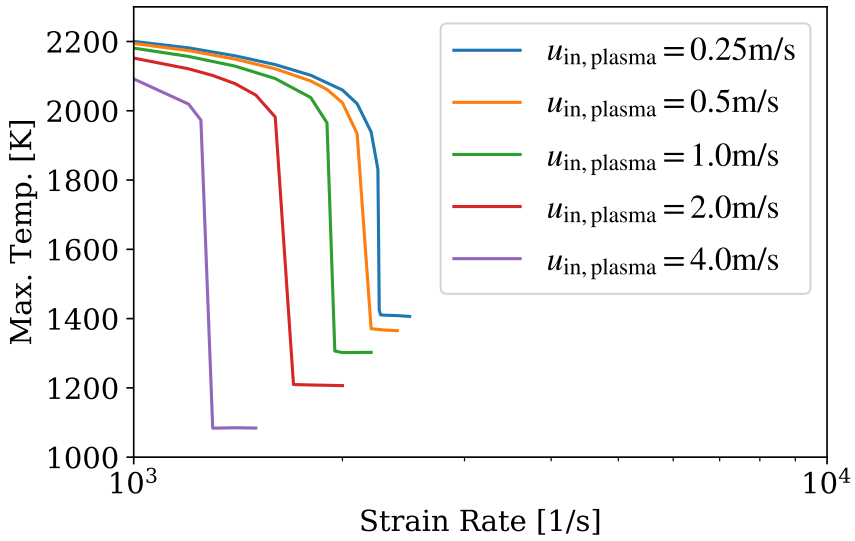

Figure 3.7. Extinction curves of counter-flow diffusion flames with NRP plasma discharges (PRF = 1 kHz) with different flow velocities into the plasma reactor ($u_{\text{in,plasma}}$). The flow rate of the burner oxidizer stream is fixed to the value calculated from $u_{\text{in,burner}}$ = 4 m/s at 300 K and 100 Torr (independent of $u_{\text{in,plasma}}$).

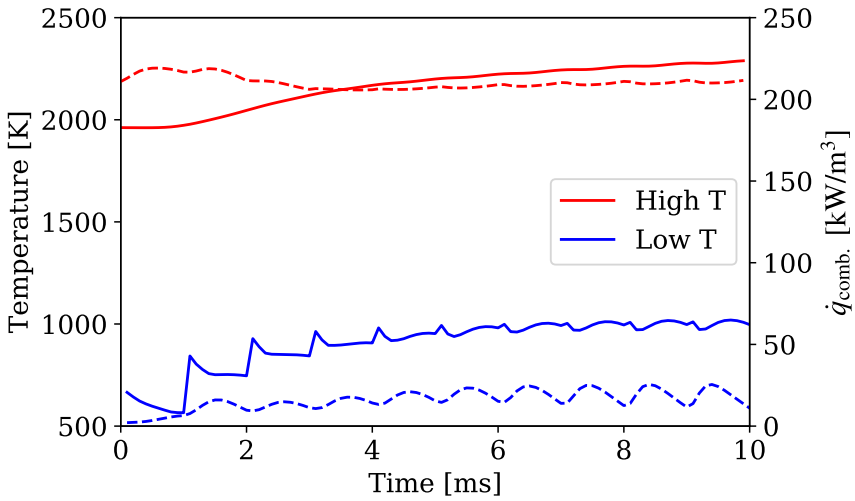

Figure 3.8. Comparing high and low temperature NRP plasma assisted counter-flow combustion (PRF = 1 kHz, flow velocity into plasma reactor $u_{\text{in,burner}}$ = 1 m/s, and a = 400 1/s). The flow rate of the burner oxidizer stream is fixed to the value calculated from $u_{\text{in,burner}}$ = 1 m/s at 300 K and 100 Torr. The dashed lines are the combustion heat release rates. The high-temperature case started the simulation with the stable flame profile, but the low-temperature case started with room temperature unburned gas. The combustion heat is calculated only with the reactions in [109].

stream. We start with the lowest PRF considered in this paper, 1 kHz. Figure 3.8 shows that the case with 1 kHz NRP discharges has two quasi-steady solution branches depending on the initial conditions of the gas in the 1D domain. The high temperature branch starts with a stable flame profile, and the NRP plasma increases the flame temperature and combustion heat release rate. The low temperature branch starts with room temperature unburned gas (300 K), and we find that discharges with a PRF of 1 kHz cannot ignite the counter-flow diffusion flame, but rather induce only low-temperature oxidation. Therefore, we next apply discharges with higher PRFs (2 kHz, 4 kHz, and 8 kHz) in the oxidizer stream to investigate ignition.

We start the simulation with a small number of pulses and gradually apply more until the flame ignites to determine the minimum number of pulses for ignition. We also simulate the same number of pulses with different PRFs to investigate the effect of PRF on ignition delay. We use the time difference from the beginning of the burst to the maximum heat release rate as the ignition delay time (IDT). The resulting ignition delays for the different cases are shown in Figure 3.9. PRFs of 2 kHZ and 4 kHz require a minimum of 9 pulses to ignite the flame, while 12 pulses are required for a PRF of 8 kHz. For PRF = 2 kHz, increasing the number of pulses only slightly shortens the IDT (5.25 ms to 5.22 ms with $>$ 9 pulses). For PRF = 4 kHz and 8 kHz, increasing the number of pulses is more effective in shortening the ignition delay, but the magnitude of the decrease of the IDT decreases exponentially as the number of pulses increases as shown in Figure 3.10. Applying pulses with PRF = 4 kHz and 8 kHz gives a shorter ignition delay time than for PRF = 2 kHz because the higher frequency pulses result in higher temperatures and concentrations of radical species (3.4). However, using a PRF of 8 kHz requires more pulses to ignite the flame (12 pulses for PRF = 8 kHz compared to 9 pulses for PRF = 4 kHz).

Figure 3.11 shows the evolution of plasma temperature and concentration of oxygen atoms (the main chain branching radical for combustion) at the centroid of the combustion heat release rate for different PRFs but the same number of pulses (9). For PRF = 2 kHz and 4 kHz, ignition is successful because the longer burst duration (4.5 and 2.25 ms for 2 and 4 kHz, respectively) maintains the higher temperature and oxygen atom concentration for a longer time. Although the 8 kHz case generates higher temperature and oxygen atom

concentration initially, the burst duration is too short (cut off before the temperature reaches 1000 K) to maintain the reactivity of the gas. Figure 3.12 compares the temperature and oxygen concentration profiles for different PRFs (same as 3.11 but the number of pulses is increased from 9 to 12). At 2 kHz, the burst duration is longer than the ignition delay time, so the last few pulses of the burst do not contribute to flame ignition. On the other hand, when the PRF is increased to 4 kHz or 8kHz, the pulse burst finishes before the onset of ignition, causing the energy of all 12 pulses to contribute to ignition and making the IDTs similar for the two PRFs. Therefore, with the same number of pulses, higher PRFs provide faster ignition, while lower PRFs are more energy efficient as long as energy pulses are applied to ignite the flame.

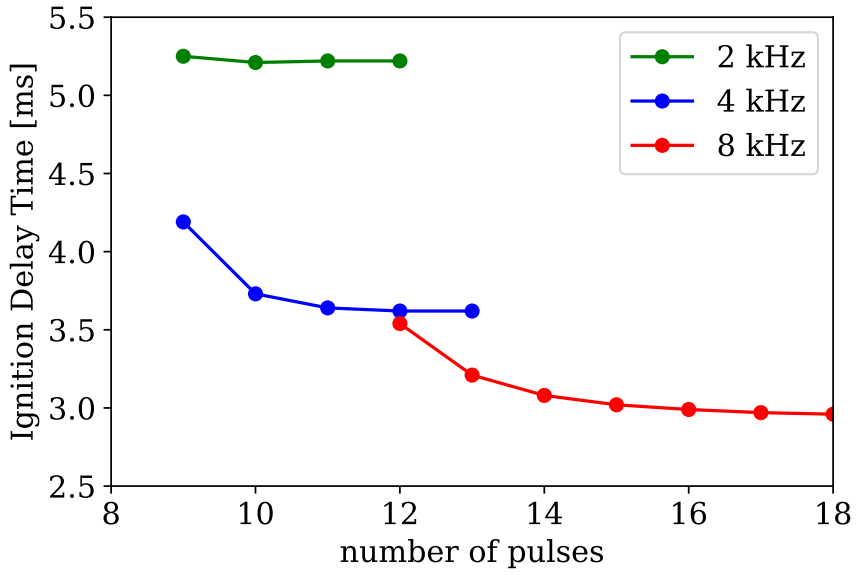

Figure 3.9. Ignition delay time (IDT) vs. number of plasma pulses for three different PRFs of the plasma discharge. The burst of plasma pulses is generated in the oxidizer stream (29.4% O_2 /70.6% N_2) with flow velocity $u_{\text{in,burner}} = u_{\text{in,plasma}} = 1$ m/s at 300K and 100 Torr.

3.5 Conclusion

This study, a NRP plasma-assisted combustion model for a methane/air counter-flow diffusion flame is developed, where the plasma discharges are generated in the oxidizer stream.

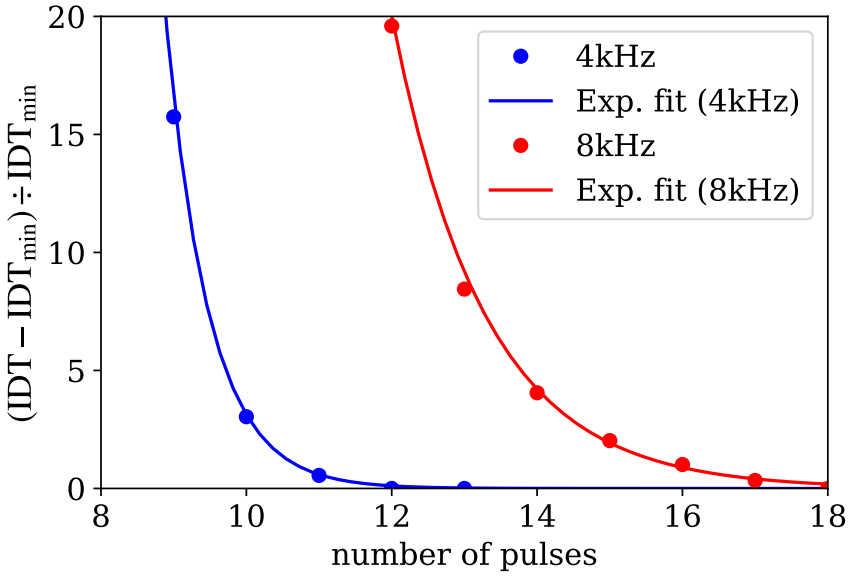

Figure 3.10. Percent difference between the IDT and overall minimum IDT as a function of number of applied pulses. The exponential decay constants are 0.78 and 1.67 for 4 kHz and 8 kHz, respectively.

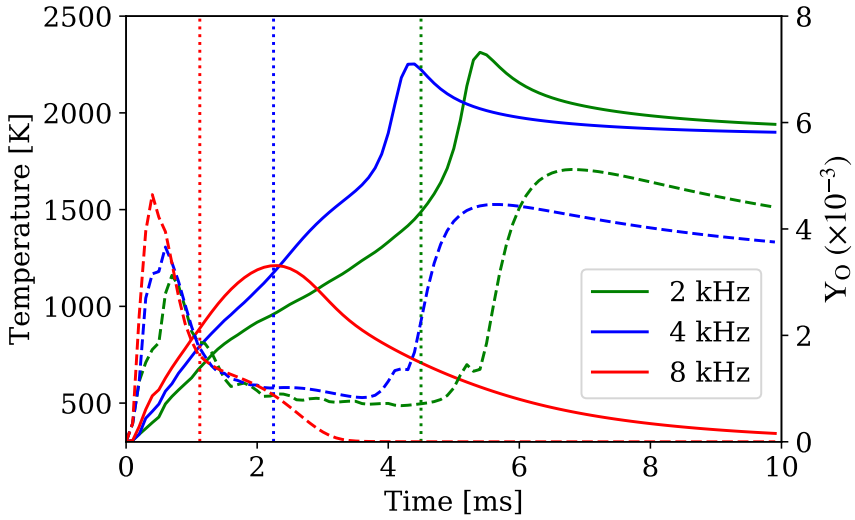

Figure 3.11. Comparison of the plasma temperature and oxygen atom concentration as a function of time at the combustion heat release centroid for a burst of 9 applied pulses at different PRFs. The combustion heat release centroid is computed from the reactions in [109] only. The temperature and oxygen concentration are given by the solid and dashed lines, respectively, and the dotted vertical lines indicate the end of the burst of 9 pulses. The inlet flow rate of the 1D counter-flow simulation is $u_{\text{in,burner}} = u_{\text{in,plasma}} = 1$ m/s at 300 K and 100 Torr. The initial mole fractions of electrons and O_2^+ ions are 3.2×10^{-10}.

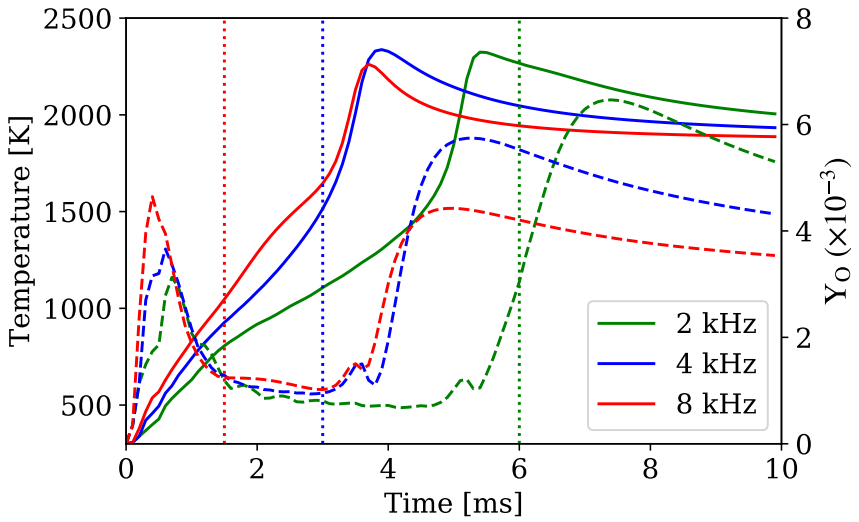

Figure 3.12. Comparison of the plasma temperature and oxygen atom concentration as a function of time at the combustion heat release centroid for a burst of 12 pulses at different PRFs. The combustion heat release centroid is computed from the reactions in [109] only. The temperature and oxygen concentration are given by the solid and dashed lines, respectively, and the dotted vertical lines indicate the end of the burst of 12 pulses. The inlet flow rate of the 1D counter-flow simulation is $u_{\text{in,burner}} = u_{\text{in,plasma}} = 1$ m/s at 300 K and 100 Torr. The initial mole fractions of electrons and O_2^+ ions are 3.2×10^{-10}.

The plasma and counterflow flame are separated into 0D and 1D domains, respectively, to increase computational efficiency of the model. The 0D NRP plasma simulation calculates the plasma properties, including reduced electric field, vibrational temperature (vibrational level populations), and species concentrations for a given current profile, voltage profile, discharge radius, and electrode gap distance. To model the 1D counterflow flame, an unsteady flame solver is modified to use the periodic gas temperature and species concentrations produced by the NRP plasma as the inlet boundary condition of the oxidizer stream.

The model is used to investigate the effect of the NRP plasma discharges on counterflow flame extinction and ignition. The results show that the extinction strain rate (ESR) can be increased significantly by applying NRP plasma discharges in the flame oxidizer stream. In addition, it is shown that increasing the plasma pulse repetition frequency (PRF) is more effective in increasing the ESR than decreasing the flow rate through the plasma discharge. using plasma discharges with higher PRFs significantly increases the peak flame temperature in the simulation. The model is also used to simulate ignition of the counterflow flame using NRP plasma discharges in the oxidizer stream. At low PRFs ($\leq\approx$ 1 kHz) the plasma produces low temperature oxidation but not flame ignition. At higher PRFs ($\geq\approx$ 2 kHz) the NRP plasmaa can ignite the counter-flow diffusion flame with a small (< 20) number of pulses. It is shown that pulse bursts with higher PRF lead to shorter ignition delay times but require more pulses to ignite the flame vs. bursts with lower PRFs.

There are some notable limitations to the model developed in this work, particularly regarding the 0D NRP plasma model. First, the model requires an estimated value for the initial electron number density before the formation of a uniform plasma and is limited to PRFs that maintain high numbers of residual electrons at the quasi-steady state. Fortunately, at high PRFs, the NRP plasma reaches a quasi-steady state very quickly after only a few repetitions. Second, the model uses an average value of reduced electric field E/N across the cathode-anode gap, which is not accurate for cases with significantly non-uniform electric fields, such as for sharp electrodes with large field enhancement at the electrode tips. Third, in reality, the rapid heating by NRP plasma discharges produces pressure waves that can induce a complex local flow field that cannot be simulated with a 0D model. This will create a larger discrepancy for both gas temperature and species concentrations at longer timescales.

The 1D flame model could also be improved by including charged species transport. However, the effect is not significant because the concentration of charged species is much lower than neutral species when the plasma discharge is far away from the flame. Despite the limitations, our PAC model can reproduce multiple-time-scale gas heating and predict flame properties in experiments. In addition, the de-coupling of plasma and flame simulation enable us to investigate the physics underlying the plasma-flame interaction efficiently. In the future, this methodology could be extended to other 1D flame models as well as 2D or even 3D PAC models.

4. CONCLUSION

4.1 Summary

This thesis reports the development of one-dimensional flame models for microwave electric field-assisted combustion and nanosecond repetitively pulsed (NRP) plasma-assisted combustion. For microwave electric field assisted combustion, we considered a free 1D flame subjected to a microwave electric field. We modified the open-source code, Cantera, to facilitate charged species electric force calculations. We also used the Boltzmann equation solver BOLOS to calculate the electron energy density function (EEDF) and incorporated the associated electron properties to accurately predict electron number density and Joule heating in the flame. For NRP plasma-assisted combustion, we built a zero-dimensional perfectly-stirred plasma reactor model to simulate the chemistry and heating produced by an NRP discharge. We used a detailed reaction mechanism composed of 270 reactions from a conventional combustion mechanism and 209 reactions describing methane/air nonequilibrium plasma chemistry. The model can simulate gas heating effects at vastly different timescales which includes the fast gas heating due to mainly dissociative quenching of N_2 and slow heatign due to vibrational relaxation. We modified the open-source unsteady flame code, Ember, to use a time-dependent gas profile and connected the zero-dimensional plasma model to a one-dimensional counter-flow diffusion flame.

Using the new model for microwave electric field-assisted combustion, we significantly improved the prediction of the flame speed enhancement by the microwaves. Our model successfully reproduced experimental results over a range of electric field strengths. The results showed that using the EEDF to calculate electron-ion recombination rates is critical for predicting the flame speed increase by a microwave electric field. We also investigated the efficiency of flame speed enhancement by microwaves via Joule heating, and we found that $E = 0.8$ kV/cm has the maximum efficiency in the range of 0.6 to 1.2 kV/cm. In addition to predicting flame speed enhancement, the model could be used to investigate other complicated effects such as expanding blow-off limits, increasing flame stability, and reducing soot formation. The major limitation of the model is that it only applies to a

sub-breakdown electric field. We can improve the model by adding more plasma chemistry to account for electric breakdown and electronically excited species.

Using our model for NRP plasma assisted-combustion, we showed that NRP plasma discharges significantly increased the flame extinction strain rate (ESR). We found that changing the pulse repetition frequency (PRF) had the strongest effect on increasing the extinction strain rate. In addition, plasma discharges at high PRF produced a shorter ignition delay time than vs. low PRF, but were not as energy efficient. The main limitation of our NRP plasma model is that it requires voltage and current profiles for the model input. However, our model is computationally efficient and capable of predicting the effect of plasma on flame properties such as flame speed, temperature, and extinction strain rate. Finally, the general approach of connecting a plasma reactor model to a flame simulation could be extended to other one-dimensional flame simulations and multi-dimensional combustion models.

4.2 Recommendations for Future Work

One closely-related future effort would be to apply our plasma-assisted combustion models to a realistic combustion system. One could replace the 1D flame with a higher dimensional CFD model or a network of 0D reactors [182]–[184] to account for the realistic flow field in an engine or a combustor. Optimization methods, such as neural networks or genetic algorithms, could then be used to optimize adjustable parameters such as PRF, pulse voltage, and flow rate, and pulse voltage to maximize engine efficiency under different constraints (e.g., amount of NO_x emission). Therefore, our models could contribute to the design process for developing cutting-edge future combustion technologie.

Another future study could entail investigating use of a pulsed microwave for PAC instead of a continuous microwave. Previous studies have suggested that using pulsed microwaves can be much more efficient [70], [74], [75] because higher electric field strength can be used without causing electrical breakdown, which can induce flame instability [75]. Modelling an unsteady flame subjected to a pulsed microwave would be challenging and computationally

expensive, but could potentially be achievable by modifying the current PAC code implemented in Ember.

Finally, the present work focused on plasma-assisted combustion in the gas phase. In reality, droplet combustion is widely used in internal combustion engines but very few studies have focused on the interactions between plasma and fuel droplets [58], [185]. Recently, an interesting study about the popular trick of using grapes in a microwave to generate plasma showed that grapes can form resonant cavities to enhance electromagnetic fields [186]. It would be interesting to investigate whether fuel droplets can induce similar behavior, and more studies could be done to better characterize these plasma/droplet interactions. Building a model to predict the electric field applied by a plasma on a single droplet would be very useful for exploring the possibility of electric field enhancement of droplet burning rates.

REFERENCES

[1] *U.S. Energy Information Administration*, https://www.eia.gov/.

[2] *Federal Highway Administration, U.S. Department of Transportation*, https://highways.dot.gov/.

[3] Y. Ju and W. Sun, "Plasma assisted combustion: Dynamics and chemistry," *Progress in Energy and Combustion Science*, vol. 48, pp. 21–83, 2015.

[4] A. Nishiyama and Y. Ikeda, "Improvement of lean limit and fuel consumption using microwave plasma ignition technology," SAE Technical Paper, Tech. Rep., 2012.

[5] C. Hampe, M. Bertsch, K. W. Beck, U. Spicher, S. Bohne, and G. Rixecker, "Influence of high frequency ignition on the combustion and emission behaviour of small two-stroke spark ignition engines," SAE Technical Paper, Tech. Rep., 2013.

[6] Z. Wang, J. Huang, Q. Wang, L. Hou, and G. Zhang, "Experimental study of microwave resonance plasma ignition of methane–air mixture in a constant volume cylinder," *Combustion and flame*, vol. 162, no. 6, pp. 2561–2568, 2015.

[7] J. Hwang, W. Kim, C. Bae, W. Choe, J. Cha, and S. Woo, "Application of a novel microwave-assisted plasma ignition system in a direct injection gasoline engine," *Applied Energy*, vol. 205, pp. 562–576, 2017.

[8] S. Padala, M. K. Le, Y. Wachi, and Y. Ikeda, "Effects of microwave enhanced plasma on diesel spray combustion," SAE Technical Paper, Tech. Rep., 2017.

[9] M. K. Le, A. Nishiyama, T. Serizawa, and Y. Ikeda, "Applications of a multi-point microwave discharge igniter in a multi-cylinder gasoline engine," *Proceedings of the Combustion Institute*, vol. 37, no. 4, pp. 5621–5628, 2019.

[10] R. Stiles, G. J. Thompson, and J. E. Smith, "Investigation of a radio frequency plasma ignitor for possible internal combustion engine use," SAE Technical Paper, Tech. Rep., 1997.

[11] A. Agneray, X. Jaffrezic, L. Mispreuve, *et al.*, "Radio frequency ignition system, breakthrough technology for the future spark ignition engine," *SAI Strassbourg*, 2009.

[12] A. Mariani and F. Foucher, "Radio frequency spark plug: An ignition system for modern internal combustion engines," *Applied energy*, vol. 122, pp. 151–161, 2014.

[13] C. D. Cathey, T. Tang, T. Shiraishi, T. Urushihara, A. Kuthi, and M. A. Gundersen, "Nanosecond plasma ignition for improved performance of an internal combustion engine," *IEEE Transactions on Plasma Science*, vol. 35, no. 6, pp. 1664–1668, 2007.

[14] T. Shiraishi, T. Urushihara, and M. Gundersen, "A trial of ignition innovation of gasoline engine by nanosecond pulsed low temperature plasma ignition," *Journal of Physics D: Applied Physics*, vol. 42, no. 13, p. 135 208, 2009.

[15] T. Shiraishi, A. Kakuho, T. Urushihara, C. Cathey, T. Tang, and M. Gundersen, "A study of volumetric ignition using high-speed plasma for improving lean combustion performance in internal combustion engines," *SAE International Journal of Engines*, vol. 1, no. 1, pp. 399–408, 2009.

[16] T. Shiraishi and T. Urushihara, "Fundamental analysis of combustion initiation characteristics of low temperature plasma ignition for internal combustion gasoline engine," SAE Technical Paper, Tech. Rep., 2011.

[17] K. Tanoue, T. Kuboyama, Y. Moriyoshi, E. Hotta, N. Shimizu, Y. Imanishi, and K. Iida, "Extension of Lean and Diluted Combustion Stability Limits by Using Repetitive Pulse Discharges," SAE International, Warrendale, PA, SAE Technical Paper 2010-01-0173, Apr. 12, 2010. DOI: 10.4271/2010-01-0173.

[18] M. Sjöberg, W. Zeng, D. Singleton, J. M. Sanders, and M. A. Gundersen, "Combined Effects of Multi-Pulse Transient Plasma Ignition and Intake Heating on Lean Limits of Well-Mixed E85 DISI Engine Operation," *SAE International Journal of Engines*, vol. 7, no. 4, pp. 1781–1801, Oct. 13, 2014, ISSN: 1946-3944. DOI: 10.4271/2014-01-2615.

[19] H. Ohisa, I. Kimura, and H. Horisawa, "Control of soot emission of a turbulent diffusion flame by dc or ac corona discharges," *Combustion and flame*, vol. 116, no. 4, pp. 653–661, 1999.

[20] D. Packan, F. Grisch, and B. Attal-Tretout, "Study of plasma-enhanced combustion using optical diagnostics," in *42nd AIAA Aerospace Sciences Meeting and Exhibit*, 2004, p. 983.

[21] M. S. Cha, S. Lee, K. Kim, and S. H. Chung, "Soot suppression by nonthermal plasma in coflow jet diffusion flames using a dielectric barrier discharge," *Combustion and flame*, vol. 141, no. 4, pp. 438–447, 2005.

[22] W. Kim, H. Do, M. G. Mungal, and M. A. Cappelli, "Plasma-discharge stabilization of jet diffusion flames," *IEEE Transactions on Plasma Science*, vol. 34, no. 6, pp. 2545–2551, 2006.

[23] W. Kim, H. Do, M. G. Mungal, and M. A. Cappelli, "Optimal discharge placement in plasma-assisted combustion of a methane jet in cross flow," *Combustion and Flame*, vol. 153, no. 4, pp. 603–615, 2008.

[24] W. Kim, H. Do, M. G. Mungal, and M. A. Cappelli, "A study of plasma-stabilized diffusion flames at elevated ambient temperatures," *IEEE Transactions on Plasma Science*, vol. 36, no. 6, pp. 2898–2904, 2008.

[25] S. Hammack, T. Lee, C. Carter, A. Lynch, and S. Kostka, "Simultaneous planar oh imaging of microwave plasma enhanced combustion at 10 khz," in *50th AIAA Aerospace Sciences Meeting including the New Horizons Forum and Aerospace Exposition*, 2012, p. 243.

[26] M. S. Bak, S.-k. Im, M. G. Mungal, and M. A. Cappelli, "Studies on the stability limit extension of premixed and jet diffusion flames of methane, ethane, and propane using nanosecond repetitive pulsed discharge plasmas," *Combustion and flame*, vol. 160, no. 11, pp. 2396–2403, 2013.

[27] S.-k. Im, M. S. Bak, M. G. Mungal, and M. A. Cappelli, "Plasma actuator control of a lifted ethane turbulent jet diffusion flame," *IEEE Transactions on Plasma Science*, vol. 41, no. 12, pp. 3293–3298, 2013.

[28] M. G. De Giorgi, A. Sciolti, S. Campilongo, E. Pescini, A. Ficarella, L. M. Martini, P. Tosi, and G. Dilecce, "Plasma assisted flame stabilizationin a non-premixed lean burner," *Energy Procedia*, vol. 82, pp. 410–416, 2015.

[29] Y.-H. Liao and X.-H. Zhao, "Plasma-assisted stabilization of lifted non-premixed jet flames," *Energy & Fuels*, vol. 32, no. 3, pp. 3967–3974, 2018.

[30] J. E. Retter and G. S. Elliott, "Investigations on a dbd burner: Corrected filtered rayleigh scattering by means of spontaneous raman scattering," in *2018 AIAA Aerospace Sciences Meeting*, 2018, p. 0933.

[31] J. Gao, C. Kong, J. Zhu, A. Ehn, T. Hurtig, Y. Tang, S. Chen, M. Aldén, and Z. Li, "Visualization of instantaneous structure and dynamics of large-scale turbulent flames stabilized by a gliding arc discharge," *Proceedings of the Combustion Institute*, vol. 37, no. 4, pp. 5629–5636, 2019.

[32] G. Pilla, D. Galley, D. A. Lacoste, F. Lacas, D. Veynante, and C. O. Laux, "Stabilization of a turbulent premixed flame using a nanosecond repetitively pulsed plasma," *IEEE Transactions on Plasma Science*, vol. 34, no. 6, pp. 2471–2477, 2006.

[33] D. Xu, D. Lacoste, and C. Laux, "Temporal and spatial evolution of oh concentration in a lean premixed propane-air flame assisted by nanosecond repetitively pulsed discharges," in *51st AIAA Aerospace Sciences Meeting including the New Horizons Forum and Aerospace Exposition*, 2013, p. 895.

[34] D. Lacoste, D. Xu, J. Moeck, and C. Laux, "Dynamic response of a weakly turbulent lean-premixed flame to nanosecond repetitively pulsed discharges," *Proceedings of the Combustion Institute*, vol. 34, no. 2, pp. 3259–3266, 2013.

[35] S. Barbosa, G. Pilla, D. Lacoste, P. Scouflaire, S. Ducruix, C. Laux, and D. Veynante, "Influence of a repetitively pulsed plasma on the flame stability domain of a lab-scale gas turbine combustor," in *Fourth European Combustion Meeting*, 2009, pp. 1–6.

[36] S. Schimek, J. P. Moeck, and C. O. Paschereit, "An experimental investigation of the nonlinear response of an atmospheric swirl-stabilized premixed flame," *Journal of Engineering for Gas Turbines and Power*, vol. 133, no. 10, 2011.

[37] C.-C. Wang and S. Roy, "Combustion stabilization using serpentine plasma actuators," *Applied Physics Letters*, vol. 99, no. 4, p. 041 502, 2011.

[38] D. Lacoste, J. Moeck, D. Durox, C. Laux, and T. Schuller, "Effect of nanosecond repetitively pulsed discharges on the dynamics of a swirl-stabilized lean premixed flame," *Journal of Engineering for Gas Turbines and Power*, vol. 135, no. 10, 2013.

[39] J. Moeck, D. Lacoste, C. Laux, and C. Paschereit, "Control of combustion dynamics in a swirl-stabilized combustor with nanosecond repetitively pulsed discharges," in *51st AIAA Aerospace Sciences Meeting including the New Horizons Forum and Aerospace Exposition*, 2013, p. 565.

[40] A. Ehn, J. Zhu, P. Petersson, Z. Li, M. Aldén, C. Fureby, T. Hurtig, N. Zettervall, A. Larsson, and J. Larfeldt, "Plasma assisted combustion: Effects of o3 on large scale turbulent combustion studied with laser diagnostics and large eddy simulations," *Proceedings of the Combustion Institute*, vol. 35, no. 3, pp. 3487–3495, 2015.

[41] R. Rajasegar, C. Mitsingas, E. Mayhew, and T. Lee, "Experimental characterization of a swirl stabilized, direct-coupled, plasma assisted turbulent jet flame," 2015.

[42] R. Rajasegar, C. M. Mitsingas, E. K. Mayhew, S. Hammack, H. Do, and T. Lee, "Effects of continuous volumetric direct-coupled nonequilibrium atmospheric microwave plasma discharge on swirl-stabilized premixed flames," *IEEE Transactions on Plasma Science*, vol. 44, no. 1, pp. 39–48, 2015.

[43] A. Ehn, P. Petersson, J. Zhu, Z. Li, M. Aldén, E. Nilsson, J. Larfeldt, A. Larsson, T. Hurtig, N. Zettervall, *et al.*, "Investigations of microwave stimulation of a turbulent low-swirl flame," *Proceedings of the Combustion Institute*, vol. 36, no. 3, pp. 4121–4128, 2017.

[44] R. Rajasegar, C. M. Mitsingas, E. Mayhew, T. Lee, and J. Yoo, "Proper orthogonal decomposition for flame dynamics of microwave plasma assisted swirl stabilized premixed flames," in *55th AIAA Aerospace Sciences Meeting*, 2017, p. 1973.

[45] J. Choe and W. Sun, "Blowoff hysteresis, flame morphology and the effect of plasma in a swirling flow," *Journal of Physics D: Applied Physics*, vol. 51, no. 36, p. 365 201, 2018.

[46] G. Li, X. Jiang, Q. Chen, and Z. Wang, "Flame lift-off height control by a combined vane-plasma swirler," *Journal of Physics D: Applied Physics*, vol. 51, no. 34, p. 345 205, 2018.

[47] W. Cui, Y. Ren, and S. Li, "Stabilization of premixed swirl flames under flow pulsations using microsecond pulsed plasmas," *Journal of Propulsion and Power*, vol. 35, no. 1, pp. 190–200, 2019.

[48] F. Di Sabatino and D. A. Lacoste, "Enhancement of the lean stability and blow-off limits of methane-air swirl flames at elevated pressures by nanosecond repetitively pulsed discharges," *Journal of Physics D: Applied Physics*, vol. 53, no. 35, p. 355 201, 2020.

[49] T. C. Wagner, W. F. O'Brien, G. B. Northam, and J. M. Eggers, "Plasma torch igniter for scramjets," *Journal of Propulsion and Power*, vol. 5, no. 5, pp. 548–554, 1989.

[50] Y. Sato, M. Sayama, K. Ohwaki, G. Masuya, T. Komuro, K. Kudou, A. Murakami, K. Tani, Y. Wakamatsu, T. Kanda, *et al.*, "Effectiveness of plasma torches for ignition and flameholding in scramjet," *Journal of Propulsion and Power*, vol. 8, no. 4, pp. 883–889, 1992.

[51] J. L. Prebola Jr, "Performance of a plasma torch with hydrocarbon feedstocks for use in scramjet combustion," PhD thesis, Virginia Tech, 1998.

[52] I. I. Esakov, L. P. Grachev, K. V. Khodataev, V. A. Vinogradov, and D. M. Van Wie, "Propane–air mixture combustion assisted by mw discharge in a speedy airflow," *IEEE transactions on plasma science*, vol. 34, no. 6, pp. 2497–2506, 2006.

[53] T. Ombrello, X. Qin, Y. Ju, A. Gutsol, A. Fridman, and C. Carter, "Combustion enhancement via stabilized piecewise nonequilibrium gliding arc plasma discharge," *AIAA journal*, vol. 44, no. 1, pp. 142–150, 2006.

[54] A. Fridman, A. Gutsol, S. Gangoli, Y. Ju, and T. Ombrello, "Characteristics of gliding arc and its application in combustion enhancement," *Journal of Propulsion and Power*, vol. 24, no. 6, pp. 1216–1228, 2008.

[55] R. Feng, J. Li, Y. Wu, J. Zhu, X. Song, and X. Li, "Experimental investigation on gliding arc discharge plasma ignition and flame stabilization in scramjet combustor," *Aerospace Science and Technology*, vol. 79, pp. 145–153, 2018.

[56] R. Feng, J. Zhu, Z. Wang, M. Sun, H. Wang, Z. Cai, and W. Yan, "Dynamic characteristics of a gliding arc plasma-assisted ignition in a cavity-based scramjet combustor," *Acta Astronautica*, vol. 171, pp. 238–244, 2020.

[57] R. Feng, Y. Huang, J. Zhu, Z. Wang, M. Sun, H. Wang, and Z. Cai, "Ignition and combustion enhancement in a cavity-based supersonic combustor by a multi-channel gliding arc plasma," *Experimental Thermal and Fluid Science*, vol. 120, p. 110 248, 2021.

[58] S. Macheret, M. Shneider, and R. Miles, "Energy efficiency of plasma-assisted combustion in ram/scramjet engines," in *36th AIAA Plasmadynamics and Lasers Conference*, 2005, p. 5371.

[59] S. O. Macheret, M. N. Shneider, and R. B. Miles, "Plasma-assisted fuel atomization and multipoint ignition for scramjet engines," *Journal of Propulsion and Power*, vol. 36, no. 3, pp. 357–362, 2020.

[60] A. Firsov, K. V. Savelkin, D. A. Yarantsev, and S. B. Leonov, "Plasma-enhanced mixing and flameholding in supersonic flow," *Philosophical Transactions of the Royal Society A: Mathematical, Physical and Engineering Sciences*, vol. 373, no. 2048, p. 20 140 337, 2015.

[61] A. Houpt, B. Hedlund, S. Leonov, T. Ombrello, and C. Carter, "Quasi-dc electrical discharge characterization in a supersonic flow," *Experiments in Fluids*, vol. 58, no. 4, p. 25, 2017.

[62] S. B. Leonov, A. W. Houpt, and B. E. Hedlund, "Experimental study of ignition, reignition and flameholding by q-dc electrical discharge in a model scramjet," in *48th AIAA Plasmadynamics and Lasers Conference*, 2017, p. 3673.

[63] H. Do, S.-k. Im, M. A. Cappelli, and M. G. Mungal, "Plasma assisted flame ignition of supersonic flows over a flat wall," *Combustion and Flame*, vol. 157, no. 12, pp. 2298–2305, 2010.

[64] H. Do, M. A. Cappelli, and M. G. Mungal, "Plasma assisted cavity flame ignition in supersonic flows," *Combustion and Flame*, vol. 157, no. 9, pp. 1783–1794, 2010.

[65] S. Brieschenk, S. O'Byrne, and H. Kleine, "Laser-induced plasma ignition studies in a model scramjet engine," *Combustion and Flame*, vol. 160, no. 1, pp. 145–148, 2013.

[66] R. Clements, R. Smith, and P. Smy, "Enhancement of flame speed by intense microwave radiation," *Combustion Science and Technology*, vol. 26, no. 1-2, pp. 77–81, 1981.

[67] C. MacLatchy, R. Clements, and P. Smy, "An experimental investigation of the effect of microwave radiation on a propane-air flame," *Combustion and Flame*, vol. 45, pp. 161–169, 1982.

[68] D. Sullivan, S. Macheret, S. Zaidi, R. Miles, and Y. Ju, "Microwave techniques for the combustion enhancement of laminar flames," in *40th AIAA/ASME/SAE/ASEE Joint Propulsion Conference and Exhibit*, 2004, p. 3713.

[69] E. S. Stockman, S. H. Zaidi, R. B. Miles, C. D. Carter, and M. D. Ryan, "Measurements of combustion properties in a microwave enhanced flame," *Combustion and Flame*, vol. 156, no. 7, pp. 1453–1461, 2009.

[70] E. Stockman, S. Zaidi, and R. Miles, "Pulsed microwave enhancement of laminar and turbulent hydrocarbon flames," in *45th AIAA Aerospace Sciences Meeting and Exhibit*, 2007, p. 1348.

[71] S. Zaidi, E. Stockman, X. Qin, Z. Zhao, S. Macheret, Y. Ju, R. Miles, D. Sullivan, and J. Kline, "Measurements of hydrocarbon flame speed enhancement in high-q microwave cavity," in *44th AIAA Aerospace Sciences Meeting and Exhibit*, 2006, p. 1217.

[72] B. Wolk, A. DeFilippo, J.-Y. Chen, R. Dibble, A. Nishiyama, and Y. Ikeda, "Enhancement of flame development by microwave-assisted spark ignition in constant volume combustion chamber," *Combustion and flame*, vol. 160, no. 7, pp. 1225–1234, 2013.

[73] D. Hoffman, K.-U. Münch, and A. Leipertz, "Two-dimensional temperature determination in sooting flames by filtered rayleigh scattering," *Optics letters*, vol. 21, no. 7, pp. 525–527, 1996.

[74] E. Stockman, S. Zaidi, and R. Miles, "Hydrocarbon flame speed enhancement with high-power pulsed microwaves," in *38th AIAA Plasmadynamics and Lasers Conference In conjunction with the 16th International Conference on MHD Energy Conversion*, 2007, p. 4601.

[75] J. B. Michael, T. L. Chng, and R. B. Miles, "Sustained propagation of ultra-lean methane/air flames with pulsed microwave energy deposition," *Combustion and Flame*, vol. 160, no. 4, pp. 796–807, 2013.

[76] S. J. Barkley, K. Zhu, J. E. Lynch, J. B. Michael, and T. R. Sippel, "Microwave plasma enhancement of multiphase flames: On-demand control of solid propellant burning rate," *Combustion and Flame*, vol. 199, pp. 14–23, 2019.

[77] L. P. Babich, T. Loĭko, and V. Tsukerman, "High-voltage nanosecond discharge in a dense gas at a high overvoltage with runaway electrons," *Soviet Physics Uspekhi*, vol. 33, no. 7, p. 521, 1990.

[78] S. Starikovskaia, N. Anikin, S. Pancheshnyi, D. Zatsepin, and A. Y. Starikovskii, "Pulsed breakdown at high overvoltage: Development, propagation and energy branching," *Plasma Sources Science and Technology*, vol. 10, no. 2, p. 344, 2001.

[79] S. Starikovskaia, A. Y. Starikovskii, and D. Zatsepin, "Hydrogen oxidation in a stoichiometric hydrogen-air mixture in the fast ionization wave," *Combustion Theory and Modelling*, vol. 5, no. 1, pp. 97–129, 2001.

[80] D. Z. Pai, G. D. Stancu, D. A. Lacoste, and C. O. Laux, "Nanosecond repetitively pulsed discharges in air at atmospheric pressure—the glow regime," *Plasma Sources Science and Technology*, vol. 18, no. 4, p. 045 030, 2009.

[81] D. Z. Pai, D. A. Lacoste, and C. O. Laux, "Nanosecond repetitively pulsed discharges in air at atmospheric pressure—the spark regime," *Plasma Sources Science and Technology*, vol. 19, no. 6, p. 065 015, 2010.

[82] D. Z. Pai, D. A. Lacoste, and C. O. Laux, "Transitions between corona, glow, and spark regimes of nanosecond repetitively pulsed discharges in air at atmospheric pressure," *Journal of Applied Physics*, vol. 107, no. 9, p. 093 303, 2010.

[83] G. Lou, A. Bao, M. Nishihara, S. Keshav, Y. G. Utkin, J. W. Rich, W. R. Lempert, and I. V. Adamovich, "Ignition of premixed hydrocarbon–air flows by repetitively pulsed, nanosecond pulse duration plasma," *Proceedings of the Combustion Institute*, vol. 31, no. 2, pp. 3327–3334, 2007.

[84] Y. Zuzeek, S. Bowman, I. Choi, I. Adamovich, and W. Lempert, "Pure rotational cars studies of thermal energy release and ignition in nanosecond repetitively pulsed hydrogen-air plasmas," *Proceedings of the Combustion Institute*, vol. 33, no. 2, pp. 3225–3232, 2011.

[85] Z. Yin, I. Adamovich, and W. Lempert, "Oh radical and temperature measurements during ignition of h2-air mixtures excited by a repetitively pulsed nanosecond discharge," *Proceedings of the Combustion Institute*, vol. 34, no. 2, pp. 3249–3258, 2013.

[86] E. Mintusov, A. Serdyuchenko, I. Choi, W. Lempert, and I. Adamovich, "Mechanism of plasma assisted oxidation and ignition of ethylene–air flows by a repetitively pulsed nanosecond discharge," *Proceedings of the Combustion Institute*, vol. 32, no. 2, pp. 3181–3188, 2009.

[87] J. K. Lefkowitz, M. Uddi, B. C. Windom, G. Lou, and Y. Ju, "In situ species diagnostics and kinetic study of plasma activated ethylene dissociation and oxidation in a low temperature flow reactor," *Proceedings of the Combustion Institute*, vol. 35, no. 3, pp. 3505–3512, 2015.

[88] J. K. Lefkowitz, P. Guo, A. Rousso, and Y. Ju, "Species and temperature measurements of methane oxidation in a nanosecond repetitively pulsed discharge," *Philosophical Transactions of the Royal Society A: Mathematical, Physical and Engineering Sciences*, vol. 373, no. 2048, p. 20 140 333, 2015.

[89] S. Lovascio, T. Ombrello, J. Hayashi, S. Stepanyan, D. Xu, G. D. Stancu, and C. O. Laux, "Effects of pulsation frequency and energy deposition on ignition using nanosecond repetitively pulsed discharges," *Proceedings of the Combustion Institute*, vol. 36, no. 3, pp. 4079–4086, 2017.

[90] J. K. Lefkowitz and T. Ombrello, "Reduction of flame development time in nanosecond pulsed high frequency discharge ignition of flowing mixtures," *Combustion and Flame*, vol. 193, pp. 471–480, 2018.

[91] S. Nagaraja, T. Li, J. A. Sutton, I. V. Adamovich, and V. Yang, "Nanosecond plasma enhanced h2/o2/n2 premixed flat flames," *Proceedings of the Combustion Institute*, vol. 35, no. 3, pp. 3471–3478, 2015.

[92] D. A. Lacoste, Y. Xiong, J. P. Moeck, S. H. Chung, W. L. Roberts, and M. S. Cha, "Transfer functions of laminar premixed flames subjected to forcing by acoustic waves, ac electric fields, and non-thermal plasma discharges," *Proceedings of the Combustion Institute*, vol. 36, no. 3, pp. 4183–4192, 2017.

[93] I. Kossyi, A. Y. Kostinsky, A. Matveyev, and V. Silakov, "Kinetic scheme of the non-equilibrium discharge in nitrogen-oxygen mixtures," *Plasma Sources Science and Technology*, vol. 1, no. 3, p. 207, 1992.

[94] N. Popov, "Effect of a pulsed high-current discharge on hydrogen-air mixtures," *Plasma Physics Reports*, vol. 34, no. 5, pp. 376–391, 2008.

[95] D. Zatsepin, S. Starikovskaia, and A. Y. Starikovskii, "Hydrogen oxidation in the stoichiometric hydrogen-oxygen mixture in the fast ionization wave," *Combustion Theory and Modelling*, vol. 20, no. 7, pp. 66–99, 2001.

[96] I. Kosarev, N. Aleksandrov, S. Kindysheva, S. Starikovskaia, and A. Y. Starikovskii, "Kinetics of ignition of saturated hydrocarbons by nonequilibrium plasma: Ch4-containing mixtures," *Combustion and flame*, vol. 154, no. 3, pp. 569–586, 2008.

[97] N. Aleksandrov, S. Kindysheva, E. Kukaev, S. Starikovskaya, and A. Y. Starikovskii, "Simulation of the ignition of a methane-air mixture by a high-voltage nanosecond discharge," *Plasma physics reports*, vol. 35, no. 10, pp. 867–882, 2009.

[98] M. S. Bak and M. A. Cappelli, "A reduced set of air plasma reactions for nanosecond pulsed plasmas," *IEEE Transactions on Plasma Science*, vol. 43, no. 4, pp. 995–1001, 2015.

[99] H. Wang and M. Frenklach, "Detailed reduction of reaction mechanisms for flame modeling," *Combustion and Flame*, vol. 87, no. 3-4, pp. 365–370, 1991.

[100] M. S. Bak and M. A. Cappelli, "Numerical studies of nitric oxide formation in nanosecond-pulsed discharge-stabilized flames of premixed methane/air," *Philosophical Transactions of the Royal Society A: Mathematical, Physical and Engineering Sciences*, vol. 373, no. 2048, p. 20 140 331, 2015.

[101] A. Starikovskiy, "Mechanism of plasma-assisted ignition for h2 and c1-c5 hydrocarbons," in *55th AIAA Aerospace Sciences Meeting*, 2017, p. 1977.

[102] A. E. Long, R. L. Speth, and W. H. Green, "Ember: An open-source, transient solver for 1d reacting flow using large kinetic models, applied to strained extinction," *Combustion and Flame*, vol. 195, pp. 105–116, 2018.

[103] R. J. Kee, M. E. Coltrin, and P. Glarborg, *Chemically reacting flow: theory and practice*. John Wiley & Sons, 2005.

[104] T. Pedersen and R. C. Brown, "Simulation of electric field effects in premixed methane flames," *Combustion and Flame*, vol. 94, no. 4, pp. 433–448, 1993.

[105] M. Belhi, P. Domingo, and P. Vervisch, "Direct numerical simulation of the effect of an electric field on flame stability," *Combustion and flame*, vol. 157, no. 12, pp. 2286–2297, 2010.

[106] N. Speelman, L. de Goey, and J. van Oijen, "Development of a numerical model for the electric current in burner-stabilised methane–air flames," *Combustion Theory and Modelling*, vol. 19, no. 2, pp. 159–187, 2015.

[107] D. G. Goodwin, H. K. Moffat, and R. L. Speth, *Cantera: An object-oriented software toolkit for chemical kinetics, thermodynamics, and transport processes*, http://www.cantera.org, Version 2.4.0, 2018. DOI: 10.5281/zenodo.1174508.

[108] A. Luque, *Bolos: An open source solver for the boltzmann equation*, https://github.com/aluque/bolos, Version 0.1, 2014.

[109] Mechanical and U. o. C. a. S. D. Aerospace Engineering (Combustion Research), *Chemical-kinetic mechanisms for combustion applications*, http://web.eng.ucsd.edu/mae/groups/combustion/mechanism.html, update of 2016-12-14, 2016.

[110] A. Chattock, "Xliv. On the velocity and mass of the ions in the electric wind in air," *The London, Edinburgh, and Dublin Philosophical Magazine and Journal of Science*, vol. 48, no. 294, pp. 401–420, 1899.

[111] H. F. Calcote and R. N. Pease, "Electrical properties of flames. burnerflames in longitudinal electric fields.," *Industrial & Engineering Chemistry*, vol. 43, no. 12, pp. 2726–2731, 1951.

[112] H. Calcote and C. Berman, "Increased methane-air stability limits by a dc electric field," in *Proceeding of the ASME Fossil Fuels Combustion Symposium*, American Soc. of Mechanical Engineers New York, 1989, pp. 25–31.

[113] D. Bradley and S. Nasser, "Electrical coronas and burner flame stability," *Combustion and Flame*, vol. 55, no. 1, pp. 53–58, 1984.

[114] H. Jaggers and A. Von Engel, "The effect of electric fields on the burning velocity of various flames," *Combustion and Flame*, vol. 16, no. 3, pp. 275–285, 1971.

[115] M. Kono, F. Carleton, A. Jones, and F. Weinberg, "The effect of nonsteady electric fields on sooting flames," *Combustion and flame*, vol. 78, no. 3-4, pp. 357–364, 1989.

[116] S. Marcum and B. Ganguly, "Electric-field-induced flame speed modification," *Combustion and Flame*, vol. 143, no. 1-2, pp. 27–36, 2005.

[117] J. Van Den Boom, A. A. Konnov, A. Verhasselt, V. Kornilov, L. De Goey, and H. Nijmeijer, "The effect of a dc electric field on the laminar burning velocity of premixed methane/air flames," *Proceedings of the Combustion Institute*, vol. 32, no. 1, pp. 1237–1244, 2009.

[118] S. V. Jacobs and K. G. Xu, "Examination of ionic wind and cathode sheath effects in a e-field premixed flame with ion density measurements," *Physics of Plasmas*, vol. 23, no. 4, p. 043 504, 2016.

[119] J. Kuhl, T. Seeger, L. Zigan, S. Will, and A. Leipertz, "On the effect of ionic wind on structure and temperature of laminar premixed flames influenced by electric fields," *Combustion and Flame*, vol. 176, pp. 391–399, 2017.

[120] Y. Ju, S. Macheret, R. Miles, and D. Sullivan, "Numerical study of the effect of microwave discharge on the premixed methane-air flame," in *40th AIAA/ASME/SAE/ASEE Joint Propulsion Conference and Exhibit*, 2004, p. 3707.

[121] V. Naumov, S. Zhdanok, A. Starik, A. Cenian, and A. Chernukho, "Modeling of singlet oxygen production in nonequilibrium o2 gas discharge plasma," *Nonequilibrium Processes and their Applications*, pp. 62–6, 2002.

[122] C. MacLatchy, "Langmuir probe measurements of ion density in an atmospheric-pressure air-propane flame," *Combustion and Flame*, vol. 36, pp. 171–178, 1979.

[123] H. Calcote, "Mechanisms for the formation of ions in flames," *Combustion and Flame*, vol. 1, no. 4, pp. 385–403, 1957.

[124] H. F. Calcote, "Mechanisms of soot nucleation in flames—a critical review," *Combustion and Flame*, vol. 42, pp. 215–242, 1981.

[125] J. Goodings, D. Bohme, and C.-W. Ng, "Detailed ion chemistry in methane oxygen flames.," *Combustion and Flame*, vol. 36, pp. 27–62, 1979.

[126] J. Prager, U. Riedel, and J. Warnatz, "Modeling ion chemistry and charged species diffusion in lean methane–oxygen flames," *Proceedings of the Combustion Institute*, vol. 31, no. 1, pp. 1129–1137, 2007.

[127] S. Selle and U. Riedel, "Transport properties of ionized species," *Annals of the New York Academy of Sciences*, vol. 891, no. 1, pp. 72–80, 1999.

[128] J. Han, M. Belhi, F. Bisetti, and S. Mani Sarathy, "Numerical modelling of ion transport in flames," *Combustion Theory and Modelling*, vol. 19, no. 6, pp. 744–772, 2015.

[129] N. Speelman, M. Kiefer, D. Markus, U. Maas, L. de Goey, and J. van Oijen, "Validation of a novel numerical model for the electric currents in burner-stabilized methane–air flames," *Proceedings of the Combustion Institute*, vol. 35, no. 1, pp. 847–854, 2015.

[130] M. Belhi, P. Domingo, and P. Vervisch, "Modelling of the effect of dc and ac electric fields on the stability of a lifted diffusion methane/air flame," *Combustion Theory and Modelling*, vol. 17, no. 4, pp. 749–787, 2013.

[131] F. Bisetti and M. El Morsli, "Kinetic parameters, collision rates, energy exchanges and transport coefficients of non-thermal electrons in premixed flames at sub-breakdown electric field strengths," *Combustion Theory and Modelling*, vol. 18, no. 1, pp. 148–184, 2014.

[132] J. E. Jones, "On the determination of molecular fields.—ii. from the equation of state of a gas," *Proc. R. Soc. Lond. A*, vol. 106, no. 738, pp. 463–477, 1924.

[133] E. Mason, R. Munn, and F. J. Smith, "Transport coefficients of ionized gases," *The Physics of Fluids*, vol. 10, no. 8, pp. 1827–1832, 1967.

[134] G. Hagelaar and L. Pitchford, "Solving the Boltzmann equation to obtain electron transport coefficients and rate coefficients for fluid models," *Plasma Sources Science and Technology*, vol. 14, no. 4, p. 722, 2005.

[135] G. P. Smith *et al.*, *Gri-mech*, 2000. [Online]. Available: http://combustion.berkeley.edu/gri-mech/.

[136] S. Davis, C. Law, and H. Wang, "Propene pyrolysis and oxidation kinetics in a flow reactor and laminar flames," *Combustion and Flame*, vol. 119, no. 4, pp. 375–399, 1999.

[137] A. Neau, A. Al Khalili, S. Rosén, A. Le Padellec, A. Derkatch, W. Shi, L. Vikor, M. Larsson, J. Semaniak, R. Thomas, *et al.*, "Dissociative recombination of D_3O^+ and H_3O^+: Absolute cross sections and branching ratios," *The Journal of Chemical Physics*, vol. 113, no. 5, pp. 1762–1770, 2000.

[138] J. Han, "Numerical study of electric field enhanced combustion," PhD thesis, King Abdullah University of Science and Technology, 2016.

[139] D. McElroy, C. Walsh, A. Markwick, M. Cordiner, K. Smith, and T. Millar, "The umist database for astrochemistry 2012," *Astronomy & Astrophysics*, vol. 550, A36, 2013.

[140] A. M. Starik, A. M. Savel'ev, N. S. Titova, and U. Schumann, "Modeling of sulfur gases and chemiions in aircraft engines," *Aerospace Science and Technology*, vol. 6, no. 1, pp. 63–81, 2002.

[141] M. Belhi, J. Han, T. A. Casey, J.-Y. Chen, H. G. Im, S. M. Sarathy, and F. Bisetti, "Analysis of the current–voltage curves and saturation currents in burner-stabilised premixed flames with detailed ion chemistry and transport models," *Combustion Theory and Modelling*, vol. 22, no. 5, pp. 939–972, 2018.

[142] S. M. Burke, W. Metcalfe, O. Herbinet, F. Battin-Leclerc, F. M. Haas, J. Santner, F. L. Dryer, and H. J. Curran, "An experimental and modeling study of propene oxidation. part 1: Speciation measurements in jet-stirred and flow reactors," *Combustion and Flame*, vol. 161, no. 11, pp. 2765–2784, 2014.

[143] S. M. Burke, U. Burke, R. Mc Donagh, O. Mathieu, I. Osorio, C. Keesee, A. Morones, E. L. Petersen, W. Wang, T. A. DeVerter, *et al.*, "An experimental and modeling study of propene oxidation. part 2: Ignition delay time and flame speed measurements," *Combustion and Flame*, vol. 162, no. 2, pp. 296–314, 2015.

[144] A. Starik and A. Sharipov, "Theoretical analysis of reaction kinetics with singlet oxygen molecules," *Physical Chemistry Chemical Physics*, vol. 13, no. 36, pp. 16 424–16 436, 2011.

[145] A. Starik, V. Kozlov, and N. Titova, "On the influence of singlet oxygen molecules on the speed of flame propagation in methane–air mixture," *Combustion and Flame*, vol. 157, no. 2, pp. 313–327, 2010.

[146] A. Starik, V. Kozlov, and N. Titova, "On mechanisms of a flame velocity increase upon activation of o2 molecules in electrical discharge," *Journal of Physics D: Applied Physics*, vol. 41, no. 12, p. 125 206, 2008.

[147] *Morgan database*, www.lxcat.net, retrieved on April 24, 2017.

[148] *Phelps database*, www.lxcat.net, retrieved on April 24, 2017.

[149] *SIGLO database*, www.lxcat.net, retrieved on April 24, 2017.

[150] L. C. Pitchford, L. L. Alves, K. Bartschat, S. F. Biagi, M.-C. Bordage, I. Bray, C. E. Brion, M. J. Brunger, L. Campbell, A. Chachereau, *et al.*, "Lxcat: An open-access, web-based platform for data needed for modeling low temperature plasmas," *Plasma Processes and Polymers*, vol. 14, no. 1-2, p. 1 600 098, 2017.

[151] I. Glassman, *Combustion, 3'rd edition*, 1996.

[152] A. Starikovskiy and N. Aleksandrov, "Plasma-assisted ignition and combustion," *Progress in Energy and Combustion Science*, vol. 39, no. 1, pp. 61–110, 2013.

[153] Y. Ju and W. Sun, "Plasma assisted combustion: Progress, challenges, and opportunities," *Combustion and Flame*, vol. 162, no. 3, pp. 529–532, 2015.

[154] J. B. Heywood, *Internal combustion engine fundamentals*. McGraw-Hill Education, 2018.

[155] J. K. Lefkowitz and T. Ombrello, "An exploration of inter-pulse coupling in nanosecond pulsed high frequency discharge ignition," *Combustion and Flame*, vol. 180, pp. 136–147, 2017.

[156] S. Nagaraja, V. Yang, and I. Adamovich, "Multi-scale modelling of pulsed nanosecond dielectric barrier plasma discharges in plane-to-plane geometry," *Journal of Physics D: Applied Physics*, vol. 46, no. 15, p. 155 205, 2013.

[157] W. Sun, M. Uddi, T. Ombrello, S. H. Won, C. Carter, and Y. Ju, "Effects of non-equilibrium plasma discharge on counterflow diffusion flame extinction," *Proceedings of the Combustion Institute*, vol. 33, no. 2, pp. 3211–3218, 2011.

[158] K. Takita, G. Masuya, T. Sato, and Y. Ju, "Effect of addition of radicals on burning velocity," *AIAA journal*, vol. 39, no. 4, pp. 742–744, 2001.

[159] I. V. Adamovich and W. R. Lempert, "Challenges in understanding and predictive model development of plasma-assisted combustion," *Plasma Physics and Controlled Fusion*, vol. 57, no. 1, p. 014 001, 2014.

[160] A. Dogariu, B. M. Goldberg, S. O'Byrne, and R. B. Miles, "Species-independent femtosecond localized electric field measurement," *Physical Review Applied*, vol. 7, no. 2, p. 024 024, 2017.

[161] B. M. Goldberg, T. L. Chng, A. Dogariu, and R. B. Miles, "Electric field measurements in a near atmospheric pressure nanosecond pulse discharge with picosecond electric field induced second harmonic generation," *Applied Physics Letters*, vol. 112, no. 6, p. 064 102, 2018.

[162] N. Popov, "Fast gas heating in a nitrogen–oxygen discharge plasma: I. kinetic mechanism," *Journal of Physics D: Applied Physics*, vol. 44, no. 28, p. 285 201, 2011.

[163] E. Mintoussov, S. Pendleton, F. Gerbault, N. Popov, and S. Starikovskaia, "Fast gas heating in nitrogen–oxygen discharge plasma: Ii. energy exchange in the afterglow of a volume nanosecond discharge at moderate pressures," *Journal of Physics D: Applied Physics*, vol. 44, no. 28, p. 285 202, 2011.

[164] N. Popov, "Kinetics of plasma-assisted combustion: Effect of non-equilibrium excitation on the ignition and oxidation of combustible mixtures," *Plasma Sources Science and Technology*, vol. 25, no. 4, p. 043 002, 2016.

[165] T. A. Casey, J. Han, M. Belhi, P. G. Arias, F. Bisetti, H. G. Im, and J.-Y. Chen, "Simulations of planar non-thermal plasma assisted ignition at atmospheric pressure," *Proceedings of the Combustion Institute*, vol. 36, no. 3, pp. 4155–4163, 2017.

[166] A. Shioyoke, J. Hayashi, R. Murai, N. Nakatsuka, and F. Akamatsu, "Numerical investigation on effects of nonequilibrium plasma on laminar burning velocity of ammonia flame," *Energy & fuels*, vol. 32, no. 3, pp. 3824–3832, 2018.

[167] S. H. Won, B. Jiang, P. Diévart, C. H. Sohn, and Y. Ju, "Self-sustaining n-heptane cool diffusion flames activated by ozone," *Proceedings of the Combustion Institute*, vol. 35, no. 1, pp. 881–888, 2015.

[168] S. Yang, S. Nagaraja, W. Sun, and V. Yang, "Multiscale modeling and general theory of non-equilibrium plasma-assisted ignition and combustion," *Journal of Physics D: Applied Physics*, vol. 50, no. 43, p. 433 001, 2017.

[169] I. V. Adamovich, T. Li, and W. R. Lempert, "Kinetic mechanism of molecular energy transfer and chemical reactions in low-temperature air-fuel plasmas," *Philosophical Transactions of the Royal Society A: Mathematical, Physical and Engineering Sciences*, vol. 373, no. 2048, p. 20 140 336, 2015.

[170] A. Montello, Z. Yin, D. Burnette, I. Adamovich, and W. Lempert, "Picosecond cars measurements of nitrogen vibrational loading and rotational/translational temperature in non-equilibrium discharges," *Journal of Physics D: Applied Physics*, vol. 46, no. 46, p. 464 002, 2013.

[171] S. Chapman, "The kinetic theory of simple and composite monatomic gases: Viscosity, thermal conduction, and diffusion," *Proceedings of the Royal Society of London. Series A, Containing Papers of a Mathematical and Physical Character*, vol. 93, no. 646, pp. 1–20, 1916.

[172] A. Fridman and L. A. Kennedy, *Plasma physics and engineering*. CRC press, 2021.

[173] P. Virtanen, R. Gommers, T. E. Oliphant, M. Haberland, T. Reddy, D. Cournapeau, E. Burovski, P. Peterson, W. Weckesser, J. Bright, S. J. van der Walt, M. Brett, J. Wilson, K. Jarrod Millman, N. Mayorov, A. R. J. Nelson, E. Jones, R. Kern, E. Larson, C. Carey, İ. Polat, Y. Feng, E. W. Moore, J. Vand erPlas, D. Laxalde, J. Perktold, R. Cimrman, I. Henriksen, E. A. Quintero, C. R. Harris, A. M. Archibald, A. H. Ribeiro, F. Pedregosa, P. van Mulbregt, and S. 1. 0. Contributors, "SciPy 1.0: Fundamental Algorithms for Scientific Computing in Python," *Nature Methods*, 2020. DOI: https://doi.org/10.1038/s41592-019-0686-2.

[174] *IST-Lisbon database*, www.lxcat.net, retrieved on February 15, 2020.

[175] B. F. Gordiets, C. M. Ferreira, V. L. Guerra, J. M. Loureiro, J. Nahorny, D. Pagnon, M. Touzeau, and M. Vialle, "Kinetic model of a low-pressure n/sub 2/-o/sub 2/flowing glow discharge," *IEEE Transactions on Plasma Science*, vol. 23, no. 4, pp. 750–768, 1995.

[176] Z. S. Eckert, "Energy transfer in non-equilibrium reacting gas flows: Applications in plasma assisted combustion and chemical gas lasers," PhD thesis, The Ohio State University, 2018.

[177] G. V. Candler, J. D. Kelley, S. O. Macheret, M. N. Shneider, and I. V. Adamovich, "Vibrational excitation, thermal nonuniformities, and unsteady effects on supersonic blunt bodies," *AIAA journal*, vol. 40, no. 9, pp. 1803–1810, 2002.

[178] B. J. McBride, *NASA Glenn coefficients for calculating thermodynamic properties of individual species*. National Aeronautics and Space Administration, John H. Glenn Research Center …, 2002.

[179] A. C. DeFilippo and J.-Y. Chen, "Modeling plasma-assisted methane–air ignition using pre-calculated electron impact reaction rates," *Combustion and Flame*, vol. 172, pp. 38–48, 2016.

[180] A. Burcat and B. Ruscic, *Third millennium ideal gas and condensed phase thermochemical database for combustion with updates from active thermochemical tables*, http://garfield.chem.elte.hu/Burcat/burcat.html, Report TAE960, 2005.

[181] A. E. Long, H. Burbano, R. L. Speth, A. Movaghar, F. N. Egolfopoulos, and W. H. Green, "An apparatus-independent extinction strain rate in counterflow flames," *Proceedings of the Combustion Institute*, vol. 37, no. 2, pp. 1979–1987, 2019.

[182] L. Pedersen, P. Glarborg, K. Dam-Johansen, P. Hepburn, and G. Hesselmann, "A chemical engineering model for predicting no emissions and burnout from pulverised coal flames," *Combustion science and technology*, vol. 132, no. 1-6, pp. 251–314, 1998.

[183] R. F. Monaghan and A. F. Ghoniem, "A dynamic reduced order model for simulating entrained flow gasifiers: Part i: Model development and description," *Fuel*, vol. 91, no. 1, pp. 61–80, 2012.

[184] R. F. Monaghan and A. F. Ghoniem, "A dynamic reduced order model for simulating entrained flow gasifiers. part ii: Model validation and sensitivity analysis," *Fuel*, vol. 94, pp. 280–297, 2012.

[185] S. Huang, Y. Wu, K. Zhang, D. Jin, Z. Zhang, and Y. Li, "Experimental investigation of spray characteristics of gliding arc plasma airblast fuel injector," *Fuel*, vol. 293, p. 120 382, 2021.

[186] H. K. Khattak, P. Bianucci, and A. D. Slepkov, "Linking plasma formation in grapes to microwave resonances of aqueous dimers," *Proceedings of the National Academy of Sciences*, vol. 116, no. 10, pp. 4000–4005, 2019.

[187] J. Warnatz, "Rate coefficients in the C/H/O system," in *Combustion chemistry*, Springer, 1984, pp. 197–360.

[188] A. N. Eraslan and R. C. Brown, "Chemiionization and ion-molecule reactions in fuel-rich acetylene flames," *Combustion and flame*, vol. 74, no. 1, pp. 19–37, 1988.

[189] A. Hayhurst, "The mass spectrometric sampling of ions from atmospheric pressure flames as exemplified by the reactions of OH^- and O_2^- in O_2^- rich flames," *Pure and applied chemistry*, vol. 65, no. 2, pp. 285–295, 1993.

[190] M. Capitelli, C. M. Ferreira, B. F. Gordiets, and A. I. Osipov, *Plasma kinetics in atmospheric gases*. Springer Science & Business Media, 2013, vol. 31.

[191] D. Bohme, J. Goodings, and C.-W. Ng, "In situ chemical ionization as a probe for neutral constituents upstream in a methane-oxygen flame," *International Journal of Mass Spectrometry and Ion Physics*, vol. 24, no. 3, pp. 335–354, 1977.

[192] M. S. Bak, H. Do, M. G. Mungal, and M. A. Cappelli, "Plasma-assisted stabilization of laminar premixed methane/air flames around the lean flammability limit," *Combustion and Flame*, vol. 159, no. 10, pp. 3128–3137, 2012.

[193] T. Ombrello, S. H. Won, Y. Ju, and S. Williams, "Flame propagation enhancement by plasma excitation of oxygen. part i: Effects of o3," *Combustion and flame*, vol. 157, no. 10, pp. 1906–1915, 2010.

[194] T. Ombrello, S. H. Won, Y. Ju, and S. Williams, "Flame propagation enhancement by plasma excitation of oxygen. part ii: Effects of o2(a1dg)," *Combustion and Flame*, vol. 157, no. 10, pp. 1916–1928, 2010.

[195] M. Pinchak, T. Ombrello, C. Carter, E. Gutmark, and V. Katta, "The effects of hydrodynamic stretch on the flame propagation enhancement of ethylene by addition of ozone," *Philosophical Transactions of the Royal Society A: Mathematical, Physical and Engineering Sciences*, vol. 373, no. 2048, p. 20 140 339, 2015.

[196] Y. Cao, S. Li, L. Petzold, and R. Serban, "Adjoint sensitivity analysis for differential-algebraic equations: The adjoint dae system and its numerical solution," *SIAM journal on scientific computing*, vol. 24, no. 3, pp. 1076–1089, 2003.

A. CHEMISTRY

Table A.1. Detailed ion reaction mechanism. Reaction rate coefficient in (cm, mole, s, K).

*Branching ratio: n1(H_2O + H) = 0.18, n2(OH + H_2) = 0.11, n3(OH + H + H) = 0.67, and n4(O + H_2 + H) = 0.04

(a) $k = 1.523\times10^{21} T_e^{-1.0} \exp(100.0/T_{gas}) \exp(-700.0/T_e)$

(b) $k = 3.590\times10^{21} T_e^{-2.0} \exp(1430/T_{gas}) \exp(-1500.0/T_e)$

Reaction	A	n	E_a	**Ref.**
1. $CH + O \longrightarrow CHO^+ + e$	2.51×10^{11}	0.0	1700	[126], [187]
2. $HCO^+ + e \longleftrightarrow CO + H$	7.400×10^{18}	-0.68	0.0	[126], [139]
3. $HCO^+ + H_2O \longleftrightarrow H_3O^+ + CO$	1.506×10^{15}	0.0	0.0	[126], [139]
4. $H_3O^+ + e \longrightarrow$ *neutral species	EEDF			[139]
5. $H_3O^+ + C \longleftrightarrow HCO^+ + H_2$	6.022×10^{12}	0.0	0.0	[126], [139]
6. $HCO^+ + CH_2CO \longleftrightarrow C_2H_3O^+ + CO$	1.259×10^{15}	-0.048	0.0	[126], [139]
7. $HCO^+ + CH_3 \longleftrightarrow C_2H_3O^+ + H$	7.763×10^{14}	-0.006	0.0	[126], [188]
8. $C_2H_3O^+ + e \longleftrightarrow CH_2CO + H$	2.291×10^{18}	-0.5	0.0	[126], [139]
9. $H_3O^+ + CH_2CO \longleftrightarrow C_2H_3O^+ + H_2O$	1.204×10^{15}	0.0	0.0	[126], [139]
10. $C_2H_3O^+ + e \longleftrightarrow CO + CH_3$	2.403×10^{17}	-0.05	0.0	[126], [139]
11. $C_2H_3O^+ + O \longleftrightarrow HCO^+ + CH_2O$	2.000×10^{14}	0.0	0.0	[126]
12. $HCO^+ + CH_3OH \longleftrightarrow CH_5O^+ + CO$	8.710×10^{14}	-0.056	0.0	[126], [139]
13. $H_3O^+ + CH_3OH \longleftrightarrow CH_5O^+ + H_2O$	1.506×10^{15}	0.0	0.0	[126], [139]
14. $CH_5O^+ + e \longleftrightarrow CH_3OH + H$	2.403×10^{17}	-0.05	0.0	[126], [139]
15. $CH_5O^+ + CH_2CO \longleftrightarrow C_2H_3O^+ + CH_3OH$	1.486×10^{15}	-0.077	-41.73	[126]
16. $O_2^- + H_2 \longleftrightarrow H_2O_2 + e$	6.022×10^{15}	0.0	0.0	[126]
17. $O_2^- + H \longleftrightarrow HO_2 + e$	7.226×10^{14}	0.0	0.0	[79], [126]
18. $O_2^- + OH \longleftrightarrow OH^- + O_2$	6.022×10^{13}	0.0	0.0	[126], [189]

Continued on next page

Table A.1 – continued from previous page

Reaction	A	n	E_a	**Ref.**
19. $O_2^- + H \longleftrightarrow OH^- + O$	1.084×10^{15}	0.0	0.0	[79], [126]
20. $OH^- + O \longleftrightarrow HO_2 + e$	1.204×10^{14}	0.0	0.0	[125], [126]
21. $OH^- + H \longleftrightarrow H_2O + e$	1.084×10^{15}	0.0	0.0	[126], [139]
22. $OH^- + C \longleftrightarrow HCO + e$	3.001×10^{14}	0.0	0.0	[126], [139]
23. $OH^- + CH \longleftrightarrow CH_2O + e$	3.001×10^{14}	0.0	0.0	[126], [139]
24. $OH^- + CH_3 \longleftrightarrow CH_3OH + e$	6.022×10^{14}	0.0	0.0	[126], [139]
25. $CO_3^- + H \longleftrightarrow OH^- + CO_2$	1.020×10^{14}	0.0	0.0	[125], [126]
26. $CO_3^- + O \longleftrightarrow O_2^- + CO_2$	4.600×10^{13}	0.0	0.0	[125], [126]
27. $CHO_2^- + H \longleftrightarrow CO_2 + H_2 + e$	1.159×10^{14}	0.0	0.0	[126]
28. $OH^- + HCO \longleftrightarrow CHO_2^- + H$	2.959×10^{15}	-0.14	-53.04	[126]
29. $O^- + C \longleftrightarrow CO + e$	3.011×10^{14}	0.0	0.0	[126], [139]
30. $O^- + H_2 \longleftrightarrow OH^- + H$	1.987×10^{13}	0.0	0.0	[126], [139]
31. $O^- + CH_4 \longleftrightarrow OH^- + CH_3$	6.022×10^{13}	0.0	0.0	[126], [139]
32. $O^- + H_2O \longleftrightarrow OH^- + OH$	8.431×10^{14}	0.0	0.0	[126], [190]
33. $O^- + CH_2O \longleftrightarrow OH^- + HCO$	5.601×10^{14}	0.0	0.0	[126], [191]
34. $O^- + CH_2O \longleftrightarrow CHO_2^- + H$	1.307×10^{15}	0.0	0.0	[126], [191]
35. $O^- + C_2H_6 \longleftrightarrow C_2H_5 + OH^-$	6.130×10^{15}	-0.5	0.0	[126], [140]
36. $O^- + H \longleftrightarrow OH + e$	3.011×10^{14}	0.0	0.0	[126], [139]
37. $O^- + H_2 \longleftrightarrow H_2O + e$	4.215×10^{14}	0.0	0.0	[126], [139]
38. $O^- + CH \longleftrightarrow HCO + e$	3.011×10^{14}	0.0	0.0	[126], [139]
39. $O^- + CH_2\cdot \longleftrightarrow CH_2O + e$	3.011×10^{14}	0.0	0.0	[126], [139]
40. $O^- + CO \longleftrightarrow CO_2 + e$	3.914×10^{14}	0.0	0.0	[126], [139]
41. $O^- + O \longleftrightarrow O_2 + e$	8.431×10^{13}	0.0	0.0	[126], [139]
42. $O^- + C_2H_2 \longleftrightarrow CH_2CO + e$	7.226×10^{14}	0.0	0.0	[125], [126]
43. $O^- + H_2O \longrightarrow H_2O_2 + e$	3.613×10^{11}	0.0	0.0	[138]
44. $O_2^- + O \longleftrightarrow O^- + O_2$	1.987×10^{14}	0.0	0.0	[126], [190]
45. $O_2^- + C_2H_3O^+ \longleftrightarrow O_2 + CH_2CHO$	2.090×10^{18}	-0.50	0.0	[93], [140]

Continued on next page

Table A.1 – continued from previous page

Reaction	A	n	E_a	**Ref.**
46. $O_2^- + C_2H_3O^+ \longleftrightarrow O_2 + CH_2CO + H$	6.020×10^{16}	0.0	0.0	[93], [140]
47. $O_2^- + CH_5O^+ \longleftrightarrow O_2 + CH_3 + H_2O$	6.020×10^{16}	0.0	0.0	[93], [140]
48. $O^- + C_2H_3O^+ \longleftrightarrow O + CH_2CHO$	2.090×10^{18}	-0.50	0.0	[93], [140]
49. $O^- + C_2H_3O^+ \longleftrightarrow O + CH_2CO + H$	6.020×10^{16}	0.0	0.0	[93], [140]
50. $O^- + CH_5O^+ \longleftrightarrow O + CH_3 + H_2O$	6.020×10^{16}	0.0	0.0	[93], [140]
51. $HCO_3^- + C_2H_3O^+ \longleftrightarrow CH_2CHO + CO_2 + OH$	6.020×10^{16}	0.0	0.0	[93], [140]
52. $HCO_3^- + CH_5O^+ \longleftrightarrow CH_3OH + H_2O + CO_2$	6.020×10^{16}	0.0	0.0	[93], [140]
53. $O_2 + e + O \longleftrightarrow O_2^- + O$	3.627×10^{16}	0.0	0.0	[126], [190]
54. $O_2 + e + O_2 \longleftrightarrow O_2^- + O_2$	(a)			[190]
55. $O_2 + e + H_2O \longleftrightarrow O_2^- + H_2O$	5.077×10^{18}	0.0	0.0	[126], [190]
56. $O_2 + e + N_2 \longleftrightarrow O_2^- + N_2$	(b)			[190]
57. $e + OH + M \longleftrightarrow OH^- + M$	1.088×10^{17}	0.0	0.0	[126], [189]
Third body efficiencies = H_2:1.0, H_2O:6.5, O_2:0.4, N_2:0.4, CO:0.75, CO_2:1.5, CH_4:3.0				
58. $OH^- + CO_2 + O_2 \longleftrightarrow HCO_3^- + O_2$	2.760×10^{20}	0.0	0.0	[125], [126]
59. $OH^- + CO_2 + H_2O \longleftrightarrow HCO_3^- + H_2O$	1.104×10^{21}	0.0	0.0	[126]
60. $e + O + O_2 \longleftrightarrow O^- + O_2$	3.627×10^{16}	0.0	0.0	[126], [190]
61. $e + O + O \longleftrightarrow O^- + O$	3.021×10^{17}	0.0	0.0	[79], [126]
62. $O^- + CO_2 + O_2 \longleftrightarrow CO_3^- + O_2$	1.123×10^{20}	0.0	0.0	[125], [126]
63. $CO_3^- + OH \longrightarrow HO_2 + CO_2 + e$	3.550×10^{15}	-0.25	0.0	[138]
64. $HCO_3^- + OH \longleftrightarrow CO_3^- + H_2O$	3.500×10^{15}	-0.25	0.0	[138]
65. $O_2^- + H_3O^+ \longleftrightarrow O_2 + H + H_2O$	7.833×10^{17}	-0.5	0.0	[139]
66. $OH^- + H_3O^+ \longleftrightarrow OH + H + H_2O$	7.833×10^{17}	-0.5	0.0	[139]
67. $O_2^- + HCO^+ \longleftrightarrow O_2 + HCO$	3.922×10^{17}	-0.5	0.0	[139]
68. $OH^- + HCO^+ \longleftrightarrow OH + H + CO$	3.922×10^{17}	-0.5	0.0	[139]

Table A.2. Plasma reaction mechanism where the reaction rate coefficients are in units of cm, s, and K and v and w in reactions 15 to 17 are the levels of the vibrational states.

Reaction	A	n	E_a	**Ref.**
1. $N_2 + e \longrightarrow N_2(A^3) + e$	EEDF			[169]
2. $N_2 + e \longrightarrow N_2(B^3) + e$	EEDF			[169]
3. $N_2 + e \longrightarrow N_2(C^3) + e$	EEDF			[169]
4. $N_2 + e \longrightarrow N_2(a) + e$	EEDF			[169]
5. $N_2 + e \longrightarrow N + N + e$	EEDF			[169]
6. $N_2 + e \longrightarrow N_2^+ + e + e$	EEDF			[169]
7. $O_2 + e \longrightarrow O_2(a^1) + e$	EEDF			[169]
8. $O_2 + e \longrightarrow O_2(b^1) + e$	EEDF			[169]
9. $O_2 + e \longrightarrow O + O + e$	EEDF			[169]
10. $O_2 + e \longrightarrow O + O(^1D) + e$	EEDF			[169]
11. $O_2 + e \longrightarrow O + O(^1D) + e$	EEDF			[169]
12. $O_2 + e \longrightarrow O + O(^1S) + e$	EEDF			[169]
13. $O_2 + e \longrightarrow O_2^+ + e + e$	EEDF			[169]
14. $O_2 + e \longrightarrow O^- + O$	EEDF			[98]
15. $N_2(v) + e \longrightarrow N_2(v+1) + e$	EEDF			[169]
16. $N_2(v+1) + O \longrightarrow N_2(v) + O$	Eqn. (3.17)			[169]
17. $N_2(v) + N_2(w+1) \longrightarrow N_2(v+1) + N_2(w)$	Eqn. (3.20)			[169]
18. $N_2(A^3) + O_2 \longrightarrow N_2 + O + O$	2.5×10^{-12}	0.0	0.0	[169]
19. $N_2(A^3) + O_2 \longrightarrow N_2 + O_2(a^1)$	8.68×10^{-15}	0.55	0.0	[169]
20. $N_2(A^3) + O_2 \longrightarrow N_2 + O_2(b^1)$	8.68×10^{-15}	0.55	0.0	[169]
21. $N_2(A^3) + O_2 \longrightarrow N_2O + O$	8.68×10^{-16}	0.55	0.0	[169]
22. $N_2(A^3) + O \longrightarrow N_2 + O(^1S)$	2.1×10^{-11}	0.0	0.0	[169]
23. $N_2(A^3) + O \longrightarrow NO + N(^2D)$	7.0×10^{-12}	0.0	0.0	[169]

Continued on next page

Table A.2 – continued from previous page

Reaction	A	n	E_a	**Ref.**
24. $N_2(A^3) + N_2 \longrightarrow N_2 + N_2$	3.0×10^{-18}	0.0	0.0	[169]
25. $N_2(A^3) + N \longrightarrow N_2 + N(^2P)$	1.79×10^{-19}	-0.67	0.0	[169]
26. $N_2(A^3) + NO \longrightarrow N_2 + NO$	7.0×10^{-11}	0.0	0.0	[169]
27. $N_2(A^3) + N_2O \longrightarrow N_2 + N + NO$	1.0×10^{-11}	0.0	0.0	[169]
28. $N_2(A^3) + N_2(A^3) \longrightarrow N_2(C^3) + N_2$	5.54×10^{-4}	-2.64	0.0	[169]
29. $N_2(B^3) + O_2 \longrightarrow N_2 + O + O$	3.0×10^{-10}	0.0	0.0	[169]
30. $N_2(a) + O_2 \longrightarrow N_2 + O + O$	3.0×10^{-10}	0.0	0.0	[169]
31. $N_2(C^3) + O_2 \longrightarrow N_2 + O + O(^1S)$	3.0×10^{-10}	0.0	0.0	[169]
32. $N_2(B^3) + O \longrightarrow NO + N(^2D)$	3.0×10^{-10}	0.0	0.0	[169]
33. $N_2(a) + O \longrightarrow NO + N(^2D)$	3.0×10^{-10}	0.0	0.0	[169]
34. $N_2(C^3) + O \longrightarrow NO + N(^2D)$	3.0×10^{-10}	0.0	0.0	[169]
35. $N_2(B^3) + N_2 \longrightarrow N_2(A^3) + N_2$	5.0×10^{-11}	0.0	0.0	[169]
36. $N_2(B^3) + N_2 \longrightarrow N_2(A^3) + N_2$	5.0×10^{-11}	0.0	0.0	[169]
37. $N_2(B^3) \longrightarrow N_2(A^3)$	1.5×10^{5}	0.0	0.0	[169]
38. $N_2(B^3) + NO \longrightarrow N_2(A^3) + NO$	2.4×10^{-10}	0.0	0.0	[169]
39. $N_2(a) + N_2 \longrightarrow N_2(B^3) + N_2$	2.0×10^{-13}	0.0	0.0	[169]
40. $N_2(a) + NO \longrightarrow N_2 + N + O$	3.6×10^{-10}	0.0	0.0	[169]
41. $N_2(C^3) \longrightarrow N_2(B^3)$	3.0×10^{7}	0.0	0.0	[169]
42. $N_2(C^3) + N_2 \longrightarrow N_2(a) + N_2$	1.0×10^{-11}	0.0	0.0	[169]
43. $O_2(a^1) + O_3 \longrightarrow O_2 + O_2 + O$	9.7×10^{-13}	0.0	1564	[169]
44. $O_2(a^1) + O_2 \longrightarrow O_2 + O_2$	2.3×10^{-20}	0.0	0.0	[169]
45. $O_2(a^1) + O \longrightarrow O_2 + O$	7.0×10^{-16}	0.0	0.0	[169]
46. $O_2(a^1) + N \longrightarrow NO + O$	2.0×10^{-14}	0.0	600.0	[169]
47. $O_2(a^1) + N_2 \longrightarrow O_2 + N_2$	3.0×10^{-21}	0.0	600.0	[169]
48. $O_2(a^1) + NO \longrightarrow O_2 + NO$	2.5×10^{-11}	0.0	0.0	[169]
49. $O_2(b^1) + O_3 \longrightarrow O_2 + O_2 + O$	1.8×10^{-11}	0.0	0.0	[169]
50. $O_2(b^1) + O_2 \longrightarrow O_2(a^1) + O_2$	4.3×10^{-22}	2.4	241	[169]

Continued on next page

Table A.2 – continued from previous page

Reaction	A	n	E_a	**Ref.**
51. $O_2(b^1) + O \longrightarrow O_2(a^1) + O$	8.0×10^{-14}	0.0	0.0	[169]
52. $O_2(b^1) + O \longrightarrow O_2 + O(^1D)$	6.0×10^{-11}	-0.1	4201	[169]
53. $O_2(b^1) + N_2 \longrightarrow O_2(a^1) + N_2$	4.9×10^{-15}	0.0	253	[169]
54. $O_2(b^1) + NO \longrightarrow O_2(a^1) + NO$	4.0×10^{-14}	0.0	0.0	[169]
55. $N(^2D) + O_2 \longrightarrow N + O + O$	8.66×10^{-14}	0.5	0.0	[169]
56. $N(^2D) + O_2 \longrightarrow N + O + O(^1D)$	3.46×10^{-13}	0.5	0.0	[169]
57. $N(^2D) + N_2 \longrightarrow N + N_2$	2.0×10^{-14}	0.0	0.0	[169]
58. $N(^2D) + NO \longrightarrow N_2O$	6.0×10^{-11}	0.0	0.0	[169]
59. $N(^2D) + N_2O \longrightarrow NO + N_2$	3.0×10^{-12}	0.0	0.0	[169]
60. $N(^2D) + O_2 \longrightarrow NO + O$	2.6×10^{-12}	0.0	0.0	[169]
61. $N(^2D) + N_2 \longrightarrow N(^2D) + N_2$	2.0×10^{-18}	0.0	0.0	[169]
62. $N(^2P) + N \longrightarrow N(^2D) + N$	1.8×10^{-12}	0.0	0.0	[169]
63. $N(^2P) + NO \longrightarrow N(A^3) + O$	3.4×10^{-11}	0.0	0.0	[169]
64. $O(^1D) + O_2 \longrightarrow O + O_2(b^1)$	2.56×10^{-11}	0.0	-67	[169]
65. $O(^1D) + O_2 \longrightarrow O + O_2$	6.4×10^{-12}	0.0	-67	[169]
66. $O(^1D) + O_3 \longrightarrow O + O + O_2$	2.3×10^{-10}	0.0	0.0	[169]
67. $O(^1D) + O_3 \longrightarrow O_2 + O_2$	1.2×10^{-10}	0.0	0.0	[169]
68. $O(^1D) + N_2O \longrightarrow NO + NO$	7.2×10^{-11}	0.0	0.0	[169]
69. $O(^1D) + N_2O \longrightarrow N_2 + O_2$	4.4×10^{-11}	0.0	0.0	[169]
70. $O(^1D) + N_2 \longrightarrow O + N_2$	1.8×10^{-11}	0.0	-107	[169]
71. $O(^1D) + NO \longrightarrow N + O_2$	1.7×10^{-10}	0.0	0.0	[169]
72. $O(^1S) + O_2 \longrightarrow O(^1D) + O_2$	1.33×10^{-12}	0.0	850	[169]
73. $O(^1S) + O_3 \longrightarrow O(^1D) + O + O_2$	2.9×10^{-10}	0.0	0.0	[169]
74. $O(^1S) + O_3 \longrightarrow O_2 + O_2$	2.9×10^{-10}	0.0	0.0	[169]
75. $O(^1S) + O \longrightarrow O(^1D) + O$	5.0×10^{-11}	0.0	301	[169]
76. $O(^1S) + O_2(a_1) \longrightarrow O(^1D) + O_2(b_1)$	3.6×10^{-11},	0.0	0.0	[169]
77. $O(^1S) + O_2(a_1) \longrightarrow O + O + O$	3.4×10^{-11}	0.0	0.0	[169]

Continued on next page

Table A.2 – continued from previous page

Reaction	A	n	E_a	**Ref.**
78. $O(^1S) + O_2(a_1) \longrightarrow O + O_2(a_1)$	1.3×10^{-10}	0.0	0.0	[169]
79. $O(^1S) + N_2 \longrightarrow N + NO$	5.0×10^{-17},	0.0	0.0	[169]
80. $O(^1S) + N_2O \longrightarrow O + N_2O$	6.3×10^{-12}	0.0	0.0	[169]
81. $O(^1S) + N_2O \longrightarrow O(^1D) + N_2O$	3.1×10^{-12}	0.0	0.0	[169]
82. $O(^1S) + NO \longrightarrow O + NO$	2.9×10^{-10}	0.0	0.0	[169]
83. $O(^1S) + NO \longrightarrow O(^1D) + NO$	5.1×10^{-10}	0.0	0.0	[169]
84. $N + O_2 \longleftrightarrow NO + O$	1.1×10^{-14}	1.0	3150	[169]
85. $N + O_3 \longleftrightarrow NO + O_2$	2.0×10^{-16}	0.0	0.0	[169]
86. $N + NO \longleftrightarrow N_2 + O$	1.05×10^{-12}	0.5	0.0	[169]
87. $N + NO_2 \longleftrightarrow N_2 + O_2$	7.0×10^{-13}	0.0	0.0	[169]
88. $N + NO_2 \longleftrightarrow N_2 + O + O$	9.1×10^{-13}	0.0	0.0	[169]
89. $N + NO_2 \longleftrightarrow N_2O + O$	3.0×10^{-12}	0.0	0.0	[169]
90. $N + NO_2 \longleftrightarrow NO + NO$	2.3×10^{-12}	0.0	0.0	[169]
91. $O + NO_2 \longleftrightarrow NO + O_2$	3.26×10^{-12}	0.18	0.0	[169]
92. $O + O_3 \longleftrightarrow O_2 + O_2$	2.0×10^{-11}	0.0	2300	[169]
93. $O + NO_3 \longleftrightarrow O_2 + NO_2$	1.0×10^{-11}	0.0	0.0	[169]
94. $O + N_2O_5 \longleftrightarrow N_2 + 3\,O_2$	3.0×10^{-16}	0.0	0.0	[169]
95. $NO + O_3 \longleftrightarrow O_2 + NO_2$	2.5×10^{-13}	0.0	765	[169]
96. $NO + NO_3 \longleftrightarrow NO_2 + NO_2$	1.7×10^{-11}	0.0	0.0	[169]
97. $NO_2 + O_3 \longleftrightarrow O_2 + NO_3$	1.2×10^{-13}	0.0	2450	[169]
98. $NO_3 + NO_3 \longleftrightarrow O_2 + NO_2 + NO_2$	5.0×10^{-12}	0.0	3000	[169]
99. $NO_2 + NO_3 \longleftrightarrow NO + NO_2 + O_2$	2.3×10^{-13}	0.0	1600	[169]
100. $N + N + M \longleftrightarrow N_2 + M$	8.27×10^{-34}	0.0	-500	[169]
101. $O + O + N_2 \longleftrightarrow O_2 + N_2$	2.76×10^{-34}	0.0	-720	[169]
102. $O + O + O_2 \longleftrightarrow O_2 + O_2$	2.45×10^{-31}	-0.63	0.0	[169]
103. $N + O + M \longleftrightarrow NO + M$	1.76×10^{-31}	-0.5	0.0	[169]
104. $O + O_2 + N_2 \longleftrightarrow O_3 + N_2$	5.58×10^{-29}	-2.0	0.0	[169]

Continued on next page

Table A.2 – continued from previous page

Reaction	A	n	E_a	**Ref.**
105. $O + O_2 + O_2 \longleftrightarrow O_3 + O_2$	8.62×10^{-31}	-1.25	0.0	[169]
106. $O + NO + M \longleftrightarrow NO_2 + M$	2.0×10^{-30}	-0.8	-443	[169]
107. $O + NO_2 + M \longleftrightarrow NO_3 + M$	1.4×10^{-30}	-0.8	-513	[169]
108. $NO_2 + NO_2 + M \longleftrightarrow N_2O_4 + M$	2.0×10^{-31}	-1.3	-453	[169]
109. $NO_2 + NO_3 + M \longleftrightarrow N_2O_5 + M$	1.0×10^{-31}	-0.5	-604	[169]
110. $N_2^+ + O_2 \longrightarrow O_2^+ + N_2$	1.04×10^{-09}	-0.5	0.0	[162]
111. $O_4^+ + e \longrightarrow O + O + O_2$	6.49×10^{-05}	-0.48	0.0	[162]
112. $O_2^- + O_3 \longrightarrow O_3^- + O_2$	4.0×10^{-10}	0.0	0.0	[162]
113. $O_4^- + O \longrightarrow O_3^- + O_2$	4.0×10^{-10}	0.0	0.0	[162]
114. $O_2^- + O_4^+ + O_2 \longrightarrow 2\,O + 3\,O_2$	3.118×10^{-19}	-2.5	0.0	[162]
115. $O_4^- + O_2^+ + O_2 \longrightarrow 2\,O + 3\,O_2$	3.118×10^{-19}	-2.5	0.0	[162]
116. $O_4^- + O_4^+ + O_2 \longrightarrow 2\,O + 4\,O_2$	3.118×10^{-19}	-2.5	0.0	[162]
117. $O_2^+ + e \longrightarrow O + O$	6.0×10^{-5}	-1.0	0.0	[98], [162]
118. $e + O_2 + O_2 \longrightarrow O_2^- + O_2$	4.2×10^{-27}	-1.0	-100, 700	[98], [162]
119. $O_2^- + O \longrightarrow O_3 + e$	1.5×10^{-10}	0.0	0.0	[98], [162]
120. $O^- + O \longrightarrow O_2 + e$	5.0×10^{-10}	0.0	0.0	[192]
121. $O_3^- + O \longrightarrow O_2 + O_2 + e$	3.0×10^{-10}	0.0	0.0	[98], [162]
122. $O_2^- + N_2 \longrightarrow O_2 + e + N_2$	1.097×10^{-13}	0.5	4990	[98]
123. $O_2^- + O_2 \longrightarrow O_2 + e + O_2$	1.559×10^{-11}	0.5	5590	[98]
124. $N_2^+ + N_2 + N_2 \longrightarrow N_4^+ + N_2$	5.0×10^{-29}	0.0	0.0	[98], [162]
125. $O_2^+ + N_2 + N_2 \longrightarrow N_2O_2^+ + N_2$	8.1×10^{-26}	-2.0	0.0	[98], [162]
126. $O_2^+ + O_2 + O_2 \longrightarrow O_4^+ + O_2$	2.028×10^{-22}	-3.2	0.0	[98], [162]
127. $N_4^+ + O_2 \longrightarrow O_2^+ + N_2 + N_2$	2.5×10^{-10}	0.0	0.0	[98], [162]
128. $O_4^+ + N_2 \longrightarrow N_2O_2^+ + O_2$	2.957×10^{-18}	2.5	2650	[98]
129. $O_4^+ + O_2 \longrightarrow O_2^+ + O_2 + O_2$	$2.673\times10^{+04}$	-4.0	5030	[98]
130. $N_2O_2^+ + N_2 \longrightarrow O_2^+ + N_2 + N_2$	$1.48\times10^{+07}$	-5.3	2357	[98], [162]
131. $N_2O_2^+ + O_2 \longrightarrow O_4^+ + N_2$	1.0×10^{-09},	0.0	0.0	[98], [162]

Continued on next page

Table A.2 – continued from previous page

Reaction	A	n	E_a	**Ref.**
132. $O_2^- + O_2 + M \longrightarrow O_4^- + M$	1.05×10^{-28}	-1.0	0.0	[98], [162]
133. $O_2^- + O \longrightarrow O_2 + O^-$	3.3×10^{-10}	0.0	0.0	[98]
134. $O_3^- + O \longrightarrow O_2^- + O_2$	3.2×10^{-10}	0.0	0.0	[98], [162]
135. $O^- + O_2 + M \longrightarrow O_3^- + M$	3.3×10^{-28}	-1.0	0.0	[98]
136. $O_4^- + M \longrightarrow O_2^- + O_2 + M$	1.0×10^{-10}	0.0	1044	[98], [162]
137. $O_2^- + O_2^+ \longrightarrow O_2 + O_2$	3.464×10^{-06}	-0.5	0.0	[98]
138. $O^- + O_2^+ \longrightarrow O + O_2$	3.464×10^{-06}	-0.5	0.0	[98]
139. $O_3^- + O_2^+ \longrightarrow O_3 + O_2$	3.464×10^{-06}	-0.5	0.0	[98]
140. $O_2^- + O_2^+ \longrightarrow O_2 + O + O$	1.0×10^{-07}	0.0	0.0	[98]
141. $O_3^- + O_2^+ \longrightarrow O_3 + O + O$	1.0×10^{-07}	0.0	0.0	[98]
142. $O_2^- + O_2^+ + M \longrightarrow O_2 + O_2 + M$	3.118×10^{-19}	-2.5	0.0	[98], [162]
143. $N_2^+ + e \longrightarrow N + N$	4.85×10^{-06}	-0.5	0.0	[98]
144. $N_2^+ + e \longleftrightarrow N + N(^2D)$	3.46×10^{-06}	-0.5	0.0	[98]
145. $N_4^+ + e \longleftrightarrow N_2(C^3) + N_2$	3.46×10^{-5}	-0.5	0.0	[98]
146. $NO^+ + e \longleftrightarrow N(^2D) + O$	2.08×10^{-3}	-1.5	0.0	[98]
147. $N_2(A^3) + N_2(ap) \longrightarrow N_4^+ + e$	5.00×10^{-11}	0.0	0.0	[98]
148. $N_2(ap) + N_2(ap) \longrightarrow N_4^+ + e$	2.00×10^{-10}	0.0	0.0	[98]
149. $N_4^+ + N_2 \longrightarrow N_2^+ + 2\,N_2$	3.80×10^{-15}	0.0	0.0	[98]
150. $O_2^+ + NO \longrightarrow NO^+ + O_2$	4.40×10^{-10},	0.0	0.0	[98]
151. $N_2(A^3) + H_2 \longrightarrow N_2 + 2\,H$	4.4×10^{-10}	0.0	3500	[169]
152. $N_2(B^3) + H_2 \longrightarrow N_2(A^3) + H_2$	2.5×10^{-11}	0.0	0.0	[169]
153. $N_2(ap) + H_2 \longrightarrow N_2 + 2\,H$	2.6×10^{-11}	0.0	0.0	[169]
154. $N_2(C^3) + H_2 \longrightarrow N_2 + 2\,H$	3.3×10^{-10}	0.0	0.0	[169]
155. $O_2(a_1) + H_2 \longrightarrow 2\,OH$	2.8×10^{-9}	0.0	17906	[169]
156. $O_2(a_1) + H_2 \longrightarrow O_2 + H_2$	2.6×10^{-19}	0.5	0.0	[169]
157. $O_2(a_1) + H \longrightarrow O + OH$	1.3×10^{-11}	0.0	2530	[169]
158. $O_2(a_1) + H \longrightarrow O_2 + H$	5.2×10^{-11}	0.0	2530	[169]

Continued on next page

Table A.2 – continued from previous page

Reaction	A	n	E_a	**Ref.**
159. $O_2(a_1) + HO_2 \longrightarrow O_2 + HO_2$	2.0×10^{-11}	0.0	0.0	[169]
160. $O_2(b_1) + H_2 \longrightarrow O_2(a_1) + H_2$	1.0×10^{-12}	0.0	0.0	[169]
161. $N(^2D) + H_2 \longrightarrow NH + H$	4.6×10^{-11}	0.0	880	[169]
162. $N(^2P) + H_2 \longrightarrow N + H_2$	2.0×10^{-15}	0.0	0.0	[169]
163. $O(^1D) + H_2 \longrightarrow H + OH$	1.2×10^{-10}	0.0	0.0	[169]
164. $O(^1S) + H_2 \longrightarrow O + H_2$	2.6×10^{-16}	0.0	0.0	[169]
165. $N_2(A^3) + CH_4 \longrightarrow N_2 + CH_3 + H$	1.2×10^{-10}	0.0	3170	[169]
166. $N_2(B^3) + CH_4 \longrightarrow N_2 + CH_3 + H$	3.0×10^{-10}	0.0	0.0	[169]
167. $N_2(ap) + CH_4 \longrightarrow N_2 + CH_3 + H$	3.0×10^{-10}	0.0	0.0	[169]
168. $N_2(C^3) + CH_4 \longrightarrow N_2 + CH_3 + H$	5.0×10^{-10}	0.0	0.0	[169]
169. $O(^1D) + CH_4 \longrightarrow CH_3 + OH$	1.89×10^{-10}	0.0	0.0	[169]
170. $O(^1D) + CH_4 \longrightarrow CH_3O + H$	3.1×10^{-11}	0.0	0.0	[169]
171. $O(^1S) + CH_4 \longrightarrow O + CH_4$	2.7×10^{-14}	0.0	0.0	[169]
172. $N_2(A^3) + C_2H_4 \longrightarrow N_2 + C_2H_3 + H$	5.5×10^{-11}	0.0	0.0	[169]
173. $N_2(A^3) + C_2H_4 \longrightarrow N_2 + C_2H_2 + H_2$	5.5×10^{-11}	0.0	0.0	[169]
174. $N_2(ap) + C_2H_4 \longrightarrow N_2 + C_2H_3 + H$	2.0×10^{-10}	0.0	0.0	[169]
175. $N_2(ap) + C_2H_4 \longrightarrow N_2 + C_2H_2 + H_2$	2.0×10^{-10}	0.0	0.0	[169]
176. $N_2(B^3) + C_2H_4 \longrightarrow N_2 + C_2H_3 + H$	1.5×10^{-10}	0.0	0.0	[169]
177. $N_2(B^3) + C_2H_4 \longrightarrow N_2 + C_2H_2 + H_2$	1.5×10^{-10}	0.0	0.0	[169]
178. $N_2(C^3) + C_2H_4 \longrightarrow N_2 + C_2H_3 + H$	1.5×10^{-10}	0.0	0.0	[169]
179. $N_2(C^3) + C_2H_4 \longrightarrow N_2 + C_2H_2 + H_2$	1.5×10^{-10}	0.0	0.0	[169]
180. $O(^1D) + C_2H_4 \longrightarrow C_2H_3 + OH$	4.0×10^{-10}	0.0	0.0	[169]
181. $O(^1S) + C_2H_4 \longrightarrow O + C_2H_4$	1.0×10^{-9}	0.0	0.0	[169]
182. $N_2(A^3) + C_2H_2 \longrightarrow N_2 + C_2H + H$	2.0×10^{-10}	0.0	0.0	[169]
183. $N_2(ap) + C_2H_2 \longrightarrow N_2 + C_2H + H$	3.0×10^{-10}	0.0	0.0	[169]
184. $N_2(B^3) + C_2H_2 \longrightarrow N_2 + C_2H + H$	3.0×10^{-10}	0.0	0.0	[169]
185. $N_2(C^3) + C_2H_2 \longrightarrow N_2 + C_2H + H$	3.0×10^{-10}	0.0	0.0	[169]

Continued on next page

Table A.2 – continued from previous page

Reaction	A	n	E_a	**Ref.**
186. $O(^1D) + C_2H_2 \longrightarrow C_2H + OH$	3.0×10^{-10}	0.0	0.0	[169]
187. $O(^1S) + C_2H_2 \longrightarrow O + C_2H_2$	9.0×10^{-10}	0.0	0.0	[169]
188. $N_2(A^3) + C_3H_8 \longrightarrow N_2 + C_3H_6 + H_2$	1.3×10^{-12}	0.0	0.0	[169]
189. $N_2(ap) + C_3H_8 \longrightarrow N_2 + C_3H_6 + H_2$	3.0×10^{-10}	0.0	0.0	[169]
190. $N_2(B^3) + C_3H_8 \longrightarrow N_2 + C_3H_6 + H_2$	3.0×10^{-10}	0.0	0.0	[169]
191. $N_2(C^3) + C_3H_8 \longrightarrow N_2 + C_3H_6 + H_2$	3.0×10^{-10}	0.0	0.0	[169]
192. $O(^1D) + C_3H_8 \longrightarrow I\text{-}C_3H_7 + OH$	7.9×10^{-10}	0.0	0.0	[169]
193. $O(^1S) + C_3H_8 \longrightarrow C_3H_8 + O$	9.0×10^{-13}	0.0	0.0	[169]
194. $N_2(A^3) + C_3H_6 \longrightarrow N_2 + C_3H_5 + H$	1.4×10^{-10}	0.0	0.0	[169]
195. $N_2(A^3) + C_3H_6 \longrightarrow N_2 + C_2H_3 + CH_3$	1.4×10^{-10}	0.0	0.0	[169]
196. $N_2(ap) + C_3H_6 \longrightarrow N_2 + C_3H_5 + H$	1.4×10^{-10}	0.0	0.0	[169]
197. $N_2(ap) + C_3H_6 \longrightarrow N_2 + C_2H_3 + CH_3$	1.4×10^{-10}	0.0	0.0	[169]
198. $N_2(B^3) + C_3H_6 \longrightarrow N_2 + C_3H_5 + H$	1.4×10^{-10}	0.0	0.0	[169]
199. $N_2(B^3) + C_3H_6 \longrightarrow N_2 + C_2H_3 + CH_3$	1.4×10^{-10}	0.0	0.0	[169]
200. $N_2(C^3) + C_3H_6 \longrightarrow N_2 + C_3H_5 + H$	1.4×10^{-10}	0.0	0.0	[169]
201. $N_2(C^3) + C_3H_6 \longrightarrow N_2 + C_2H_3 + CH_3$	1.4×10^{-10}	0.0	0.0	[169]
202. $O(^1D) + C_3H_6 \longrightarrow C_3H_5 + OH$	1.0×10^{-9}	0.0	0.0	[169]
203. $O(^1S) + C_3H_6 \longrightarrow O + C_3H_6$	8.0×10^{-10}	0.0	0.0	[169]
204. $N_2(A^3) + C_2H_6 \longrightarrow N_2 + C_2H_4 + H_2$	1.8×10^{-10}	0.0	1980	[169]
205. $N_2(ap) + C_2H_6 \longrightarrow N_2 + C_2H_4 + H_2$	5.0×10^{-8}	0.0	1880	[169]
206. $N_2(B^3) + C_2H_6 \longrightarrow N_2 + C_2H_4 + H_2$	5.0×10^{-8}	0.0	1880	[169]
207. $N_2(C^3) + C_2H_6 \longrightarrow N_2 + C_2H_4 + H_2$	3.0×10^{-10}	0.0	0.0	[169]
208. $O(^1D) + C_2H_6 \longrightarrow C_2H_5 + OH$	6.3×10^{-10}	0.0	0.0	[169]
209. $O(^1D) + C_2H_6 \longrightarrow O + C_2H_6$	1.0×10^{-12}	0.0	0.0	[169]

B. MODEL VALIDATION

B.1 Microwave Electric field Assisted Combustion

In the current work, the 1D flame code in the open source Cantera software is modified for the first time to solve for flame profiles subjected to electric fields. Therefore, the solution of the governing equations and implementation of the detailed transport model must first be validated. To do this, calculations using the current model are compared with results from the most recent modeling study in [128]. Then, the performance of the ion chemistry described in Section 2.3.5 is assessed by comparing calculated ion density profiles with available experimental data.

B.1.1 Comparison with Simulation of Han et al. [128]

The most recent simulations of ions in a premixed flame were performed by Han et al. in 2015 [128]. They first modeled methane-oxygen flames with $\phi = 0.216$ using a simplified ion reaction mechanism for sensitivity analysis. They used the GRI3.0 mechanism [135] for neutral chemistry with the simplified reaction mechanism for charged species given in Table B3 of [128].

To validate the solution of the governing equations using the detailed transport model of Han et al., flame profiles were calculated using the same simplified ion chemistry. Profiles of the number density of H_3O^+ and flame temperature calculated using the present model are shown in Figure B.1 and match closely the results from Han et al. using the Stockmayer-(n, 6, 3) transport model. This comparison confirms that the governing equations were modified appropriately and that the detailed transport model was correctly implemented.

Figure B.2 shows mixture-averaged diffusion coefficients of two major positively charged species, H_3O^+ and HCO^+, calculated using the simplified transport model described in section 2.3.3. The values agree very closely with the diffusion coefficients given in Ref. [128], confirming that the simplified transport model can be used without significant error.

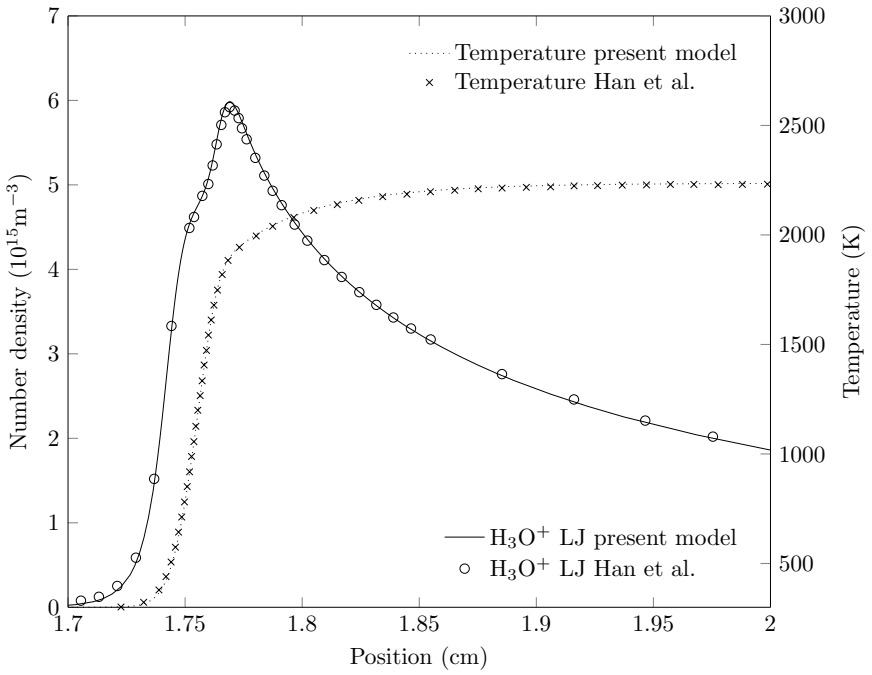

Figure B.1. Comparison of density of the major positive ion (H_3O^+) and flame temperature profiles to Han et al. [128]. Both simulations use the simplified ion reaction mechanism and detailed transport model given in [128].

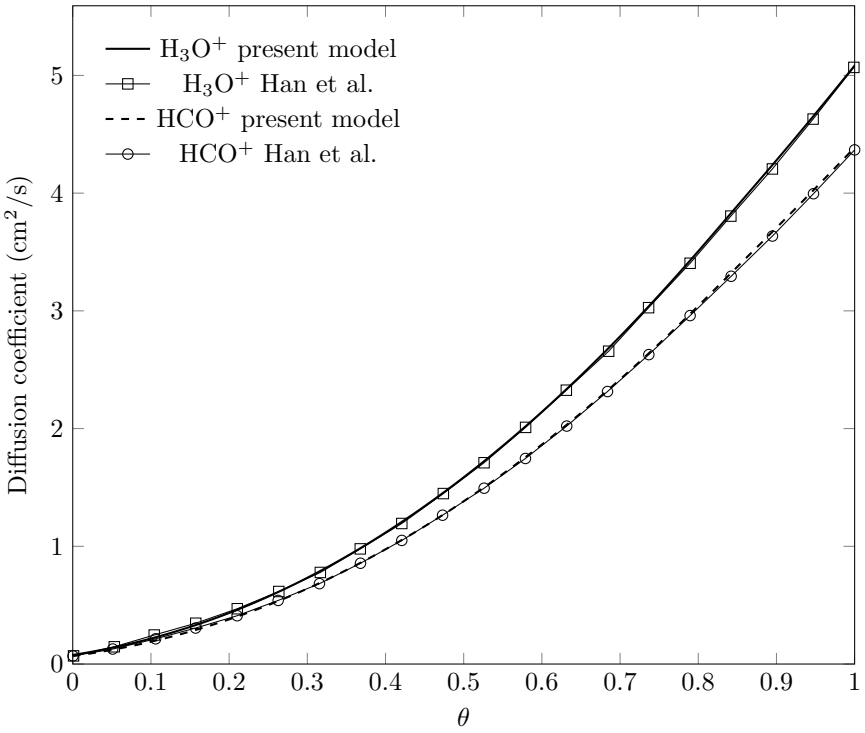

Figure B.2. Comparison of calculated mixture-averaged diffusion coefficients of two major positive ions throughout the flame to the coefficients given in Ref. [128]. The diffusion coefficients are plotted against the progress variable, $\theta = (T - T_u)/(T_b - T_u)$, where $T_u = 300$K, and $T_b = 2234$K.

B.1.2 Comparison with the Experiment of Maclatchy [122]

Since propane/air is used in the experiment of [122], we use the USC C3 mechanism [136] to perform a proper simulation for neutral species. Figure B.3 compares the total number density of positive ions calculated using the detailed ion mechanism presented in Section 2.3.5 to the results of Maclatchy [122]. Note that in the experiment the ion profile is measured across both sides of the Bunsen flame. The measured profile for the right side of the flame front arm was shown in an enlarged figure (Figure 3 of [122]), and we use it to compare to the current study. The predicted profile of total positive ion density is narrower (width at half maximum 0.270 mm compared to 0.712 mm) and has a higher peak density compared to the experimental result (4.16×10^{17} compared to 3.50×10^{17} m^{-3}). However, the left side of the flame front has a sharper ion profile and higher peak number density of approximately 3.75×10^{17} m^{-3}, which is closer to the predicted profile in the present simulation. One potential reason for a thicker flame in the experiment versus simulation is turbulence of the flame front, which is observed for a stoichiometric propane/air Bunsen flame in Ref. [122]. A second possible reason for the wider width of the measured flame profile is the angle (θ) of the flame cone. For example, if the measuring plane is parallel to the burner deck, which is not perpendicular to the flame front, the measured profile will be stretched by a factor of $1/\cos(\theta)$.

B.1.3 Comparison with the Experiment of Stockman *et al.* [69]

Since Sullivan *et al.* [68] calculated the flame speed by the simulated flow field without a direct measurement, more accurate experimental measurements of the flame speed as well as other parameters such as temperature and species concentration are desirable for model comparison and validation. Stockman *et al.* [69] measured microwave-enhanced flame characteristics using multiple advanced diagnostics. First, they used particle image velocimetry (PIV) to measure the flame speed which is more accurate than using a simulated flow field as in [68]. Second, they used filtered Rayleigh scattering (FRS) to measure the temperature distribution along the centerline of the flow normal to the flame front. Finally, they measured the OH concentration using planar laser induced fluorescence (PLIF). They used the

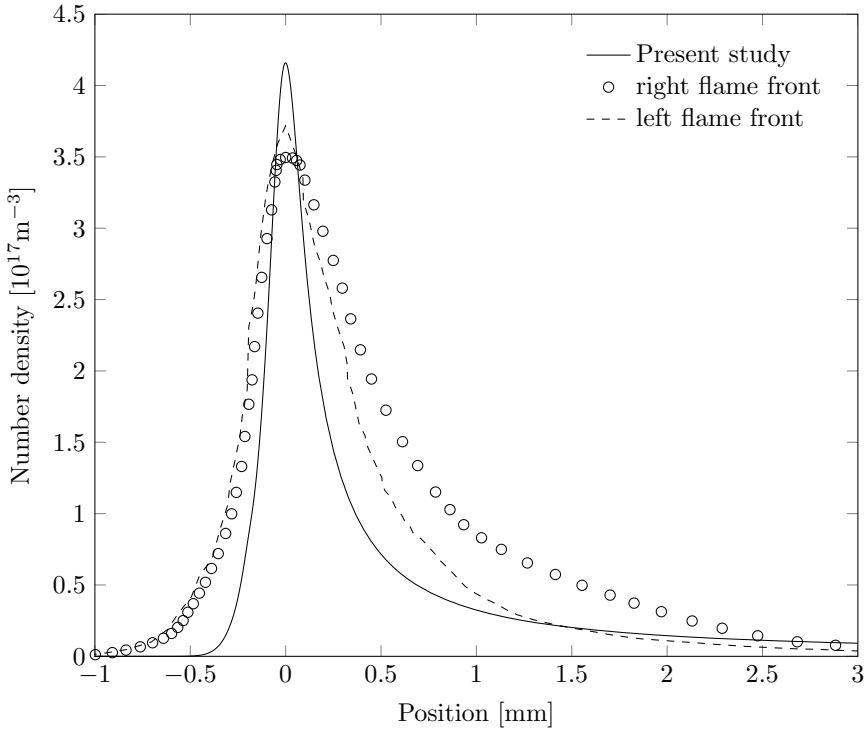

Figure B.3. Total number density of positive ions in a propane/air stoichiometric flame calculated using the current model compared with experimental measurements of Ref. [122]. Note that we set the origin at the peak of the ion number density.

same experimental system as [68] with the microwave power at 1.3 kW. Using Equation 2.16 [68], we estimate the electric field strength to be approximately $E = 1.07$kV/cm. However, Stockman and co-workers [69] stated that the calculated electric field strength was 5 kV/cm without electric breakdown, but this value is much higher than the breakdown electric field strength (2 kV/cm) according to [68], so we use $E = 1.07$kV/cm in our simulation instead. The equivalence ratios used for the temperature and OH concentration measurements in [69] were 0.75 and 0.76, respectively. For simplicity and convenience, we use a $\phi = 0.75$ methane/air mixture for our simulation. We use the reaction mechanism of [109] for the neutral species and the ion mechanism in Table A.1 for the charged species and used the EEDF to calculate rates for recombination reactions of $C_2H_3O^+$). Note that we do not use the GRI3.0 mechanism [135] because it significantly over-predicts the concentration of CH according to [141] which is important for the chem-ionization rate. One difference between our model and the experiment is that the experiment used a counter-flow premixed flame (stagnation flow) while our model uses an flat flame (zero strain rate).

Our model predicts a 13.2% enhancement of the flame speed at $\phi = 0.75$ which is very close to the 14.3% enhancement measured by Stockman et al. [69]. Figure B.4 shows a comparison of the measured and simulated temperature distribution along a line normal to the flame front. Although the experimental flame is slightly stretched and curved, the temperature profiles match very well especially in the burned zone (downstream of the flame). Therefore, we can conclude that our model accurately simulates the temperature difference due to the applied microwave field. Figure B.5 shows the OH distribution along a line normal to the flame front. The experimental OH profile is wider with a slightly lower peak value versus the simulations, but overall the model prediction is close to the experimental values.

B.2 NRP Plasma Assisted Combustion

B.2.1 Comparison with the Experiment of Adamovich *et al.* [169]

We compare our simulation to the experiment [170] and the updated simulation [169]. The plasma is generated between two spherical electrode in a low pressure chamber by NRP discharge, and the electric field is close to uniform spatially due to the radius of the electrode

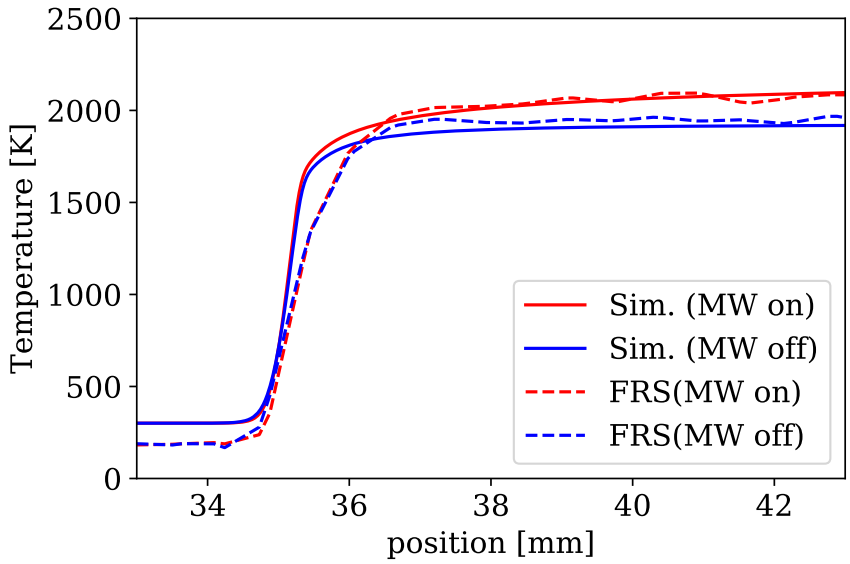

Figure B.4. Comparison of the temperature profile measured by Stockman et al. [69] to the current model simulation.

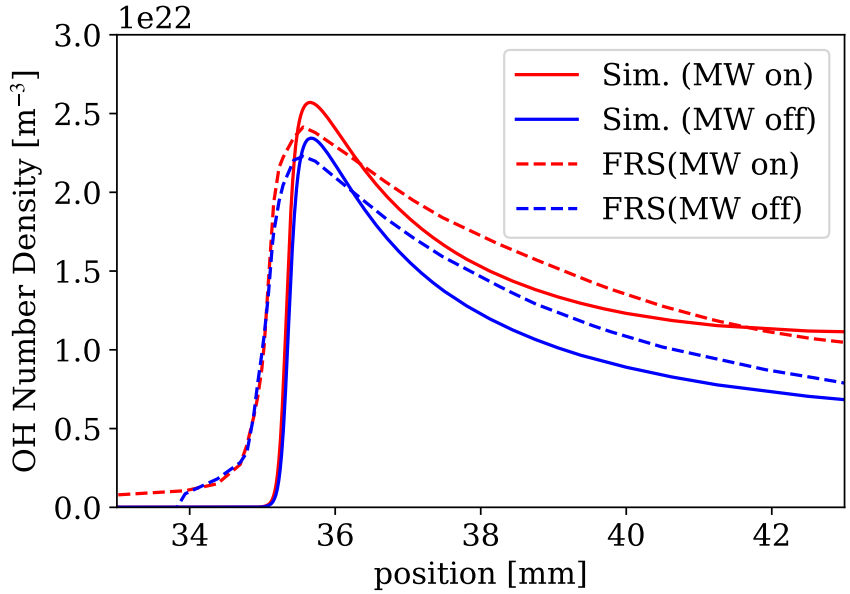

Figure B.5. Comparison of the OH profile measured by Stockman et al. [69] to the current model simulation.

is close to the distance between electrodes. The condition produce a decent size plasma that is easy to observe and measure for a NRP plasma. With the detailed measurement of [170], we can validate our model well by comparing to the gas temperature, vibrational temperature, vibrational levels. Figure B.6 shows the temperature profile of the plasma. Our simulation matches well to the experiment temperature from 10^{-7}s to 10^{-4}s, but underestimate the gas temperature for longer time scale. The major discrepancy of temperature in the longer time scale between our simulation and the experiment is likely to be the complex flow field generate by the pulse, which our zero-dimensional model cannot account. Several factor can affect the gas temperature in longer time scale. The discharge radius can change over time, and the ratio of heat transfer rate to the volume depends on the discharge radius. e.g. larger discharge radius keep heat longer than a small discharge radius. The surrounding air can heat up significantly which reduces the heat transfer rate from the discharge gas to the surrounding air. The vibrational relaxation rate can also affect the gas temperature in longer time scale. Figure B.7 shows that the vibrational levels in our simulation are close to the experiment data. However, the discrepancy grows larger as the vibrational levels go higher.

B.2.2 Convergence Tests

To ensure the accuracy and convergence of the simulation results using the 0D plasma model, we perform a single pulse simulation with two different sizes of the time step. The gas composition in the simulation is 29.4% oxygen and 70.6% nitrogen and the flow rate is 1 m/s at 300 K. Figure B.8 shows the two sets of time steps used for the comparison. We decrease the current set of time steps used in Chapter 3 ("current Δt") by one order of magnitude ("small Δt") and compare the simulation results. Figure B.8 compares the profiles of electron number density from the 0D simulations using the two sets of time steps from Figure B.8. The electron profiles match each other well with only a slightly higher peak value for the set of small Δt. Therefore, the time steps of our simulations in Chapter 3 are small enough to be considered accurate and converged.

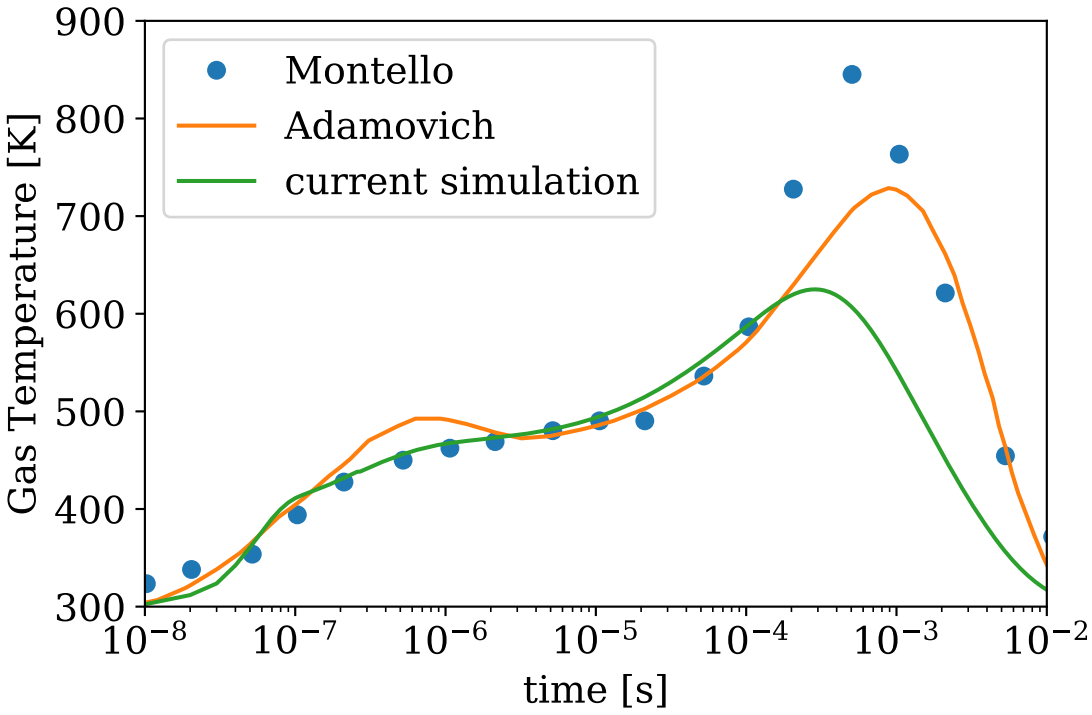

Figure B.6. The temperature profile of the low pressure plasma. The experimental data is from [170], and the simulation data is from [169].

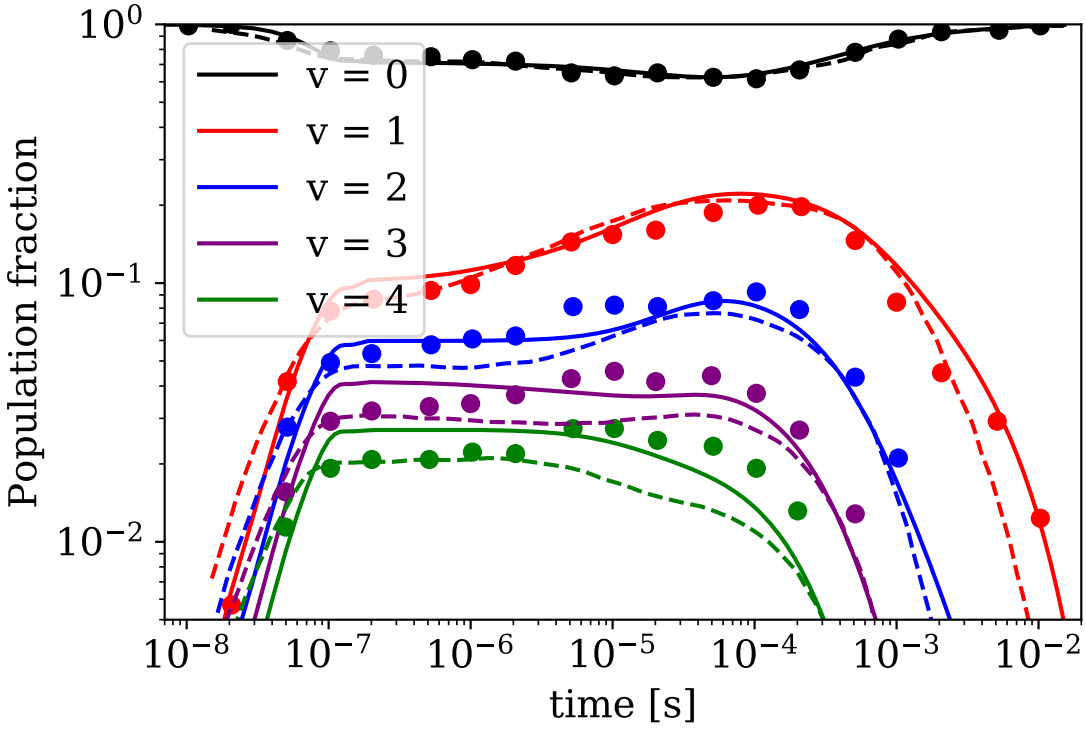

Figure B.7. The vibrational levels of the low pressure plasma. The experimental data is from [170]. The solid line is the current simulation. The dashed line is the simulation of [169]. And the dot is the experiment of [170].

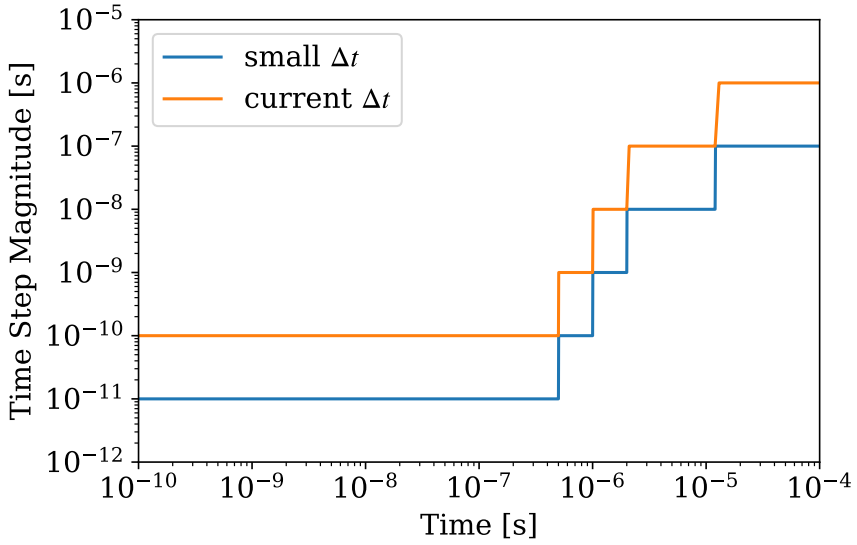

Figure B.8. Two time-step profiles used to confirm convergence of the 0D plasma simulations. The "current Δt" is the time steps used in all simulations in Chapter 3, and the "small Δt" is one order of magnitude smaller than the current Δt.

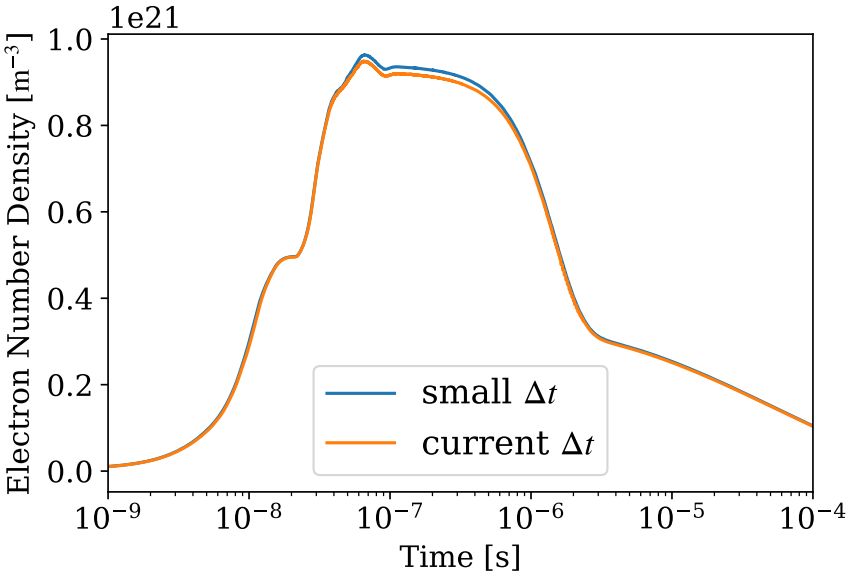

Figure B.9. Comparison of electron number density from the 0D plasma simulations with the current and small time steps shown in Figure B.8.

For the 1D flame simulation, we have shown in Figure 3.5 that the time resolution is fine enough for a temporally accurate and converged simulation. Therefore, we focus on the spatial resolution in this section. Ember [102] uses two parameters to control the refining criterion of the grid: *vtol* is the maximum relative scalar variation of each state vector (such as temperature or mass fraction), and *dvtol* is the maximum relative variation of the gradient of each state vector. For high accuracy, vtol $\leq$ 0.08 and dvtol $\leq$ 0.12 according to [102]. Therefore, we set all simulations in Chapter 3 to use vtol = 0.06 and dvtol = 0.1. Figure B.10 shows that decreasing vtol by a factor of two from 0.03 to 0.015 while keeping dvtol constant does not have a significant effect on the heat release rate (HRR). Additionally, our simulations in Chapter 3 with vtol = 0.06 ave less than 10% difference in the time to the peak HRR versus the smaller values of vtol (0.03 and 0.015). Figure B.11 shows that decreasing dvtol by a factor of two (from 0.05 to 0.025) does not result in a substantial change in the HRR profile, and our simulations with dvtol = 0.1 only have around 10 % difference in the time to the peak HRR. Although we do not use the extremely fine tolerances (vtol $\leq$ 0.03 and dvtol $\leq$ 0.05) for our simulations, our results should differ by less than 10%.

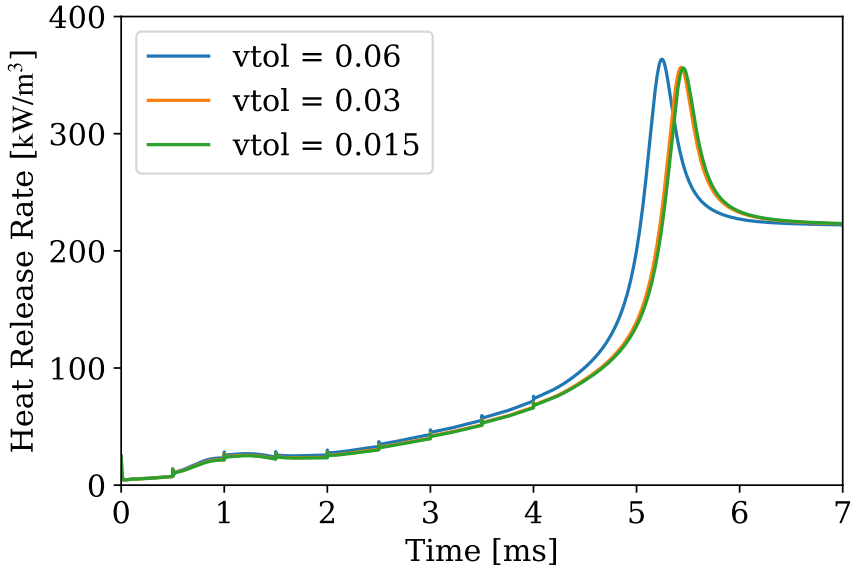

Figure B.10. Comparison of the heat release rate (HRR) for different values of vtol in the 1D flame ignition simulation (dvtol = 0.01, PRF = 2kHz, and a = 400 1/s).

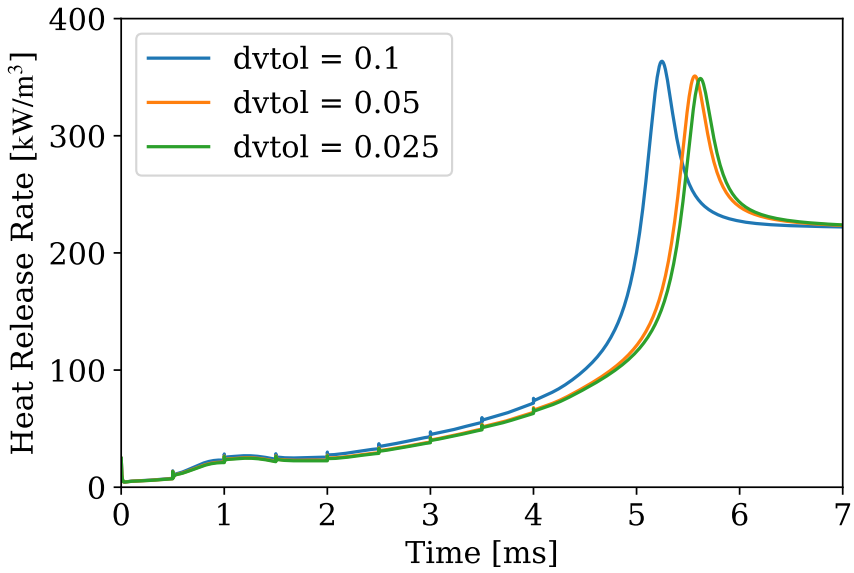

Figure B.11. Comparison of the heat release rate (HRR) for different values of dvtol in the 1D flame ignition simulation (vtol = 0.06, PRF = 2kHz, and a = 400 1/s).

C. SENSITIVITY ANALYSIS

This chapter introduces a novel sensitivity analysis for investigating the effectiveness of radicals on a burner flame.

C.1 Introduction

Understanding the kinetic effect of PAC is important for applying an plasma discharge effectively with a combustion system. Studies have investigated the effect of a specific species produced by a plasma discharge on a flame. Takita et al. [158] investigated the effects of addition of radicals on burning velocity of a hydrogen-air flame numerically. They found that the addition of radicals only have significant increase on burning velocity when the temperature is high (>750 K), and oxygen/nitrogen radical (O) are more effective than hydrogen radical. Species other than radicals can also enhance a flame. Ombrello et al. [193], [194] investigated the effect of O_3 and O2(a1) with a tribrachial triple flame at atmospheric pressure. They found that injection of O_3 can increase the flame speed effectively because ozone as the carrier of oxygen atom at low temperature releases oxygen atom in the pre-heat zone of the flame, while O2(a1) has much less effect on the flame speed. Pinchak et al. [195] investigated the effects of ozone on enhancing a premixed burner flame with different stretch rate at sub-atmospheric pressure (10.7 kPa) and room temperature (300 K). They found that the enhancement increases as the stretch rate increases. Won et al. [167] connected an ozone generator to a counterflow burner to investigate extinction limit of the flame. They found that the ozone can extend the extinction limit especially for the cool flame regime. Beside the species mentioned above, other species produced by radicals reacting with fuels such as CH_3 and HO_2 can also change the flame speed. To quantitatively compare the effectiveness of different species and plasma discharges on increasing the flame speed, we propose a fast and efficient way to evaluate the effectiveness using sensitivity analysis with the Adjoint method [196].

C.2 Method

We connect a plasma discharge to a counter-flow premixed flame. The structure of the 1D counter-flow premixed flame for the sensitivity analysis is shown in Figure C.1. The oppose flow is set to be the equilibrated product (burned gas) of the unburned gas. We set a point z_{probe} where $T(z = z_{probe}) = 2000$ K, which is at vicinity of the premixed methane/air flame (the adiabatic temperature is around 2200K). When radicals are added to the main gas flow, the flame burns faster and moves toward the unburned gas. This leads to increasing temperature at z_{probe}. We can use the Adjoint method to find the sensitivity of the temperature at z_{probe} to the inlet mole fractions of chemical species,

$$S_k = \frac{1}{T_{probe}} \frac{dT_{probe}}{dX_{k,in}} \tag{C.1}$$

where $X_{k,in}$ is the inlet mole fraction of species k. Positive sensitivity indicates the tendency of increasing temperature at z_{probe}, which corresponds to increasing the laminar flame speed. To evaluate the effectiveness of a plasma discharge, we can calculate the mean sensitivity by,

$$\bar{S} = \sum_k S_k X_{k,\text{in}} \tag{C.2}$$

Note that the sensitivity analysis uses a steady-state solution of 1D flames which does not consider the dynamic effect of plasma discharge. In reality, the concentration of radicals and temperature of a NRP plasma oscillate at PRF which requires an unsteady solver.

C.3 Result

We chose a stoichiometric methane/air mixture at atmospheric pressure as the unburned mixture of the counter-flow premixed flame and the San Diego Mechanism [109] to perform sensitivity analysis. The premixed gas temperature is increase from 300K to 1000K to show the effect of gas temperature on the effectiveness of radicals increasing the flame speed. Figure C.2 shows the sensitivity for several important radicals and species. The sensitivities increase from 600K for most of the species. Oxygen atom has the highest for all temperatures.

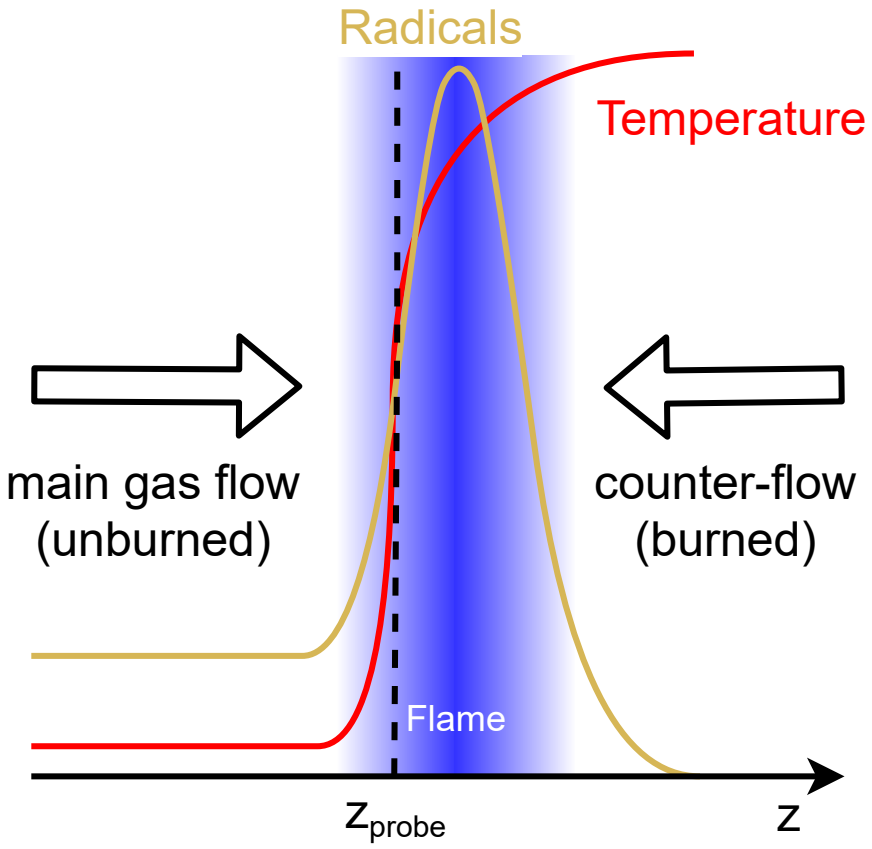

Figure C.1. Schematic for the burner-stabilized flame.

Hydrogen atom has the second highest value at 1000K. CH_3 and OH have very close values, and are more effective at 800K compared the hydrogen atom.

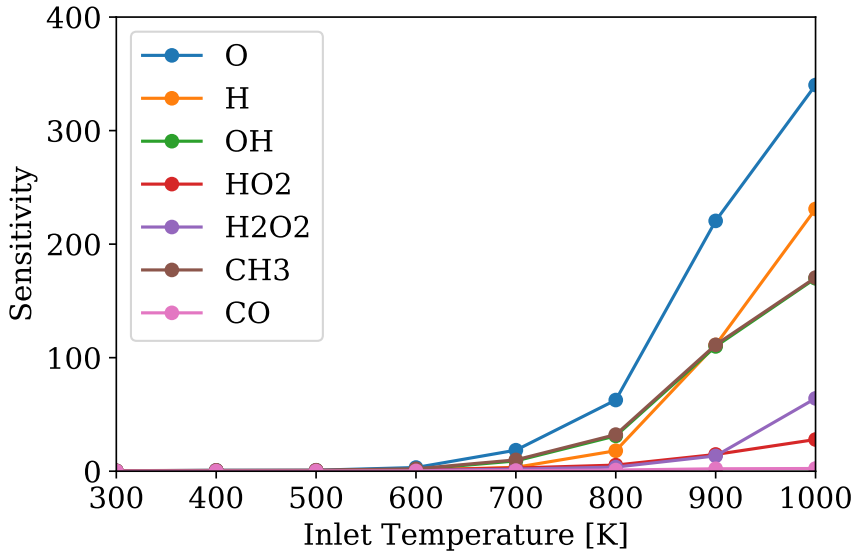

Figure C.2. The sensitivity of inlet species influence on the flame location.